LIVE-CELL TRACKING OF AUTOPHAGY FACTORS DEFINE THE ROLE OF ATG9 AND ATG2 IN AUTOPHAGOSOME BIOGENESIS

By

David Grant Broadbent

A DISSERTATION

Submitted to
Michigan State University
in partial fulfillment of the requirements
for the degree of

Physiology – Doctor of Philosophy

2023

ABSTRACT

Since its discovery, autophagy has been implicated in prevalent diseases that occur with advanced age including cancer, neurological dementias, and cardiovascular health. As we age, autophagy becomes defective, and key structures called autophagosomes are unable to sequester and degrade defective cellular material effectively. On the other hand, tumors can hijack autophagosome biogenesis leading to a poor patient prognosis. The exact pathogenesis of these conditions remains poorly understood. To actualize the potential of autophagy in the clinic, it is important to define the mechanisms governing autophagosome biogenesis, so that one day we can understand and correct the key defects that are currently plaguing patients.

Autophagosomes are created on an as needed basis; usually they are made in response to cellular stresses such as nutrient depletion or intracellular organelle dysfunction. Cells starved of amino acids, downregulate mTOR resulting in cell cycle arrest and the initiation of autophagy. Intriguingly, while the amino acid withdrawal is uniform across all cells, they have a highly varied response, suggesting a complex and misunderstood regulatory pathway. I set out to create novel tools and methods to quantitatively define the signals regulating autophagosome biogenesis. I develop a pipeline for autophagy foci analysis. I pair this novel methodology with endogenously tagged autophagy factors to provide paradigm changing insights into the regulation of autophagosome biogenesis.

For the first time, we define absolute protein abundances of the autophagy pathway. Both ATG2A and ULK1 are far lower expressed than other autophagy proteins

and are likely purposefully regulated in this manner. Intriguingly, the ULK1 complex is thought to be constitutive with its other subunits, however, ATG13 was ~9 fold higher than ULK1, it is likely that ULK1 is the limiting subunit within the complex.

Live-cell imaging of endogenously tagged factors revealed that ~80% of the population of foci were short ~30 seconds or less. Dual-tracking of short foci with ATG8 family members and P62 showed that these structures rarely colocalize, suggesting that the phagophores are not progressing to mature autophagosomes. Diffusion coefficient analysis of foci identifies two gaussian fitted populations in all autophagy factors, but ATG2. Dual-tracking of ATG2A and ATG13 shows that double positive foci are longer lived, while non-colocalized ATG2A foci were short lived, adding further evidence that many foci never mature into autophagosomes.

Knockout of ATG9A abrogated ATG2A foci, but intriguingly Halo-ATG9A, rarely formed foci. Imaging of Halo-ATG9A differed substantially from previous reports where ATG9A foci transiently interacted at autophagosomes. We rectified this difference by imaging Halo-ATG9A over-time and showed that it accumulates in the lysosome and demonstrated that previous interactions were lysosomal ATG9A interacting with autophagosomes.

ACKNOWLEDGEMENTS

Schmidt Lab, collaborators, and IQ personnel

I'd like to express my deep thanks to Dr. Jens Schmidt for his continual support through the very challenging and unpredictable autophagy project. Jens provided a phenomenal environment for me to develop and mature as a scientist. He mentored me in almost every aspect of running a lab, providing an extensive knowledge in biochemistry, advanced imaging techniques, and strategic writing; moreover, he challenged my ideas, yet gave me the freedom and confidence to see them through. He ultimately taught me to push myself to produce high quality data that thoroughly vets my hypotheses. I thank him for this life defining experience as there are very few laboratories in the world where I could have learned and accomplished what I did in my PhD.

I'd like to express my heartfelt gratitude to Dr. Carlo Barnaba, who worked at the bench alongside me in the Autophagy project; he played a central role in project conceptualization, data collection, analysis, statistics, and was instrumental in the development of novel tools to understand autophagy. In many ways Carlo acted as an unofficial second mentor to me throughout my PhD, freely sharing his expertise in chemistry, programming, image analysis, protein purification, single molecule techniques, statistics, and lipidology. Additionally, Carlo has been a reliable sounding board and provided comedic relief as we struggled to understand the complex process of autophagy. It is not an exaggeration to say that the autophagy project would not have been possible without his help, and I couldn't be happier with the impactful contributions we have made to the autophagy field.

I'd like to thank Dr. Gloria Perez, who maintains an immaculate lab despite my

presence and has provided substantial hands-on support at the bench throughout my PhD. She took a unique interest in the autophagy project, and I was fortunate to have her help throughout my PhD. In conjunction with Dr. Perez, I would like to thank Dr. Masamitsu for an excellent collaboration and for the many exciting endosomal discussions. A special thanks to Ahmed Zarea for his substantial contributions to the project as well.

To all other members of the laboratory including—past—Dr. Eric Patrick and—present—Dr. Joshua Heyza, Dr. Tomas Janovic, Basma Klump, Maria Mikhova, Maddy Turley, Cody Phillips, Emily Kaminsky. You all have enhanced my PhD in so many ways, many of which cannot be fully described here, but thank you for the significant and varied contributions that each of you have made throughout my PhD.

I would like to thank Dr. Josh Andersen and Dr. Colten McEwan for the collaborative efforts on understanding the connection between autophagy and ubiquitin biology. While this collaboration remains in progress, there is no doubt that our discussions were worthwhile and benefited all my science.

I would like to thank Matt Bernard in IQ including for his reliable and efficient flow cytometry assistance, sorting over sixty cell lines for my project alone. In addition, Gabriela, who has been a pillar within the IQ east second floor when it comes to lab maintenance and procedure. I would like to thank all of IQ, for its collaborative environment and to the many people that have assisted me in one way or another within my PhD.

<u>Family</u>

I would like to thank my Wife, Mckenzie Miller, who has been incredibly supportive of my autophagy research, which has occupied my time and attention since my undergraduate degree, totaling nearly a decade; she has encouraged me through the many challenging times that come with a dual degree program and continues to be my central support system. I thank her for her enduring and unconditional support. I would also like to thank my parents for their selfless and unconditional support over the years.

Guidance Committee

I would also like to thank my esteemed guidance committee members, Dr. Eran Andrechek, Dr. Kathleen Gallo, Dr. Lawrence Olson and Dr. Jeffrey MacKeigan. I appreciate the time and effort they invested in reviewing my work. Their feedback and constructive criticism have been instrumental in shaping my research. I particularly appreciated the unique perspective each of you brought to my project. In addition to their academic support, their encouragement and kindness along this long and unpredictable path has been greatly appreciated. I thank each of them for their constant support.

Administration

I would like to thank the MSUCOM DO/PhD Program particularly Dr. Justin McCormick, Bethany Heinlen, Dr. Brian Schutte and Michelle Volker for providing the opportunity for this life-changing experience. They have tailored a long and arduous journey to my specific needs, and it has been my pleasure to get to know each of you throughout this process. Thank you for your immense support. A special thank you to Jasmine who has gone above and beyond to ensure that I am enrolled and on track for graduation.

TABLE OF CONTENTS

CHAPTER 1: INTRODUCTION

General overview

Autophagy is a process that degrades cytosolic components within cells. This process is essential for proper cell function and organism survival, and has been implicated in various human diseases, including certain cancers and neurodegeneration. (Filippone et al., 2022; Lu et al., 2020; Mathew et al., 2007; Nixon, 2007; Tecalco-Cruz et al., 2022; White, 2015). There are three types of Autophagy including macroautophagy, microautophagy, and chaperone mediated autophagy (Feng et al., 2014; Gross and Graef, 2020; Khandia et al., 2019). This dissertation will only discuss macroautophagy, but the other two are mentioned for completeness.

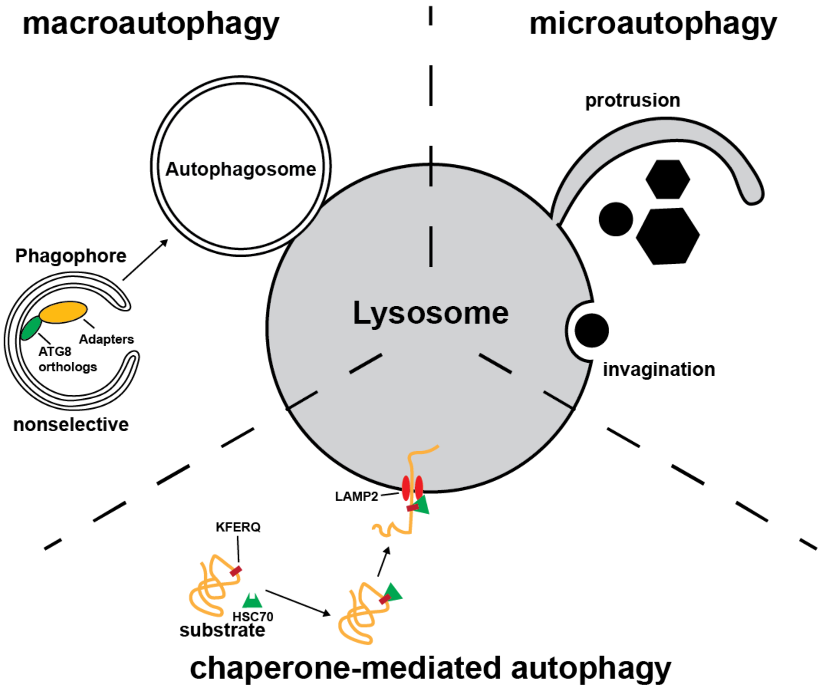

Figure 1.1. Figure depicting the three classes of autophagy. Macroautophagy: Classical autophagy starting with the formation of phagophore assembly site, elongation of the phagophore, and finally closure of the phagophore to form an autophagosome and its subsequent fusion with the lysosome. Microautophagy: the uptake of cytosolic material directly into the endosomal-lysosome system, achieved through invagination or protrusion from the lysosome/endosome. Chaperone-mediated autophagy: Lamp and heat shock protein mediated transfer of proteins from the cytosol into the lysosome for their degradation (Gross and Graef, 2020).

The molecular mechanisms underlying macroautophagy are complex and involve the coordination of multiple autophagy-related proteins, known as the autophagy machinery. Macroautophagy begins with the formation of a cup-shaped structure called the phagophore, which sequesters a heterogenous portion of the cytoplasm, by expanding the phagophore through lipid transfer to form an enclosed, spherical, double-bilipid membrane called the autophagosome (Feng et al., 2014; Ghanbarpour et al., 2021; Lamb et al., 2013; Maeda et al., 2020; Matoba et al., 2020; Matoba and Noda, 2020; Noda, 2021; Yamamoto et al., 2012; Yu et al., 2018). The autophagosome then fuses with a lysosome, where the enclosed cytoplasmic contents are degraded and recycled by lysosomal hydrolases (Lamb et al., 2013; Nakamura and Yoshimori, 2017). The degradation of proteins and organelles within the lysosome increases ATP production and generates new building blocks, such as amino acids and nucleotides, for DNA and protein synthesis, respectively (Guo et al., 2016).

Initiation of macroautophagy is triggered by diverse signals based on the type of cellular stress. Non-selective autophagy is the most studied subtype of macroautophagy, and the primary focus of this dissertation. Non-selective autophagy is triggered when nutrients are scarce, as is clinically observed after exercise, myocardial infarction, and cancer overgrowth (Foglio et al., 2017; Guo et al., 2016; Li et al., 2016; Rocchi and He, 2017). Briefly, aggrephagy, mitophagy, and ER-phagy are a few more macroautophagy subtypes. Collectively, these subtypes differ from the non-selective subtype in that they initiate autophagy to protect against harm brought on by damaged organelles and protein aggregates, thus they specifically degrade proteins, mitochondria, or the endoplasmic reticulum, respectively. While it is impossible to completely isolate selective autophagy from non-selective autophagy, the work done in this dissertation primarily focuses on understanding non-selective autophagy.

While autophagy is shown to have a central role in cellular homeostasis, treatments have yet to be effectively translated to clinic. Clinical trials using autophagy drugs have had significant setbacks over the past decade and have mostly failed mono-therapy approaches (Levy et al., 2017; Mohsen et al., 2022; Towers and Thorburn, 2016). Collectively, the autophagy field has now moved to using autophagy inhibitors as an adjunct therapy approach, but to date, there are very few FDA indicated uses of drugs that target autophagy (Mohsen et al., 2022). With the goal of unlocking the potential of autophagy for the clinic, this dissertation focuses on the development of new methods and tools to quantitatively analyze autophagy biogenesis and elucidate potential targetable pathways.

Three steps of autophagosome biogenesis

Step one: phagophore nucleation

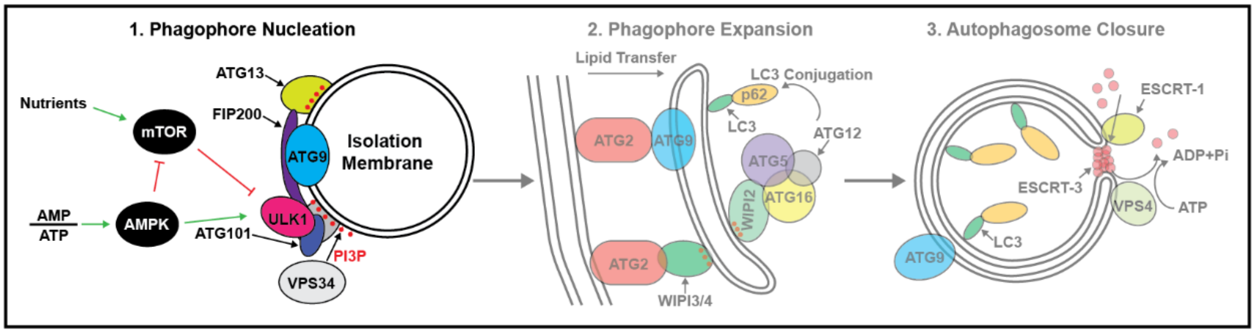

Figure 1.2. Graphic depicting the first step of autophagosome biogenesis. Nutrient deprivation inhibits mTOR through a variety of signals. Downstream ULK1 kinase is the main initiator of autophagy and begins a phosphorylation cascade to recruit autophagy factors to ATG9 vesicles. Growth of the vesicle into the phagophore is dependent on PI3P synthesis by VPS34 within the PI3K complex.

The origin of the phagophore, or the membrane that is expanded into the autophagosome, is a matter of some debate, and two models are predominantly supported. To be accurate, the following characteristics must be contained in each model. First, the phagophore must occur near or on the ER (Ge et al., 2017; Karanasios et al., 2016; Lamb et al., 2013; Tang et al., 2019; Tooze, 2013). Second, the phagophore must have a source of phosphatidylinositol (PI) from the ER, and a portion of that must be converted to PI2P, which in turn be modified into PI3P (Blommaart et al., 1997; Dooley et al., 2014; Fracchiolla et al., 2020). Third, the phagophore must form a double bilipid membrane (Tooze, 2013). Fourth, ATG9 is likely integrated into the phagophore membrane (Ghanbarpour et al., 2021; Maeda et al., 2020; Matoba et al., 2020; Matoba and Noda, 2020; Noda, 2021; Yamamoto et al., 2012). The first model proposed suggests the phagophore is of endoplasmic reticulum (ER) origin (Itakura and Mizushima, 2010; Karanasios et al., 2016). In the ER origin model, the first and second criteria are intuitively satisfied, however, the third may be less straightforward. For the ER origin model to work, there is likely a motorized component to provide the energy to assist in folding the ER onto itself. The fold is the only way to provide the final double bilipid membrane within the final autophagosome structure. While autophagy proteins and autophagosome are known to interact with microtubules and actin elements, no one has described how this mechanism occurs. The ER origin model has yet to provide evidence for ATG9 integration into the phagophore membrane. However, this fourth and final requirement may be debated by some, but there is a growing body of evidence that suggests it is necessary.

Recent Cryo-EM structures of ATG9 revealed a trimeric barrel-shaped structure that serves as a scramblase to balance the inner and outer leaflets of a bi-lipid membrane of expanding autophagosomes (Guardia et al., 2020; Maeda et al., 2020). ATG9 integration is required for the scramblase to function. Apart from one study, microscopy has never identified ATG9 localizing to the ER and thus currently requires an unidentified vesicle-ER fusion step at the PAS (Karanasios et al., 2016). In this dissertation, I will discuss that this was likely an overexpression artefact. Furthermore, few methodologies have identified ATG9 in any significant quantity within the ER membrane including proximity mass spec such as proximity-dependent biotin identification (BioID), conventional sucrose gradient cellular fractionation, or imaging (apart from the one publication) (Kannangara et al., 2021; Orsi et al., 2012). One intriguing study did find that ATG9A phosphatidylinositol synthase-enriched ER subdomains, but this was primarily only when ATG3 was knocked out, and nitrogen fractionation was used which can combine nearby membranes, thus a buildup of ATG9 vesicles near an ER structure could theoretically show up within the fractionation experiment (Nishimura et al., 2017).

The ER origin model was the first to be proposed, and largely relied on live-cell microscopy data showing autophagy markers near the ER. Both models agree that ATG9 recruitment occurs early in autophagosome formation. Early live-cell imaging of ATG9 vesicles suggested that they facilitate the formation of autophagosomes through a dynamic association at the phagophore, and largely remains contradictory the groundbreaking cryo-EM structures. Additionally, sucrose gradient fractionation of cellular material shows more overlap of ATG9 with the Golgi and the ER-Golgi intermediate compartment (ERGIC) compartment.

Alternatively, a newer theory has been proposed, suggesting that ATG9 vesicles are the platform for autophagosome formation. In this model, ATG9 vesicles redistribute from the Golgi during stress and through an unknown mechanism, traffic to the PAS

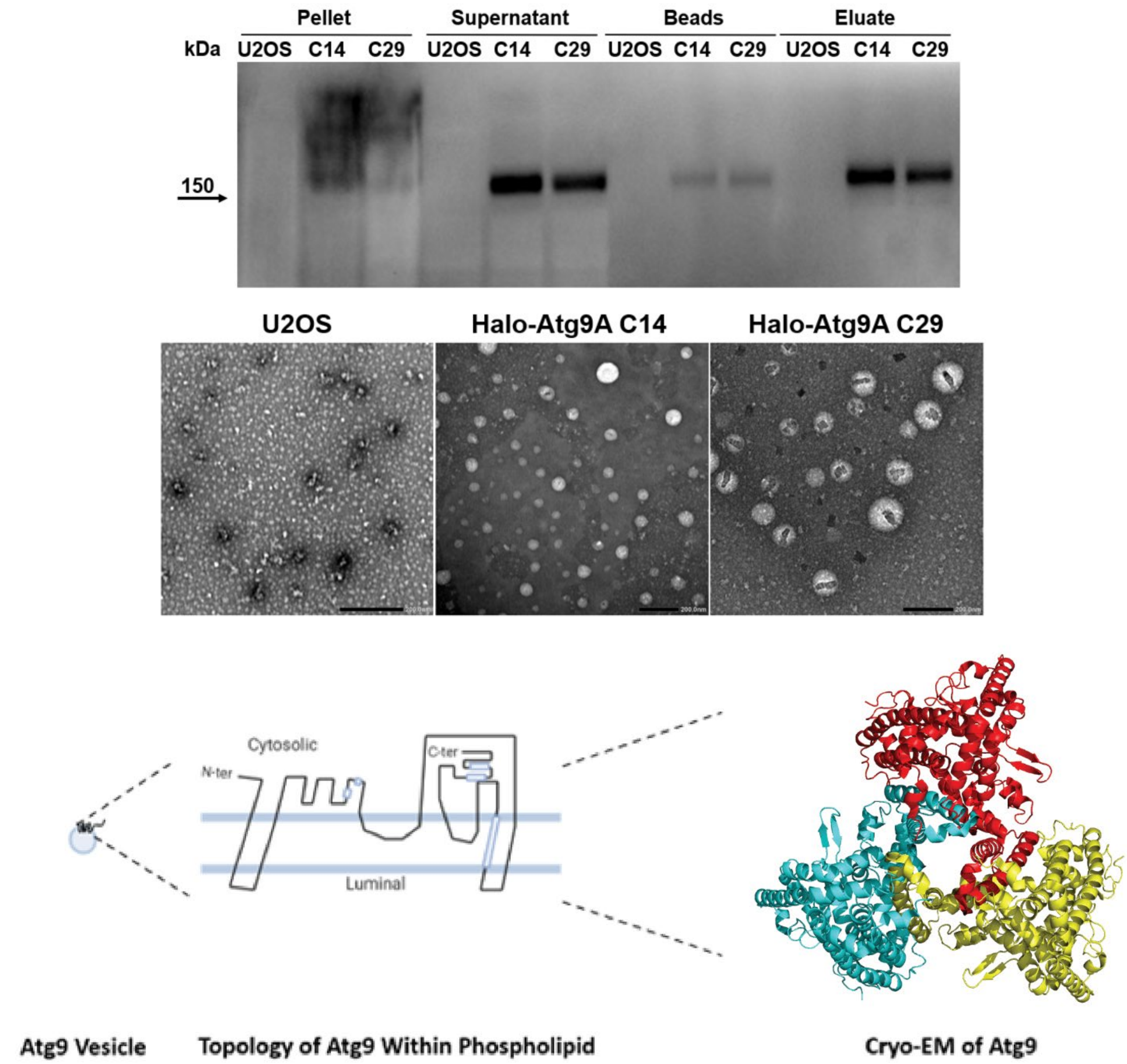

Figure 1.3. Visualizing ATG9A vesicles. Blot showing purified and eluted Halo-ATG9A vesicles that were subsequently imaged by transmission electron microscopy (TEM). Graphic showing increasing magnification of ATG9A from its position on a vesicle, orientation at the membrane interface, and finally its trimeric cryo-EM structure. The lipids are transferred from ATG2A to ATG9A at the central opening and the lipids will be transferred to the inner membrane (PyMOL, version 2.4.0. New York: Schrodinger Inc., 2020). PDB DOI: 10.2210/pdb6WR4/pdb.

where PI3P is enriched on the vesicle membrane and autophagy factors are recruited. As the ATG9 vesicle grows through lipid transfer from ATG2, autophagy factors remodel the membrane into the classical phagophore cup shape, essentially folding the vesicle in on itself to achieve a second membrane. Recent studies looking within ATG2 deficient cells also show large phase separated accumulations of unfused ATG9 vesicles at the PAS, providing further evidence that ATG9 does not integrate into the ER membrane, as would be expected in an ER origin model (Olivas et al., 2022; Tang et al., 2019).

Despite the strong evidence that recently supports the ATG9 vesicle seeding theory, there is data that this theory has yet to contextualize. As autophagosomes form near the ER, many ER resident proteins are excluded from the tubules that contribute to autophagosome formation (Hayashi-Nishino et al., 2009; Ylä-Anttila et al., 2009). In vitro experiments using recombinant protein suggest that these regions contain scramblases that form a lipid transfer complex made of the ER(scramblase)-lipid bridge (ATG2A/B)-Autophagosome(ATG9A) (Ghanbarpour et al., 2021). Imaging has yet to capture this interaction but provides an intriguing potential mechanism where the dense PI synthesis subdomains in the ER funnel lipid to less dense membrane (ATG9 vesicles). This mechanism is speculative and further intracellular studies looking into the contribution of ER subdomains to autophagosome formation is warranted. At the PAS, the models converge and agree that the phagophore is initiated through post-translational modifications, primarily phosphorylation. AMPK, as a primary energy sensor of the cell activates autophagy through many phosphorylations, but some of the better understood targets are mechanistic target of rapamycin (mTOR) and Unc-51 like autophagy activating kinase (ULK1) (Dorsey et al., 2009; Ganley et al., 2009; Mack et al., 2012; Wang et al., 2022; Weerasekara et al., 2014). AMP-activated protein kinase (AMPK) inhibits mTOR, stalling cell cycle, while simultaneously activating ULK1. mTOR is found on lysosomes and is the cell cycle regulator of the cell. Active mTOR blocks autophagy through phosphorylating ULK1.

Amino acid depletion blocks mTOR, causing activation of ULK1 (Hosokawa et al., 2009; Zoncu et al., 2011). Thus, ULK1 activity is tightly regulated by the metabolic health of the cell. The ULK1 protein is critical for the recruitment of the PI3K complex and subsequent PI3P synthesis, the ULK1 kinase function is required for progression through autophagy (Martin et al., 2018; Russell et al., 2013; Zachari et al., 2020). As more PI3P is added to the phagophore, a positive feedback loop is initiated that continuously activates ULK1 and locally enriches PI3P, recruiting additional autophagy factors (Fracchiolla et al., 2020). Within the ULK1 complex, scaffolding protein FIP200 remodels the phagophore into a cup shape that will be expanded into an autophagosome (Ge et al., 2017).

Step two: phagophore expansion

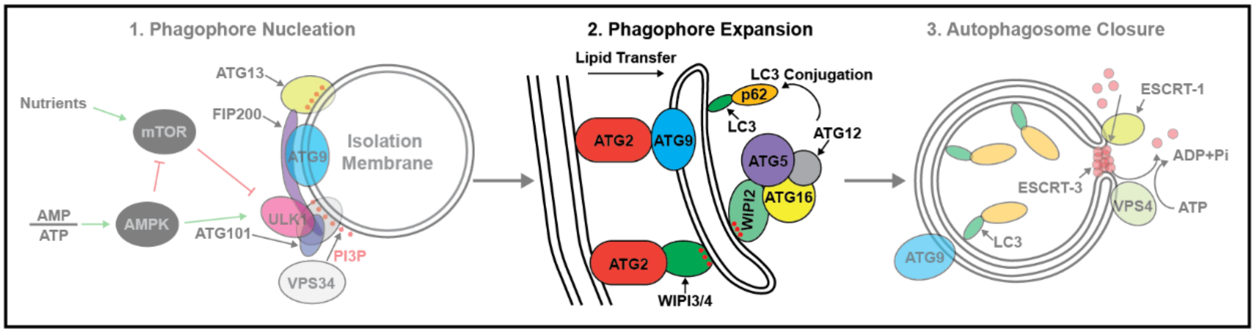

Figure 1.4. Graphic depicting the expansion of the phagophore, primarily through the interactions between ATG2 with ATG9A and ATG2 with WIPI3/4. As the phagophore expands, it is prepared for cargo through the conjugation of ATG8 family members to the autophagosome membrane. ATG8 family members anchor material through interacting with proteins containing LC3 interacting motifs (LIR).

The discovery that ATG9 is a scramblase that acts in concert with ATG2 to transfer lipid catalyzed the characterization of autophagosome membrane elongation, causing an influx of impactful studies characterizing this process (Ghanbarpour et al., 2021; Maeda et al., 2020; Matoba et al., 2020; Matoba and Noda, 2020; Noda, 2021). ATG2 is a large, 250kDA, barrel shaped protein with an -terminal shovel-like domain that scoops lipids through its barrel. At the c-terminus, ATG2 directly interacts with ATG9 which distributes the incoming lipids between the two membrane leaflets (Gómez-Sánchez et al., 2018; Maeda et al., 2019; Noda, 2021; Otomo et al., 2018). This simple mechanism suggests that ATG2 can borrow lipid from other sources, but which membranes donate to autophagosomes remain speculative at this point and the energy source for the directional lipid transport is unclear, since neither ATG9 nor ATG2 have ATPase activity. Like many proposed mechanisms, the reality is likely more complex.

Truncation studies of ATG2 demonstrated that the c-terminus interacts with ATG9, while the n-terminus interacts with ER-resident scramblases (Ghanbarpour et al., 2021). This model is intriguing, as it connects two scramblases with ATG2 acting as lipid bridge, essentially a passive process redistributing the recently synthesized lipid rich ER to autophagosomes. In contradiction, expression of the n-terminus from amino acids 1 to 345 restored autophagosome formation in an ATG2A/B double KO (Valverde et al., 2019). This domain contains the shovel-like domain, but based of other domain mapping publications, it would be unable to bind to ATG9. This demonstrates that the exact role of the ATG2 and ATG9 direct interaction is not fully understood. ATG2 is also recruited to the autophagosome through its interaction with WIPI3-4, but once again, the mutated form that rescues autophagy would once again be unable to bind WIPI3/WIPI4. Thus, the exact contribution of these domains has yet to be fully determined (Ghanbarpour et al., 2021; Otomo et al., 2018).

As ATG2 transfers lipid to the phagophore, the cell prepares the membrane to anchor cargo destined for the lysosome. This is accomplished through the same PI3P synthesis that recruits ATG2 through WIPI3/WIPI4. In this case, the other WIPI isoforms, WIPI1/2 recruit the ATG8 family conjugation machinery, ATG5/ATG12/ATG16 complex (Bakula et al., 2017; Dooley et al., 2014; Proikas-Cezanne et al., 2015; Strong et al., 2021). Conjugation of LC3B was the first ATG8 protein family member characterized, and the rest follow identical conjugation mechanisms (Kabeya et al., 2000; Kabeya et al., 2004). LC3B is transcribed in the cytosol and is immediately cleaved by ATG4 to a more soluble form with a c-terminal glycine (Kabeya et al., 2000). This form of LC3B is the most abundant within the cell and further processing to anchor LC3B to the membrane is accomplished through a mechanism akin to Ubiquitin-activating enzymes. E1 enzymes activate ubiquitin. Activated ubiquitin is then transferred to an E2 enzyme. E3 ligases facilitate the transfer of ubiquitin from the E2-ubiquitin complex to the target protein, marking it for degradation by the proteasome. Similarly, the homodimer ATG7 (E1-like) activates LC3B. LC3B-I is then transferred to ATG3 (E2-like) through an ATG3-ATG7 interaction (Kabeya et al., 2000; Mizushima et al., 2003a; Mizushima et al., 1998; Mizushima et al., 2001; Mizushima et al., 2003b; Tanida et al., 2002; Tanida et al., 2001). For the final step in LC3B-I conjugation, WIPI1/WIPI2 promotes specific conjugation by recruiting the ATG5-ATG12-ATG16 complex (E3-like) through its PI3P interaction, and LC3B is covalently linked to phosphatidylethanolamine (PE) that residues in the phagophore membrane (Dooley et al., 2014; Mizushima et al., 2003a; Mizushima et al., 2001; Mizushima et al., 2003b). This process is reversible, so while it occurs both within and outside of the autophagosome, the remaining LC3B-II will be cleaved by ATG4 to ensure cargo doesn’t bind to the outside of autophagosomes (Hemelaar et al., 2003; Ichimura et al., 2000; Kirisako et al., 1999; Kirisako et al., 2000; Scherz-Shouval et al., 2003). With LC3 coating the growing phagophore, cargo can begin to bind.

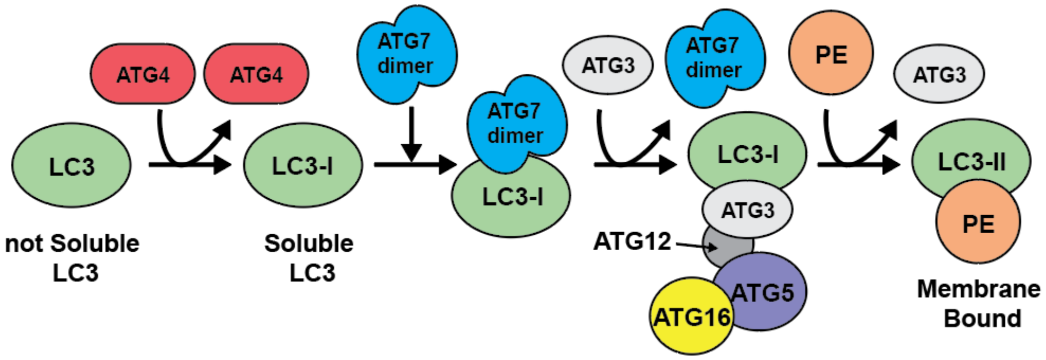

Figure 1.5. Graphic demonstrating the key steps of ATG8 family conjugation to the autophagosome. ATG4 cleaves LC3 to its soluble form containing a c-terminal glycine. ATG7 (E1-like) activates LC3-I. LC3-I is loaded (E2-like) onto ATG3-ATG7. The ATG5-ATG12-ATG16 (E3-like) covalently conjugates LC3-I to membrane bound PE, becoming LC3B-II.

The ATG8 family are small proteins with a C-terminal LIR-docking site (LDS) and the more recent hydrophobic Ubiquitin Interaction motif (UIM) docking site (UDS) (Kirkin and Rogov, 2019; Marshall et al., 2019; Marshall et al., 2022). The LDS and UDS motifs define the cargo that will bind to the ATG8 family. The LDS, refers to proteins containing LC3 interacting motifs (LIR), and includes the many core autophagy adaptors such as P62. The UDS binds to proteins containing UIMs, but is less stringent in its binding and many proteins have low affinity interaction with this site (Manczyk et al., 2017). The UDS remains an active area of research and the number of autophagy adapters continues to grow, but ultimately function to selectively degrade cellular material (Gubas and Dikic, 2022; Johansen and Lamark, 2011; Johansen and Lamark, 2020; Kirkin and Rogov, 2019; Lamark et al., 2017).

Step three: autophagosome closure

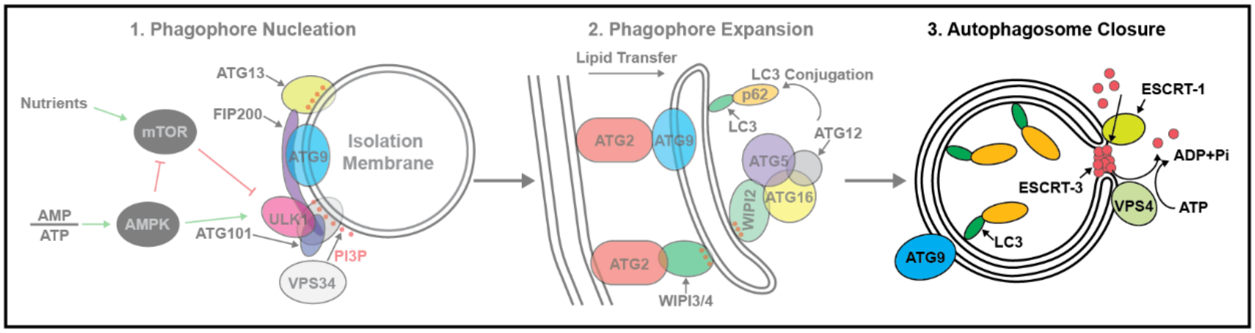

Figure 1.6. Graphical depiction describing autophagosome closure. ESCRT-0 is recruited to ubiquitinated structures. ESCRT-I/II are recruited to mold the membrane for closure. ESCRT-III fills the open gap with a filamentous structure. VPS4 depolymerizes ESCRT-III. Together, the proteins continue to bring the ends closer and closer until the ends fuse.

Autophagosome closure, like lipid transfer, has only recently been characterized. Central to autophagosome closure are the endosomal sorting complexes required for transport (ESCRT) machinery (Chang et al., 2021a; Filimonenko et al., 2007; Lee et al., 2007; Rusten et al., 2007; Takahashi et al., 2018). ESCRT proteins are a group of proteins that play a crucial role in various cellular processes, including the sorting of proteins and the formation of vesicles. ESCRT proteins are involved in the formation of intraluminal vesicles (ILVs) within multivesicular bodies (MVBs) and their subsequent fusion with lysosomes (Vietri et al., 2020). They are also involved in cytokinesis, viral budding, and exosome secretion pathways (Vietri et al., 2020).

ESCRT proteins act in a sequential and hierarchical manner (Melia et al., 2020). The first ESCRT complex to be recruited is ESCRT-0, which recognizes and binds to ubiquitinated cargo proteins on the cytosolic side of the endosomal membrane. This complex then recruits ESCRT-I and ESCRT-II, which work together to deform the membrane and form a budding vesicle. Finally, ESCRT-III is recruited, which forms a filamentous complex that drives the scission of the vesicle from the endosomal membrane.

With some overlap, ESCRT-I components (VPS37A and VPS28) shapes membrane for closure through recruitment of ESCRT-III proteins, such as chromatin-modifying protein/charged multivesicular body protein 2A (CHMP2A) and the filament-forming subunit CHMP4B (Zhen et al., 2020). In colloquial terms, these together form the glue that fills the void between the edges of the phagophore. The ends of the phagophore will be brought progressively closer as VPS4 depolymerizes the ESCRT-III complex (Chang et al., 2021a; Melia et al., 2020).

Single molecule and single particle principles

Limitations in conventional microscopy and image analysis

Fluorescence microscopy has been a tremendously useful tool to understand protein function in cells. In particular, this has been true for autophagy, where the majority of autophagy factors are not involved in autophagosome formation at any given time, and visualization of autophagosomes by florescence microscopy more effective at studying regions of interest compared to autophagosome purification (Itakura and Mizushima, 2010). The appearance of early autophagy protein foci, and the segue to autophagosome marker foci represent the three stages of the autophagosome that are mentioned above. As foci, the differences are not appreciated due to the diffraction limit of light microscopy (200-300 nm). Thus, the resolution cannot be improved through magnification with light alone. This, unfortunately, is a main limitation to conventional microscopy and super resolution solutions have yet to become mainstream within the autophagy field.

Dr. Ricardo Henriques, a prominent microscopist that specializes in the development and implementation of super resolution techniques, provided a phenomenal example of why conventional microscopy can often be misleading. In his experiment he compared a ground state total internal reflection fluorescence (TIRF) image to that of a super resolution reconstruction of a t-cell synapse (Henriques, 2022). When colocalizing at ground state all the proteins show bright colocalization, however, at super resolution none of these signals overlapped. Thus, the significance of colocalization with a resolution limited to 200 nm may not be the most reliable approach to use when characterizing cellular mechanisms. Furthermore, colocalization is often paired with cross-linking fixation agents such as PFA, formaldehyde, methanol etc. and can dramatically change protein localization.

The limitations of conventional microscopy are relevant to autophagy, which has relied on and continues to use conventional localization studies to understand the biogenesis of autophagosomes. Autophagy factors form foci near the ER, yet inherently, for this to be true, ATG proteins are close to the ERGIC, Golgi, microtubules, actin filaments, and the plasma membrane (Itakura and Mizushima, 2010; Karanasios et al., 2016). In this work, I primarily use live-cell imaging which avoids the common fixation artifacts and adds temporal information allowing co-diffusion studies.

HaloTag/SNAPTag biology and highly inclined and laminated optical sheet (HILO) microscopy

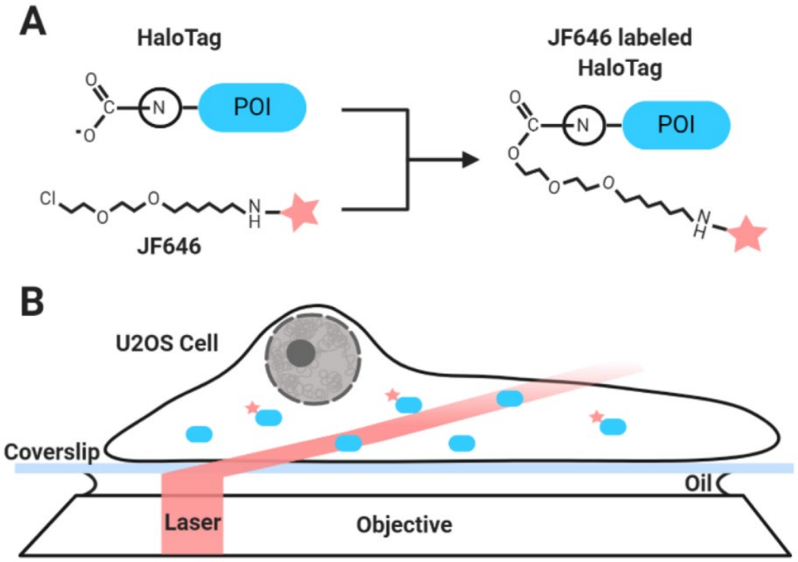

Figure 1.7. Graphic demonstrating single molecule principles (**A**) Example of the covalent bond that forms between the HaloTag and its respective ligand, in this case JF646 is shown. (**B**) Graphic showing the two key components for HLO imaging: a TIRF laser with an increased angle that illuminates the cytosol and sub-labeling of the protein of interest.

To minimize potential artifacts, provide accurate imaging, and enable pulse-chase experiments, both the HaloTag and SNAPTag were utilized for endogenous protein tagging, as described later in this dissertation. These two tags are unique compared to traditional fluorescent tags used in live-cell imaging. While the chemistry of HaloTag and SNAPTag differs, the general principle is the same: the tags have a carboxyl group that performs a nucleophilic substitution with a specific substrate, forming a covalent bond between the enzyme and the substrate (Juillerat et al., 2003; Los et al., 2008; Los and Wood, 2007). Importantly, these substrates can be chemically attached to numerous small molecules allowing customization of the HaloTag and SNAPTag to perform a variety of purposes, and the SNAP and Halo Ligands do not cross-react. In this dissertation, I widely use small, permeable, fluorescent Janelia Flour (JF) molecules ranging from 503-650 nm for their excitation wavelength maximum.

	Excitation Wavelength	Emission Wavelength	QY	EC	QY X EC	Relative Brightness
eGFP	488	510	0.6	55900	33540	0.32
mNeonGreen	505	517	0.8	116000	92800	0.88
mCherry	586	610	0.22	72000	15840	0.15
mRuby3	557	595	0.45	128000	57600	0.55
E2-Crimson	610	643	0.23	126000	28980	0.28
eBFP	380	443	0.2	31500	6300	0.06
mTagBFP2	400	456	0.64	50600	32384	0.31
JF503-Halo	503	532	.821	31000	25451	0.24
JFX554-Halo	554	582	0.64	164000	104960	1.00
JFX650-Halo	650	671	0.81	99000	80190	0.76

Table 1.1. Compiled table of useful information for selecting tags (Lambert, 2019). QY – Quantum Yield, EC – Extinction Coefficient, relative brightness is in relation to JFX554 (the brightest fluorophore) (Grimm et al., 2015; Grimm et al., 2016)

HaloTag and SNAPTag, in combination with JF dyes, have numerous advantages over conventional fluorescent tags, such as eGFP. First, many of the dyes are brighter, which is especially true when comparing red shifted fluorescent tags. For instance, JFX554 is ~7 times brighter than mCherry (calculated by quantum yield x extinction coefficient). I have found brightness is an important factor when working with endogenously tagged proteins which tend to have substantially lower levels of expression when compared to overexpression. Second, once the small molecule ligand forms a covalent bond with its paired enzymatic tag, standard western blot conditions do not affect its fluorescence, and thus fluorescence can be measured within an SDS-PAGE gel. Third, because the tags are not fluorescent on their own, they allow research to use pulse-chase methods in their studies. One peculiar difference between the Halo and SNAP tags is that once the HaloTag is bound to its ligand, it becomes protease resistant allowing it to survive within the harsh conditions of the endosome-lysosome system. Alternatively, the SNAPTag does not have this characteristic. Thus, depending on the study, researchers may opt for one or the other depending on the population of the protein of interest that one is trying to study. Fourth, since the tags require an enzymatic reaction to become fluorescent, the ligands can be titrated to label a subset of the tags, allowing for visualization of only a portion of the existing protein.

Being able to label a sub-set of protein is particularly useful when combined with highly inclined and laminated optical sheet (HILO) imaging and allows the visualization of bright single molecules that can be accurately localized and tracked. In this dissertation, I leverage the advantageous characteristics of the HaloTag and SNAPTag to overcome the colocalization challenges described above and utilize novel methodology to provide a quantitative perspective to the complex and heterogenous process of autophagy.

Clinically Targeting of Autophagy

Introduction

Pharmaceutically manipulating autophagy for the benefit of patients remains limited in clinical practice. While the strategies and novel drugs to target autophagy have improved over time, many have not been successful in clinical trials, thus the drugs used clinically have not changed for many years and are all derivatives of two general mechanisms: inhibiting mTOR (blocking proliferation and inducing autophagy) or de-acidifying the lysosome (blocking autophagosome fusion and subsequent degradation). These strategies will be briefly discussed and most of the described benefits may be functioning in the clinic independent of macroautophagy regulation. It likely will require more specific targets to truly dissect the beneficial role of targeting macroautophagy for therapeutic purposes.

Role of mTOR inhibition for organ transplant recipients

Discussions of Immunology does not encompass the primary goal of this dissertation but is considered here for understanding the importance of mTOR inhibition in the clinic. The common indication for mTOR inhibition, in this case by rapamycin, is to reduce the chance of transplant rejection (heart, lung, liver, kidney etc.) through suppressing the immune system. A simple and direct mechanism to explain this phenomenon is through reducing the proliferation of immune cells. Because active mTOR is required for cell cycle progression, mTOR inhibition affects cell types of both the innate and adaptive immune cells. The effect of mTOR on different immune cells, however, is dramatic and specific to cell type.

For example, it is proposed that Antigen Presenting Cells (dentritic cells, macrophages, B-cells), are particularly affected by mTOR inhibition through downregulation of phagocytosis, endocytosis, and pinocytosis, essentially blocking the uptake of extracellular material that would otherwise be loaded onto MHC-II for T-cell and B-cell activation. Additionally, mTOR also affects MHC-II expression and CD86, a T-cell co-stimulatory receptor, reducing key proliferative signals for T-cells and B-cells. Many other mechanisms of how Rapamycin affects the adaptive and innate immune systems are discussed in length elsewhere and won’t be considered further here.

While many mechanisms have been proposed, clinicians primarily think that the main contribution of rapamycin for treating transplant rejection is through blocking the downstream transcription factor NFKbeta. There is strong clinical evidence for this line of thinking. Rapamycin is not the first-line medication when looking to suppress the immune system. Rather calcineurin inhibitors (CNIs) such as Tacrolimus or cyclosporine A. When comparing clinical trials, tacrolimus is as effective as cyclosporine A, but with fewer side effects, while both drugs are superior in efficacy compared to rapamycin. These two classes are thought to suppress the immunes systems by controlling transcription factors that stimulate the production of Interleukin-2 (IL-2), a potent excreted activator of T-cells. CNIs and mTor inhibitors regulate NFat and NFKbeta, respectively, but as previously mentioned, NFat is the primary target for treatment.

There are two scenarios, however, when clinicians may prefer rapamycin for suppressing the immune system. The first is when patients are at risk for kidney failure. CNIs cause renal fibrotic deposition which overtime can ultimately lead to kidney failure. Alternatively, rapamycin does not have this affect, and can be combined with a low dose CNI. The second scenario occurs when patients are diagnosed with a malignancy caused by immune suppression. Once again, a combination of low does CNI and rapamycin can be combined to somewhat stimulate the immune system while retaining a healthy transplant. Thus, mTOR inhibition is useful for suppressing T-cell and B-cell activation in the described scenarios; these affects appear to be independent of the induction of macroautophagy. It also demonstrates how mTOR inhibition decreases the proliferation of cancer cells, it also impairs the immune system, and mTOR inhibitors for monotherapy have failed. As an adjuvant therapy, mTOR inhibitors have had some success but the cancers they are used for are varied and contain specific mutations which is out of the scope of this manuscript.

Indications for deacidification of the lysosome

To study autophagy, Bafilomycin A1, an ATPase inhibitor that prevents acidification and fusion of autophagosomes with lysosomes is primarily used. However, chloroquine or hydroxychloroquine are the primary drugs used in clinical trials, due to their safety profile. Initially, chloroquine and hydroxychloroquine have been used to treat malaria, and function through blocking acidification of the parasite’s food vacuole. Both drugs are no longer used for this purpose because they have no effect on trophozoites within the liver, and malaria is substantially now resistant to chloroquine derivatives. More recently, hydroxychloroquine has been repurposed for inflammatory conditions including systemic lupus erythematous (SLE) and rheumatoid arthritis (RA). Additional off label indications include other inflammatory conditions such as dermatomyositis, Porphyria cutanea tarda, Primary Sjögren syndrome (extraglandular manifestations), Q fever (Coxiella burnetii), Sarcoidosis. The use of hydroxychloroquine in cancer has been increasing, and some studies suggest that adjuvant treatment does increase some survival metric for some cancer. Even so, there are no standard of treatment indications for hydroxychloroquine in cancer currently.

CHAPTER 2: QUANTITATIVE ANALYSIS OF AUTOPHAGY REVEALS THE ROLE OF ATG9 AND ATG2 IN AUTOPHAGOSOME FORMATION

(Accepted for publication in the Journal of Cell Biology 03/17/2023

Abstract

Autophagy is a catabolic pathway required for the recycling of cytoplasmic materials. To define the mechanisms underlying autophagy it is critical to quantitatively characterize the dynamic behavior of autophagy factors in living cells. Using a panel of cell lines expressing HaloTagged autophagy factors from their endogenous loci, we analyzed the abundance, single-molecule dynamics, and autophagosome association kinetics of autophagy proteins involved in autophagosome biogenesis. We demonstrate that autophagosome formation is inefficient and ATG2-mediated tethering to donor membranes is a key commitment step in autophagosome formation. Furthermore, our observations support the model that phagophores are initiated by the accumulation of autophagy factors on mobile ATG9 vesicles, and that the ULK1 complex and PI3-kinase form a positive feedback loop required for autophagosome formation. Finally, we demonstrate that the duration of autophagosome biogenesis is approximately 110 seconds. In total, our work provides quantitative insight into autophagosome biogenesis and establishes an experimental framework to analyze autophagy in human cells.

Introduction

Autophagy is a conserved catabolic process that recycles damaged organelles and protein aggregates, or non-specifically degrades cellular material to provide nutrients for cell proliferation, particularly when cells face chemical stress or nutrient starvation (White, 2015; Yu et al., 2018). The hallmark of autophagy is the formation of double-membrane autophagosomes, which sequester cargo and then fuse with lysosomes to trigger the degradation of their contents. Alterations of autophagy have been implicated in the pathology of several human diseases. During the aging of human cells, key autophagy factors are reduced in abundance resulting in the downregulation of autophagic flux which increases the susceptibility to the two most common neurodegenerative disorders, Alzheimer's and Parkinson's disease (Filippone et al., 2022; Lu et al., 2020; Nixon, 2007; Tecalco-Cruz et al., 2022). In contrast, the upregulation of autophagy has been shown to promote a variety of cancers by providing nutrients for rapid tumor proliferation (Gewirtz, 2014). The life cycle of autophagosomes encompasses four distinct steps: phagophore initiation, expansion, and closure forming a mature autophagosome, followed by fusion of the autophagosome to the lysosome leading to its degradation.

Autophagosome formation can be initiated non-specifically (non-selective autophagy) or by a target, for instance, a damaged organelle, that requires degradation (Kirkin, 2020; Lamb et al., 2013). Non-selective autophagy is induced under starvation conditions or by chemical stress (Lamb et al., 2013). Initially, it was suggested that specific regions of the endoplasmic reticulum (ER) are remodeled into the phagophore (Ge et al., 2017). An alternative hypothesis suggests that the phagophore is formed by ATG9-containing vesicles, which expand to form a mature autophagosome (Chang et al., 2021a; Chang et al., 2021b; Olivas et al., 2022; Sawa-Makarska et al., 2020; Tang et al., 2019). ATG9 is the only known autophagy-related protein that contains a transmembrane domain and has recently been shown to have lipid scramblase activity, which facilitates the exchange of phospholipids between the outer to the inner leaflets of the membrane it is embedded in (Ghanbarpour et al., 2021; Maeda et al., 2020; Matoba et al., 2020; Matoba and Noda, 2020; Noda, 2021; Yamamoto et al., 2012). For this reason, ATG9 vesicles are prime candidates for the origin of the phagophore; as ATG2 transfers lipids to the outer leaflets, ATG9 equilibrates lipids across the membrane, growing a vesicle into an autophagosome (Maeda et al., 2019; Maeda et al., 2020; Matoba et al., 2020; Matoba and Noda, 2020; Noda, 2021; Osawa et al., 2019; Valverde et al., 2019). Regardless of the membrane structure autophagosomes originate from, non-selective autophagy is initiated through a complex phosphorylation cascade by the Unc-51 like autophagy activating kinase (ULK1/2) complex. Besides ULK1/2 isoforms, the Ulk1-kinase complex is composed of FIP200, ATG13, and ATG101 (Ganley et al., 2009; Mercer et al., 2009; Shi et al., 2020). The ULK1 substrates include many downstream autophagy factors, and these phosphorylation sites serve as key switches for autophagy protein recruitment to the phagophore (Ganley et al., 2009; Mercer et al., 2018; Mizushima, 2010).

One essential step that drives autophagosome biogenesis is the activation of the PI3K complex at the phagophore, which modifies phospho-inositol lipids leading to a local enrichment of PI3P (Mizushima, 2010). The presence of PI3P is sensed by the WIPI3/4 proteins, which subsequently recruit the lipid transferase ATG2 to the growing phagophore (Chowdhury et al., 2018; Dooley et al., 2014; Otomo et al., 2018). In addition to ATG2, WIPI1-4 also recruits the ATG5-ATG12-ATG16 complex (Fracchiolla et al., 2020; Lystad et al., 2019), which acts similarly to ubiquitin ligase complexes but instead conjugates ATG8 family (e.g. LC3 and GABARAP) proteins to phosphatidylethanolamine at the phagophore membrane (Hanada et al., 2007; Kirisako et al., 1999; Shpilka et al., 2011). Once conjugated to the phagophore membrane, LC3 and GABARAP proteins serve as anchors to tether cargo targeted for degradation to the autophagosome (Schaaf et al., 2016). Finally, when expansion and cargo sequestration are complete, the phagophore closes into the double-membrane autophagosome and fuses with the lysosome to trigger the degradation of its contents (Berg et al., 1998; Nakamura and Yoshimori, 2017).

In this study, we establish a collection of genome-edited cell lines that express endogenous HaloTagged autophagy proteins involved in autophagosome biogenesis. This approach maintains the expression levels of the tagged autophagy factors and retains all regulatory mechanisms conferred by the endogenous genomic locus of the respective gene and avoids potential artifacts caused by transgene overexpression. The HaloTag is a versatile protein tag that can be covalently linked to cell-permeable ligands, which facilitates fluorescent labeling, targeted protein degradation, and pulse-chase experiments. Using our collection of cell lines, we systematically quantify the absolute abundance, single-molecule diffusion dynamics, and the recruitment kinetics of these autophagy proteins to the phagophore. The results show that ULK1 and ATG2A are maintained at low expression levels, potentially to prevent uncontrolled autophagosome production, and are key signals in committing the phagophore into developing into an autophagosome. Our live-cell single-molecule imaging experiments reveal that the initiation of autophagosome formation is locally controlled, rather than by cell-wide changes in signaling. Furthermore, we demonstrate that ATG9A is the only autophagy factor that is not locally enriched at sites of autophagosome formation, suggesting that a limited number of ATG9A molecules, potentially those contained in a single ATG9-vesicle, are required in autophagosome formation. Our systematic analysis of autophagy factor foci kinetics reveals that the average duration of autophagosome biogenesis is approximately 110 seconds and that most phagophores do not progress to form mature autophagosomes. In addition, we observe two classes of phagophore foci with distinct diffusion dynamics. Rapidly moving pre-phagophores, which are likely mobile ATG9A vesicles that have begun to recruit autophagy factors and phagophores that move more slowly as a result of ATG2A-mediated tethering to lipid donor membranes. Importantly, we show that ATG9A accumulates within the lysosome over time, where it is degraded, suggesting ATG9A integration into the autophagosome is required for autophagosome expansion. In total, our work supports a model in which the phagophore is initiated by the accumulation of autophagy proteins on mobile ATG9A-containing vesicles which proceed to be tethered to lipid donor membranes by ATG2A, committing the phagophore to maturation into an autophagosome. In addition, we establish a sophisticated experimental framework for the quantitative analysis of autophagy in human cells.

Results

Genomic Insertion of HaloTag at Endogenous Loci of Autophagy Proteins

To quantitatively analyze autophagosome formation in human cancer cells (U2OS), we used CRISPR-Cas9 mediated genome editing to introduce the HaloTag into the endogenous loci of autophagy factors that are involved in the phagophore initiation (ULK1, ATG13, PI4K3β), lipid transfer into the growing phagophore (ATG2A and ATG9A), and LC3 conjugation (WIPI2, ATG16, ATG5, LC3) (**Fig. 2.1A**). Homozygous insertion of the HaloTag was confirmed by PCR and Sanger sequencing (**Appendix Fig. 10A-B**), and exclusive expression of the HaloTagged autophagy proteins was validated by western blot and fluorescent labeling (**Fig. 2.1B,C**). Due to their sequence complexity, we were unable to confirm homozygous editing of *WIPI2* and *ULK1* loci using PCR amplification. Instead, we validated the specificity of integration and exclusive expression of HaloTagged WIPI2 and ULK1 protein (**Appendix Fig. 10C, Fig. 2.1B**). We attempted to tag DFCP1, and subunits of the PI3K complex, including Beclin-1 and VPS34, but we failed to generate clonal cell lines that exclusively expressed the HaloTagged proteins.

To determine the expression levels of the HaloTagged autophagy proteins relative to the wildtype protein using western blots we lysed cells and removed the HaloTag using the TEV protease before gel electrophoresis. This approach avoids artifacts that we observed caused by the HaloTag affecting western blot transfer or antibody detection of the autophagy proteins (**Appendix Fig. 10D-E**). The majority of HaloTagged autophagy factors were expressed at similar levels to their untagged counterparts (**Appendix Fig. 10D-E**). Halo-ULK1 was approximately 4-fold overexpressed and Halo-WIPI2 expression

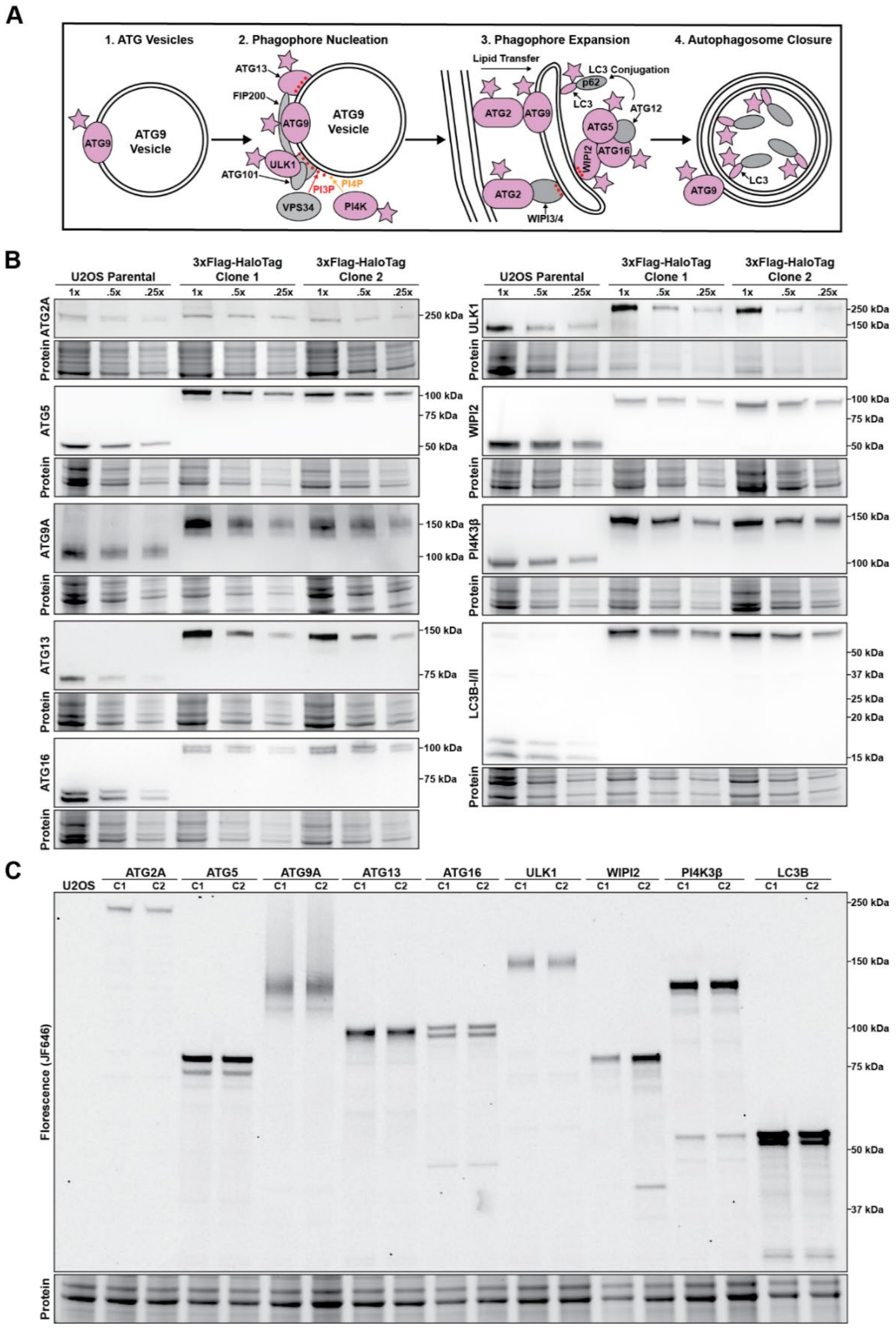

Figure 2.1. A HaloTag-based platform for quantitative analysis of autophagy in human cells. (**A**) Model showing autophagy factors and the complexes they form from phagophore initiation, towards phagophore expansion and autophagosome closure.

Figure 2.1. (cont'd) Proteins tagged in this study are indicated in pink. D.G.B., J.S. (**B**) Western blots of autophagy proteins showing size shift of the tagged protein and exclusive expression of the tagged protein in comparison to the parental U2OS cell line. Three concentrations (100, 50, and 25% of initial lysis volume) were loaded on the gel. D.G.B., C.B. (**C**) Fluorescence gel showing gene tagging; two distinct monoclonal lines (C1 and C2) were selected for each edited gene. Cell lines were labeled with saturating amounts of HaloTag ligand JF646 (250nM, 30min). D.G.B., C.B.

was reduced by ~50% (**Appendix Fig. 10D-E**). Due to the sequence complexity of the *WIPI2* locus, likely not all the *WIPI2* alleles were modified causing a reduction in gene dosage. Importantly, Halo-LC3 appeared to be more abundant than wildtype LC3 but the removal of the HaloTag by TEV cleavage eliminated the difference in the western blot signal (**Appendix Fig. 2.10D-E**). This demonstrates that the HaloTag can have a significant impact on the detection of proteins by western blot. This difference is likely caused by an alteration in western blot transfer efficiency.

Altogether these observations demonstrate that we have successfully generated a collection of cell lines expressing HaloTagged autophagy proteins from their endogenous loci at or near the levels of their wildtype counterparts.

The HaloTagged autophagy proteins are functional

Our quantitative western blots shown above demonstrate that our cell lines exclusively express HaloTagged autophagy proteins and allow us to evaluate whether fusion to the HaloTag affected their function in autophagy. To test the functionality of the HaloTagged autophagy proteins we determined the efficiency of autophagosome formation and degradation by measuring the levels of membrane-conjugated LC3 after autophagy induction by rapamycin with and without the lysosome inhibitor bafilomycin, which prevents autophagosome degradation (Barth et al., 2010; Yamamoto et al., 1998). LC3 western blots showed that apart from HaloTagged-ATG5, where we observed a minor conjugation defect, all cell lines expressing HaloTagged autophagy factors conjugated

LC3 to a similar degree as the parental U2OS cells (**Appendix Fig. 10F**). To verify the colocalization of tagged autophagy proteins with a well-established autophagosome marker, cells were incubated with fluorescent HaloTag-ligand (JF646) alongside baculovirus-mediated transient expression of GFP-LC2. Surprisingly, GFP-LC3 did not form foci indicative of autophagosome formation, when combined with N-terminal tags on the conjugation machinery including ATG5, ATG16, and WIPI2 (**Appendix Fig. 11A**). All the other tagged proteins formed puncta that colocalized with GFP-LC3 foci and responded similarly to the parental cell line when treated with rapamycin and bafilomycin (**Appendix Fig. 11A**).

Since we did not observe any defects in LC3 conjugation by western blot in Halo-ATG16 and Halo-WIPI2 cells, we hypothesized that the HaloTag sterically interferes with the conjugation of GFP-tagged LC2. To test this hypothesis, we analyzed LC3 foci formation by immunofluorescence (IF) instead of GFP-LC2. Using IF we detected similar numbers of LC3 foci within the Halo-ATG5, Halo-ATG16, and Halo-WIPI2 cell lines compared to parental U2OS cells, confirming that these HaloTagged autophagy factors can fully support endogenous LC3 conjugation (**Appendix Fig. 11B**). The formation of foci in response to autophagy induction is a characteristic of autophagy proteins (Karanasios et al., 2013a). In contrast to the LC3 foci number, which increased in response to rapamycin treatment (**Appendix Fig. 11E**), we did not observe increases in the number of foci formed by other HaloTagged autophagy proteins. HaloTagged ATG2A, ATG13, ULK1, and LC3 foci number was only slightly increased in rapamycin-treated samples while HaloTagged ATG5, ATG9A, and ATG16, showed no increase in foci formation (**Appendix Fig. 11D**). These observations suggested that inhibition of mTOR with rapamycin did not activate autophagy sufficiently to cause an increase in foci formation in our endogenously tagged cell lines.

To induce autophagy using a more robust approach, we treated cells with Earl's Balanced Salt Solution (EBSS), which triggers autophagy primarily by amino acid starvation. After treatment with EBSS, the number of foci formed by all HaloTagged autophagy factors was increased compared to cells grown in complete media (**Appendix Fig. 11C**). Strikingly, while the number of Halo-WIPI2 and Halo-ULK1 foci did not change after rapamycin treatment, amino acid starvation using EBSS lead to a 4-fold increase in the number of Halo-ULK1 and Halo-WIPI2 foci. When imaging Halo-PI4K we were unable to identify discreet foci but observed an accumulation of Halo-PI4K in the perinuclear region of the cytoplasm (**Appendix Fig. 11C, F**). This result differed from previous imaging experiments using stable expression cell lines to visualize PI4K (Judith et al., 2019). Notwithstanding, we observed a peri-nuclear redistribution of Halo-PI4K upon both rapamycin and amino acid starvation, which agrees with previous findings (Judith et al., 2019).

In total, these results demonstrate that the tagged autophagy factors are functional and support autophagosome formation. Only Halo-ATG5 showed a minor defect in the overall level of LC3 conjugation (**Appendix Fig. 10F**).

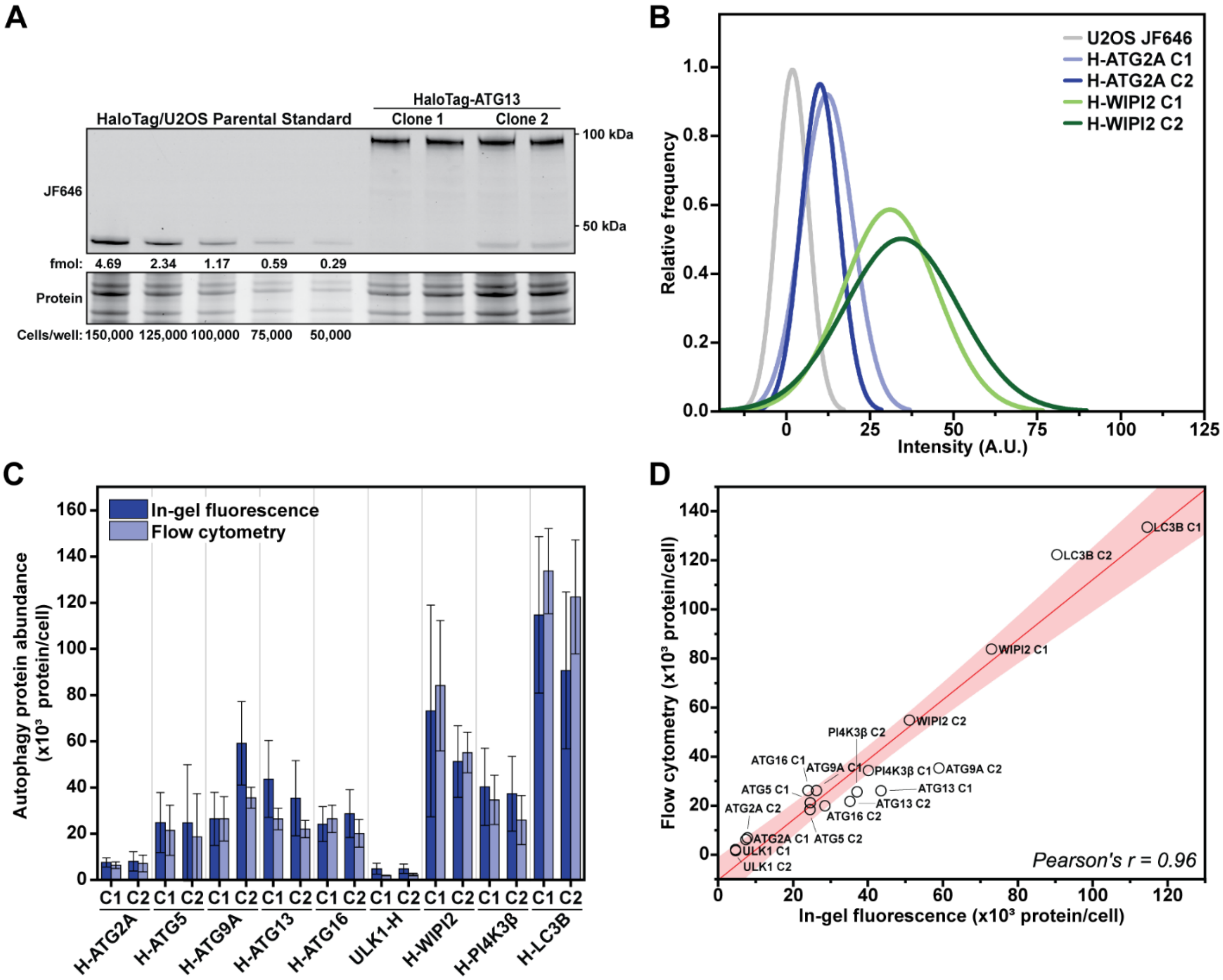

Figure 2.2. Absolute protein abundance quantification of autophagy factors in human cells. (**A**) Example in-gel fluorescence containing the quantification standards (HaloTag + cell lysate) and ATG13 protein. D.B. (**B**) Histogram of flow cytometry measurements depicting the relative protein abundances of U2OS (negative control), and two clones of cells expressing Halo-ATG2A, and Halo-WIPI2. D.G.B., C.B. (**C**) Corrected Protein abundance quantification of the tagged autophagy proteins with in-gel fluorescence and flow cytometry (N = 3, Mean ± SD including error propagation). D.G.B., C.B. (**D**) Graph showing the correlation between protein abundance measured by flow cytometry compared to in-gel fluorescence. D.G.B., C.B.

Quantification of the absolute abundance of autophagy proteins

To determine the absolute number of protein molecules per cell for each tagged autophagy factor, we expanded upon an established in-gel fluorescence method to quantify the number of HaloTagged molecules per cell (**Fig. 2.2A**) (Cattoglio et al., 2019). To avoid the recombinant expression of each HaloTagged autophagy protein to use as a quantification standard, we supplemented U2OS cell lysates of a known number of cells with purified, recombinantly expressed 3xFLAG-HaloTag protein (**Fig. 2.2A, Appendix Fig. 12A-D**). Standard curves for the cell number using total protein levels and HaloTag-fluorescence signal were reproducible across all experiments with R^2 values of 0.99 (**Appendix Fig. 12E**). To account for biases introduced by the banding patterns in fluorescence gels and differences in transfer efficiencies of HaloTagged proteins, we cleaved the fusion proteins using TEV protease. This approach allowed us to calculate correction factors by comparing the signal of the cleaved HaloTag (fluorescence signal) and autophagy factor (western blot signal) to the HaloTag standard and endogenous autophagy protein signal, respectively (**Appendix Fig. 10D**, **Appendix Fig. 12F-G**).

The in-gel fluorescence method allowed the quantification of autophagy protein abundance in U2OS cells over a broad range, from low expressed factors (ULK1, ~3,000 proteins/cell; ATG2A, ~8,000 proteins/cell), to the highly expressed LC3 (>100,000 proteins/cell). ATG16 and ATG5 were present in a 1:1 ratio, consistent with their constitutive association. WIPI2, a scaffold protein that recruits ATG16-12-5 to the initiation membrane, was present in ~5-fold excess relative to ATG16. Surprisingly, ATG13 exceeded the abundance of ULK1 9-fold (**Fig. 2.2C**), considering that both proteins are part of a larger kinase complex (the ULK1 complex) (Mizushima, 2010).

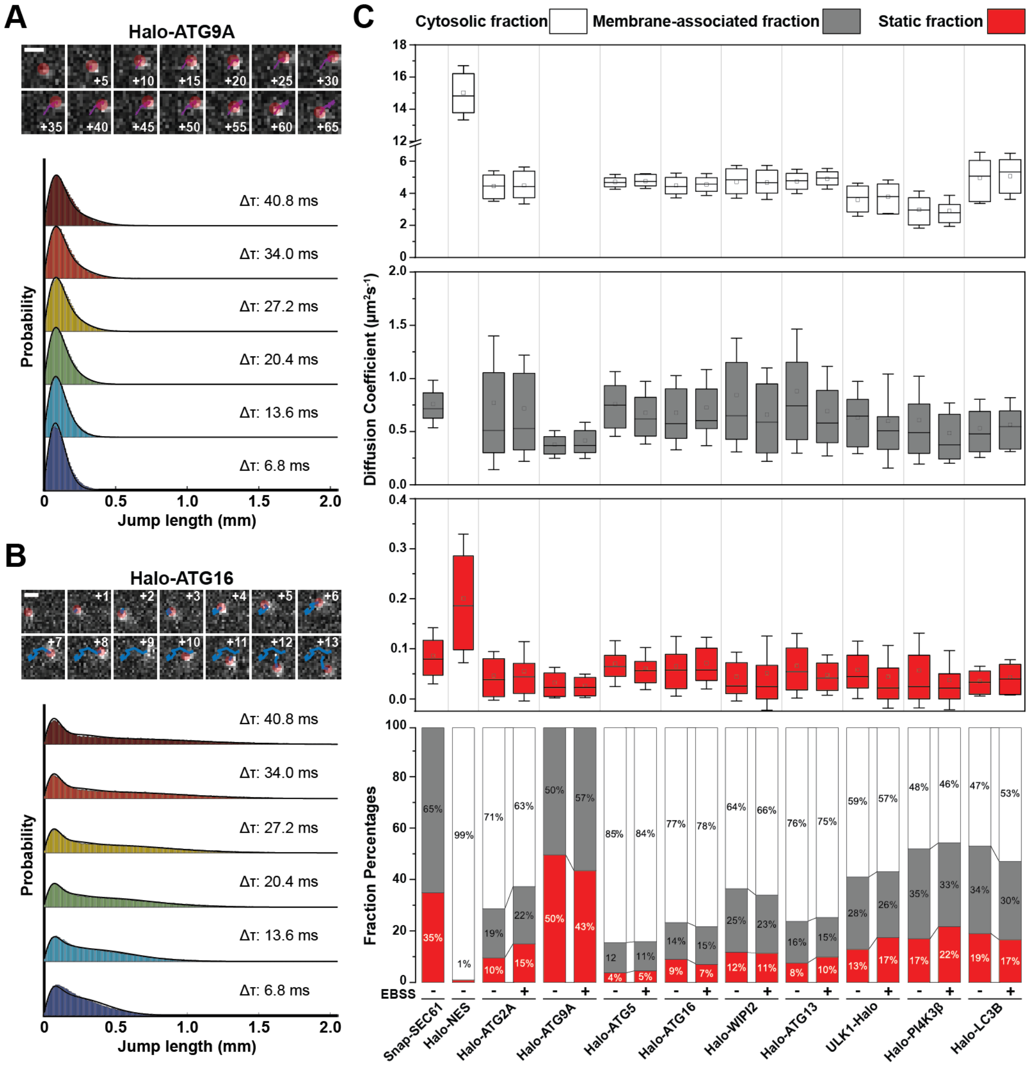

Figure 2.3. Live-cell single-molecule analysis of autophagy proteins. (**A-B**) Example of single-particle tracking of (**A**) ATG9 and (**B**) ATG16, and the corresponding fitting of the step-size probability distribution with SpotON algorithm. D.G.B., C.B., J.S. Numbers inside the micrographs indicate the imaging frame associated with the track. Movies were acquired at 6.8 ms per frame, scale bar = 1 µm. D.G.B., C.B. (**C**) Results of diffusive analysis for the HaloTagged autophagy proteins under control and EBSS starvation. Top 3 panels present the diffusion coefficients of the tracks based on the SpotON analysis. Bottom panel depicts the percentage associated with each fraction. The box indicates confidence interval ± SD, the square indicates the average, and the horizontal line is the median; for each condition, 3 biological replicates were analyzed, ~20 cells/replicate. D.G.B., C.B.

As an orthogonal approach, we determined the relative abundance of HaloTagged proteins in our collection of cell lines using flow cytometry and converted the relative fluorescence into an absolute protein number using Halo-ATG9A C1 as a fiducial point.

The absolute protein abundance determined with flow cytometry and in-gel fluorescence were in good agreement, with some differences in the range of the technical error (**Fig. 2.2D**). Collectively, we have determined the absolute protein abundance of key autophagy factors and identified unexpected ratios between the subunits of the ULK1 complex. ULK1 and ATG2A were expressed at substantially lower levels than other autophagy proteins and this may contribute to key regulatory steps that control autophagic flux.

Single-molecule analysis of the subcellular dynamics of autophagy factors

The dynamic recruitment of autophagy proteins to the sites of autophagosome formation is critical to controlling overall autophagic flux. Autophagosome formation can initiate at cargo-dependent sites such as mitophagy (Dalle Pezze et al., 2021). Alternatively, under starvation conditions, autophagosomes non-specifically engulf cellular material (Lamb et al., 2013). In either case, it is not known how autophagy factors encounter sites of autophagosome formation. Potential mechanisms include 3D-diffusion or scanning of existing membrane structures. To define the subcellular distribution of autophagy proteins and the mechanism by which they are recruited to the sites of autophagosome formation, we performed single-molecule live-cell imaging and single-particle tracking (SPT) of the HaloTagged autophagy factors. Analysis of single-particle trajectories using the SpotOn tool allowed us to define distinct mobility states for each autophagy protein imaged (**Fig. 2.3A-B, Movie S1-9**).

In principle, autophagy proteins could exist in three different states: freely diffusing in the cytoplasm, scanning a membrane (through intrinsic phospholipid binding, binding to a protein with intrinsic phospholipid binding, or interacting with transmembrane proteins), or statically bound to a site of autophagosome formation. Lipid vesicles, including ATG9A-containing vesicles, are expected to have diffusion properties closer to membrane-interacting proteins (Rothman et al., 2016; Staufer et al., 2022). To approximate the diffusion parameters for each of these states, we analyzed a HaloTag protein fused to a nuclear export signal (Halo-NES, **Movie S10**), to model freely diffusing proteins, and SNAP-SEC61, as a model membrane-bound protein (**Movie S10**). The Halo-NES diffused rapidly (D_{free} = 15 $\mu m^2/s$, F_{free} = 99%) and had a negligible static fraction (F_{Static} = 1%) (**Fig. 2.3C**). SEC61 particles either slowly diffused (D_{slow} = 0.75 $\mu m^2/s$, F_{slow} = 65%), or were static (D_{static} = 0.08 $\mu m^2/s$, F_{static} = 35%) (**Fig. 2.3C**), which likely represents SEC61 molecules moving freely within the ER membrane or SEC61 molecules that are part of a translocon actively engaged with a ribosome in the process of translation, respectively.

To define the diffusion properties of autophagy proteins, cells were imaged under control (control) and starved (EBSS treated) conditions. Except for ATG9A, we used the 3-state model described above (freely diffusing, membrane scanning, statically bound to an autophagosome or other membrane) to fit the step size distributions of all autophagy proteins (Fig. 3B). Since ATG9A, like SEC61, is a transmembrane protein and resides in lipid vesicles, it does not freely diffuse through the cytoplasm. Diffusion of lipid vesicles within the cytoplasm is characterized by smaller diffusion coefficients than cytosolic proteins (Yamamoto et al., 2012). Lipid vesicles interacting with membrane organelles (i.e., autophagosomes interacting with the ER) are expected to be statically bound. Therefore, a 2-state model better describes the expected diffusion properties of ATG9A vesicles and was used to fit the step size distribution of ATG9A trajectories. The step-size distribution for all autophagy factors fits well with a 3-state model (or 2-state model in the case of ATG9A, Fig. 3A). For all other autophagy factors analyzed, a large fraction of the particles was freely diffusing (Dfree = 4-6 µm2/s, Ffree = 46-85%) (**Fig. 2.3C**). In addition, a significant fraction of molecules for all proteins analyzed moved with a diffusion coefficient comparable to SEC61 (Dslow = 0.5-0.75 µm2/s, Fslow = 12-35%) (**Fig. 2.3C**), consistent with these particles representing a membrane-associated population of the autophagy factors. Finally, a small fraction of molecules of all factors imaged were static (Dstatic = 0.02-0.08 µm2/s, Fstatic = 4-22%) (**Fig. 2.3C**). Approximately half of the ATG9A molecules diffused slowly (Dslow = 0.3 µm2/s, Fslow = 50%), while the other half of ATG9A particles were static (Dstatic = 0.02 µm2/s, Fstatic = 50%) (**Fig. 2.3C**). The diffusion properties of ATG5 and ATG16 were comparable, consistent with ATG5 and ATG16 forming a constitutive complex (Fig. 3C). Interestingly, the diffusion properties of ATG13 and ULK1 were distinct (**Fig. 2.3C**). ATG13 had a higher fraction of freely diffusion molecules than ULK1 (76% vs 59%) and the diffusion coefficient for this fraction was significantly higher for ATG13 compared to ULK1 (4.7 µm2/s vs. 2.6 µm2/s, p<0.001) (**Fig. 2.3C**). Together, this suggests that a substantial fraction of ATG13 is not associated with ULK1, which is consistent with our observation that the abundance of ATG13 exceeds the amount of ULK1 by approximately 9-fold. Freely diffusing PI4KIIIβ particles displayed the slowest diffusion coefficient of all proteins analyzed, which could be the consequence of transient interactions formed with endosomes and other Golgi-derived organelles (Judith et al., 2019; Waugh, 2019). Finally, more than 50% of LC3 molecules were in the bound or static state. LC3 exists in two primary forms, a lipid-conjugated form (LC3-II) inserted into autophagic membranes and a cytosolic non-conjugated form (LC3-

I) (Kabeya et al., 2004). Strikingly, the diffusion dynamics of none of the autophagy factors studied significantly changed after exposing cells to starvation conditions (Fig. 3C). This demonstrates that the dynamic properties of none of the factors studied are globally changed by cell starvation. In addition, the observation that the static populations remain unchanged under starvation conditions shows that only a very small fraction of molecules of a given autophagy factor are actively involved in autophagosome formation. Taken together, our single-molecule analysis of the diffusion dynamics of the tagged autophagy factors suggests that all proteins analyzed exist in a freely diffusing and membrane-associated state. In addition, our data demonstrate that the diffusion properties of the tagged autophagy proteins do not globally change in starvation conditions, indicating that only a small fraction of these proteins actively participates in autophagosome formation.

Quantitative analysis of the autophagosome formation reveals two distinct populations of autophagosomes

We next sought to quantitatively analyze the recruitment of the tagged autophagy factors to autophagosomes, which was not possible using the single-molecule approach described above. The local accumulation of autophagy proteins at sites of autophagosome formation can be visualized as bright cytoplasmic foci and overall autophagic flux can be measured by determining the rate of foci formation using time-lapse microscopy (Dalle Pezze et al., 2021; Itakura and Mizushima, 2010). Autophagy protein foci were automatically identified and tracked using single particle tracking (**Fig. 2.4A,B; Movie S11-18**) (Kuhn et al., 2021). Under control conditions, ULK1, ATG13, ATG5, and ATG16 formed significantly more foci (~30-50 foci per cell per hour), compared to ATG2A and WIPI2, which formed a limited number of foci in control cells (~9 foci per cell per hour, **Fig. 2.4C-D**). Nutrient starvation significantly increased the number of foci formed by all autophagy factors imaged (**Fig. 2.4C-D**). Interestingly, the number of foci formed per cell per hour under starvation conditions was comparable (~120-150) for ATG5, ATG13, ATG16, and ULK1, which was approximately 2-fold higher than the number of foci formed by ATG2A (~60 foci per cell per hour) (**Fig. 2.4C-D**). WIPI2 formed an intermediate number of foci (~90 foci per cell per hour) (**Fig. 2.4C-D**). This suggests that ATG2A is only detectably recruited to a subset of phagophores.

To further analyze the characteristics of the phagophores detected, we determined the diffusion coefficient of cytoplasmic foci formed by the tagged autophagy factors, which reports on the mobility of the autophagosomes they associate with. The diffusion coefficient distribution of ATG2A positive autophagosomes revealed a single population with a mean diffusion coefficient of $D = 0.002\ \mu m^2/s$ (**Fig. 2.4E**). In contrast, the diffusion coefficient distributions of all other autophagy factors analyzed were clearly made up of two distinct populations, one with a diffusion coefficient comparable to ATG2A positive autophagosomes, and a second population of foci that moved more rapidly ($D = 0.01\ \mu m^2/s$) (**Fig. 2.4E**). Importantly, the number of foci formed by ATG5, ATG13, ATG16, ULK1, and WIPI2 (e.g. $F_{slow,ATG5} = 0.64 * 120$ foci per cell per hour = 76 foci per cell per hour) that had a comparable diffusion coefficient to ATG2A foci is in a similar range as the number of ATG2 foci formed (~60 per cell per hour) (**Fig. 2.4F**).

Our observations demonstrate that ATG2 positive foci are less mobile than a large fraction of the foci formed by other autophagy proteins analyzed. This reduced mobility could be a consequence of ATG2A-mediated tethering of the phagophore to the

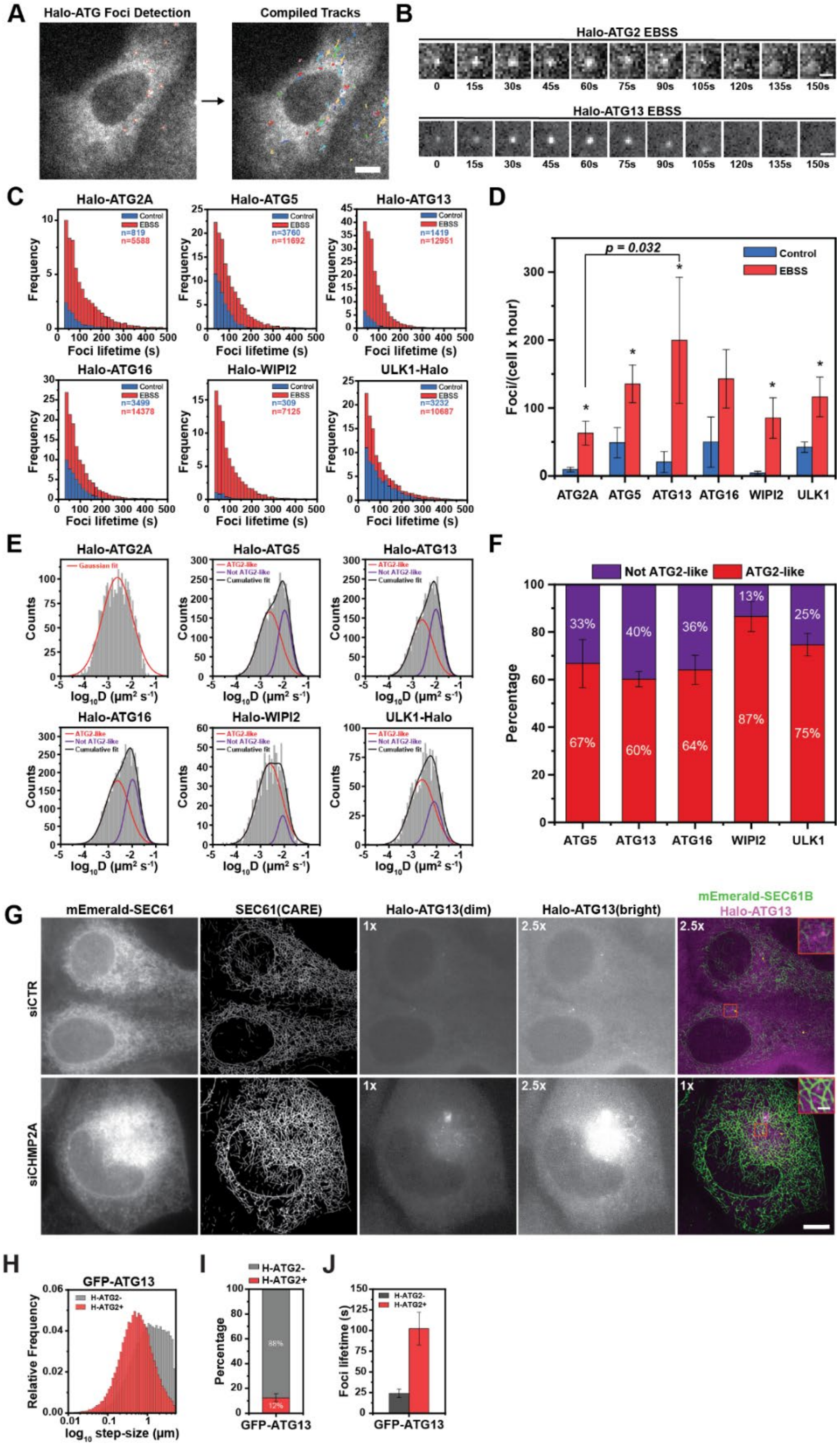

Figure 2.4. High-throughput quantification of autophagy factor foci lifetime and diffusion dynamics. (**A**) Upon labeling with fluorescent dye (JF646), cells expressing HaloTagged autophagy factors were starved (EBSS) and imaged at 4 frames per minute

Figure 2.4. (cont'd) for 1h. TrackIT was used to detect foci based on threshold intensity (left) and connected into tracks using the nearest neighbor algorithm (right). D.G.B., C.B. (**B**) Example images of foci for Halo-ATG2A (upper panel) and Halo-ATG13 (bottom panel). Scale bar = 5 µm. D.G.B., C.B. (**C**) Histograms of foci lifetime for the HaloTagged autophagy proteins in control conditions (Control) and after 1h nutrient starvation (EBSS). Three biological replicates (20-30 cells per replicate) were performed for each HaloTag cell line. The number of data points (n) is indicated in each graph in the figure panels. D.G.B., C.B. (**D**) Quantification of the number of foci formed per cell by autophagy factors over the course of 1h imaging in control (Control) and nutrient starvation (EBSS) conditions (N = 3 biological replicates, mean ± SD). A two-tailed *t*-test was used for statistical analysis (*p<0.05). D.G.B., C.B. (**E**) Histograms of diffusion coefficients of the foci formed by autophagy factors under nutrient starvation. Histograms were fitted with Gaussian curves. For the proteins other than Halo-ATG2A, we fixed the mean of one subpopulation (in red) to match Halo-ATG2A mean. An additional subpopulation (in purple) represents non ATG2A-like foci. The black line represents the cumulative fitting. C.B. (**F**) Distribution of ATG2A-like and non ATG2A-like foci diffusion coefficients (N = 3 biological replicates, mean ± SD). C.B. (**G**) Co-localization of ATG13 foci with the endoplasmic reticulum (ER) in control conditions (siCTR) or CHMP2A knock-down (siCHMP2A) cells. The ER was marked with mEmerald-SEC61 and high-resolution images were generated using the content aware image reconstruction (CARE) algorithm. Halo-ATG13 foci were scaled at low (1X) and high (2.5X) brightness. D.B. (**H**) Histogram of step-size distribution of Halo-ATG2A-positive (H-ATG2A+, red) and Halo-ATG2A-negative (H-ATG2A-, grey) GFP-ATG13 foci. Three biological replicates (20-30 cells per replicate) were performed for each experiment. D.G.B., C.B. (**I**) Fraction of GFP-ATG13 foci showing accumulation of Halo-ATG2A (N = 3 biological replicates, mean ± SD). D.G.B., C.B. (**J**) GFP-ATG13 foci lifetime for Halo-ATG2A+ and Halo-ATG2A-populations (N = 3 biological replicates, mean ± SD). D.G.B., C.B.

ER. To dissect the role of ATG2A in tethering autophagosomes to a lipid source, we analyzed the movement dynamics of stalled phagophores by knocking down the autophagosome termination factor CHMP2A in the Halo-ATG13 cell line (Takahashi et al., 2018) (**Appendix Fig. 13A**). Since CHMP2A is required for autophagosome closure(Takahashi et al., 2018), these stalled autophagosomes presumable have undergone expansion by ATG2A-mediated lipid transfer. Depletion of CHMP2A resulted in the accumulation of Halo-ATG13 foci co-localized with the ER, and we observed coordinated movements of ER tubules and Halo-ATG13 foci, indicating that the Halo-ATG13 foci are tethered to the ER (**Fig. 2.4G**, **Movie S19**). We also observed Halo-ATG13 foci that co-localized with the ER in control cells (**Fig. 2.4G, Movie S19**).

To directly test whether ATG2A is responsible for tethering autophagosomes we performed dual-color particle tracking of Halo-ATG2A and transiently expressed GFP-ATG12. Only a small fraction (12%) of Halo-2A foci co-localized with GFP-ATG13 foci and the mobility of GFP-ATG13 foci that co-localized with Halo-ATG2A was substantially lower than GFP-ATG13 foci that lacked Halo-ATG2A signal (**Fig. 2.4H-J, Movie S20**).

Strikingly, the lifetime GFP-ATG13 foci that co-localized with Halo-ATG2A (100 s) was significantly longer than GFP-ATG13 that did not accumulate Halo-ATG2A (25 s) (**Fig. 2.4L, Movie S20**), suggesting that foci that recruit both ATG13 and ATG2A likely represent stable phagophores undergoing expansion by lipid transfer and therefore are tether to a lipid donor compartment.

Together these observations demonstrate that ATG5, ATG13, ATG16, and ULK1 are recruited to all phagophores while ATG2A only detectably accumulates at a subset of autophagy-induced foci. In addition, our analysis of the movement dynamics of foci formed by the tagged autophagy factors suggests that ATG2A recruitment triggers the transition of the phagophore to a less mobile state, potentially by forming an anchor point to lipid donor membranes.

Both classes of phagophores identified from tracked populations require ULK1 complex and PI3K activity

The data presented thus far demonstrate that our automated particle tracking approach can quantitatively determine the frequency of formation and biophysical properties of starvation-induced autophagy protein foci. To validate that the tracked foci represent bona fide phagophores that mature into autophagosomes, we dissected the genetic requirements for their initiation by analyzing the contribution of the ULK1 complex and

PI3K to foci formation. It is well-established that ULK1 is critical for the initiation of autophagy (Karanasios et al., 2016; Mercer et al., 2009; Mizushima, 2010; Szymańska et al., 2015). As a marker for the ULK1 complex, we used Halo-ATG12. Our analysis of Halo-ATG13 foci dynamics revealed two distinct classes of ATG13 positive structures: a static population with a diffusion coefficient comparable to ATG2A positive foci, and a second population with higher mobility. We hypothesize that these classes of ATG13 foci represent untethered pre-phagophores (higher mobility), and phagophores tethered to a donor membrane by ATG2A (lower mobility). We therefore expected that the formation of both populations of ATG13 foci would require signaling through the ULK1 and PI3K complexes. To dissect the contribution of the ULK1 complex to the formation of both classes of autophagosomes, we knocked out ULK1, FIP200, or ATG101 in the Halo-ATG13 cell line (**Fig. 2.5A**). Clonal knock-out cell lines of ULK1, FIP200, or ATG101 showed a significant defect in LC3 conjugation under starvation conditions and a shifted phospho-P62 band was detected by western blot in the FIP200 and ATG101 knock-out cells (**Fig. 2.5B**). Interestingly, LC3 conjugation was more strongly inhibited in FIP200 and ATG101 knock-out cells compared to cells lacking ULK1 (**Fig. 2.5B,C**). ULK2 may compensate for the loss of ULK1 activity under these circumstances. We were unable to generate ULK1 and ULK2 double knock-out cells, indicating that loss of ULK1 and ULK2 function may be lethal in U2OS cells.

As an alternative approach, we combined the ULK1, FIP200, and ATG101 gene knockouts with ULK-101, a highly potent and specific small molecule inhibitor of both

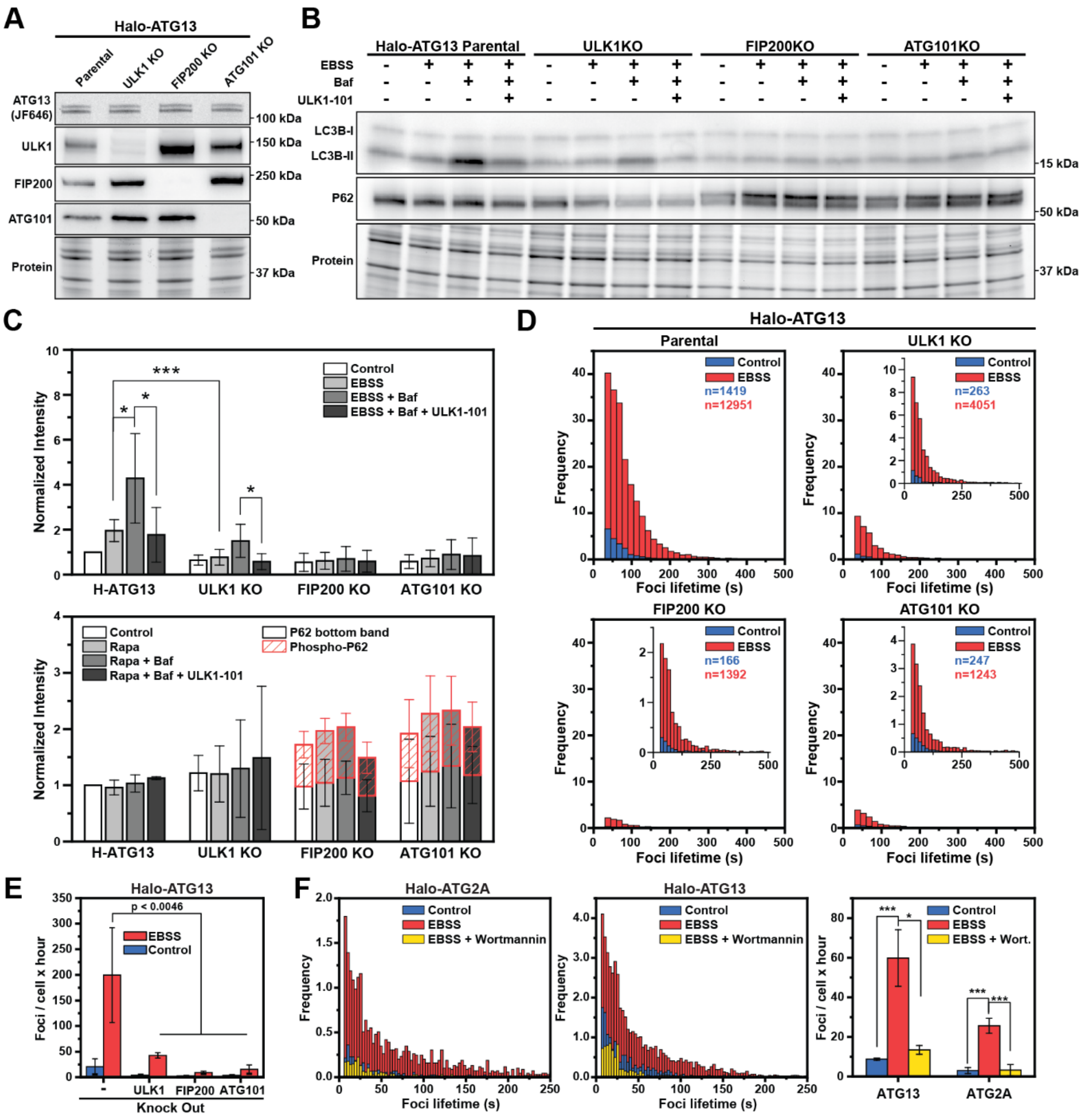

Figure 2.5. All tracked populations of autophagy factors foci require ULK1 and PI3K activity. (**A**) Fluorescence gel and western blots demonstrating successful knock-out of ULK1, FIP200 and ATG101 from the Halo-ATG13 cell line. D.G.B., C.B. (**B**) Western blots demonstrating impaired autophagy when ULK1, FIP200 and ATG101 are individually depleted from the Halo-ATG13 cell line. For the treatment experiments, cells were preincubated in control media with ULK1-101 (1µM) or without drug for 1 hour where indicated. Cells were then switched to their control or EBSS starvation media, with or without bafilomycin (100nM), for an additional hour. D.G.B., C.B. (**C**) Quantification of the western blots in (B). Data represent mean ± SD over three biological replicates. Phospho-P62 band (red striped bar graph) was detected and quantified only in the FIP200 and ATG101 knock-out cell lines. D.G.B., C.B. (**D**) Histograms of Halo-ATG13 foci lifetimes for the parental Halo- ATG13 cells and ULK1, FIP200, ATG101 knock-out cell lines in

Figure 2.5. (cont'd) control conditions (Control) and after 1h nutrient starvation (EBSS). Three biological replicates (20-30 cells per replicate) were performed for each cell line. The number of data points (n) is indicated in each graph in the figure panels. D.G.B., C.B. (**E**) Quantification of the number of foci formed per cell by HaloTag-ATG13 over the course of 1h imaging in control (Control) and nutrient starvation (EBSS) conditions (N = 3, mean ± SD). A two-tailed *t*-test was used for statistical analysis. D.G.B., C.B. (**F**) Histograms of foci lifetimes for the HaloTag-ATG2A (left) and HaloTag-ATG13 (center) in control and nutrient starvation (EBSS, 1h) conditions with and without wortmannin (1µM). Cells were pretreated with wortmannin for 1 hour. Right panel presents the quantification of the foci frequency. Data represent mean ± SD over three biological replicates (20-30 cells per replicate). A two-tailed *t*-test was used for statistical analysis (*$p < 0.05$, **$p < 0.01$, ***$p < 0.001$). Frequency histogram of foci lifetime for the Halo-ATG2AA (left) and Halo-ATG13 (right) imaged at 3 s framerate over 12 min imaging. Cells were imaged under control (Control), nutrient starvation (EBSS), and starvation + wortmannin (EBSS+wortmannin). D.G.B., C.B.

ULK1 and ULK2 (Martin et al., 2018). ULK-101 treatment in ULK1 knock-out cells further decreased LC3 conjugation, to the levels observed in cells lacking FIP200 or ATG101, confirming the previously reported role for ULK2 in maintaining LC3 conjugation in the absence of ULK1 (**Fig. 2.5B,C**) (Ro et al., 2013). In addition, these observations demonstrate that the knock-out of ATG101 and FIP200 leads to a complete loss of ULK1 complex function, which is consistent with previous studies (Itakura and Mizushima, 2010; Kannangara et al., 2021). To determine which step of autophagosome formation is inhibited by the loss of function of ULK1, FIP200, and ATG101, we assessed the formation of ATG13 foci in the knock-out cell lines in both control and starved conditions (**Fig. 2.5D**). As expected, under control conditions Halo-ATG13 formed a small number of foci in all cell lines (**Fig. 2.5E, Movie S21**). After treatment with EBSS, Halo-ATG13 foci formation was increased to ~200 foci/cell/hour in the parental cells (**Fig. 2.5E**). Knock-out of FIP200 and ATG101 resulted in a significant reduction in the number of Halo-ATG13 foci formed, from ~200 to ~9 and ~15 foci/cell/hour, respectively (**Fig. 2.5E, Movie S21**). In ULK1 knock-out cells Halo-ATG13 formed ~50 foci/cell/hour (**Fig. 2.5E**), consistent with the intermediate phenotype observed for LC3 conjugation (**Fig. 2.5B-C**).

Together these observations suggest that the tracked foci represent bona fide phagophores or autophagosomes and that their formation is dependent on the assembly of the ULK1 complex.

A critical consequence of ULK1 activation is thought to be the localized generation of PI3P by VPS34 at the site of autophagosome formation. To determine if PI3P accumulation is downstream of ULK1 complex enrichment at the phagophore, we treated Halo-ATG13 cells with 1 µM Wortmannin, which broadly inhibits the PI3-kinase activity, for 1 hour prior to and during cell starvation with EBSS and analyzed foci formation by Halo-ATG12. Strikingly, inhibition of PI3P-kinase activity eliminated the induction of Halo-ATG13 foci under starvation conditions (**Fig. 2.5F, Movie S22**). Experiments performed with Compound 31 (Pasquier et al., 2015), a specific VPS34 inhibitor, showed a similar reduction of Halo-ATG13 foci (**Appendix Fig 13B**). This suggests that PI3P formation by VPS34 is critical for ATG13 accumulation at the phagophore and phagophore initiation. To confirm this finding, we treated Halo-ATG2A cells with wortmannin and analyzed its impact on ATG2A foci formation. Similar to Halo-ATG13, the number of Halo-ATG2A foci formed in starved cells was reduced to those observed under control conditions by treatment with wortmannin (**Fig. 2.5F, Movie S23**). Importantly, this experiment confirmed that the number of Halo-ATG2A foci formed is approximately half of the number of Halo-ATG13 foci formed in all experimental conditions (**Fig. 2.5F**). Since these experiments were carried out at a higher time resolution compared to the experiments shown in Figure 4, we also confirmed that the diffusion coefficient distribution of ATG13 foci contained two distinct populations, while that of ATG2A only had a single slowly diffusing population (**Appendix Fig. 13B**). These observations demonstrate that both populations of ATG13 foci require PI3P formation by VPS34 and ULK1 complex activity and suggest that the two populations of autophagosomes with distinct mobilities represent different stages of autophagosome formation. We will refer to the mobile population as “pre-phagophores” and the static population as “phagophores”.

It was previously proposed that a positive feedback loop initiated by ULK1 activation and reinforced by additional ULK1 complex recruitment via the formation of PI3P by VPS34 at the phagophore is the critical trigger for autophagosome formation (Ganley et al., 2009; Hosokawa et al., 2009; Jung et al., 2009; Karanasios et al., 2013a; Mercer et al., 2009; Russell et al., 2013). Importantly, ATG13 contains a PI3P/PI4P binding sequence in its N-terminus, which is thought to contribute to the association of the ULK1 complex with the pre-phagophore (Karanasios et al., 2013a). To analyze the dynamic association of ATG13 with cytoplasmic membranes we took advantage of the live-cell single-molecule imaging approach we developed. Our observations demonstrated that a fraction of Halo-ATG13 particles were highly static and a second subset of Halo-ATG13 molecules moved with a similar diffusion coefficient as SNAP-SEC61. We propose that these slow-moving and static Halo-ATG13 particles are the consequence of the association of Halo-ATG13 with cytoplasmic membrane compartments or phagophores. We first determined whether the diffusion properties of Halo-ATG13 were impacted by the knock-out of ULK1, FIP200, or ATG101. Halo-ATG13 diffusion properties were unchanged in cells lacking ULK1, FIP200, or ATG101 under both control and starved conditions (**Appendix Fig. 13D, Movie S24**). These observations suggest that the membrane association of ATG13 does not depend on its association with any of the other ULK1 complex components. Our results demonstrate that the initiation of autophagosome formation requires the ULK1 complex. In addition, ULK1 complex accumulation at the phagophore requires PI3P, which is potentially mediated by the association of ATG13 with PI3P. Altogether, our observations are consistent with a model in which a positive feedback loop initiated by the ULK1 complex and amplified by VPS34 is critical to trigger autophagosome formation.

The majority of cytoplasmic foci formed by autophagy proteins do not progress to form mature autophagosomes

The experiments described thus far focused on the initiation of starvation-induced foci by the tagged autophagy proteins. To analyze the progression of these foci into mature autophagosomes, we performed quantitative dual-color live-cell imaging to assess the recruitment of the cargo adaptor P62 and the ATG8 family protein LC3 to the starvation-induced foci formed by the tagged autophagy factors. To mark growing phagophores and mature autophagosomes we transduced cells with baculoviruses encoding GFP-LC3 or GFP-P62. To avoid GFP-LC3 aggregation, we optimized the virus concentration using GFP-LC3-G120A, which cannot be conjugated and therefore only forms foci by aggregation. At the viral titers used no GFP-LC3-G120A foci were detected in the Halo-ATG9A cell line, but GFP-LC3-G120A aggregates were observed in ATG9A knock-out cells, which is consistent with the previously observed LC3 aggregates reported in autophagy-deficient cells (**Fig. 13E**) (Runwal et al., 2019). Using this protocol, cells expressing the HaloTagged autophagy proteins were transduced with GFP-LC3 or GFP-P62 and imaged with high time resolution (3 s per frame) after cell starvation with EBSS (**Fig. 2.6A, Movie S25-35**). GFP and HaloTag signals were tracked independently, and

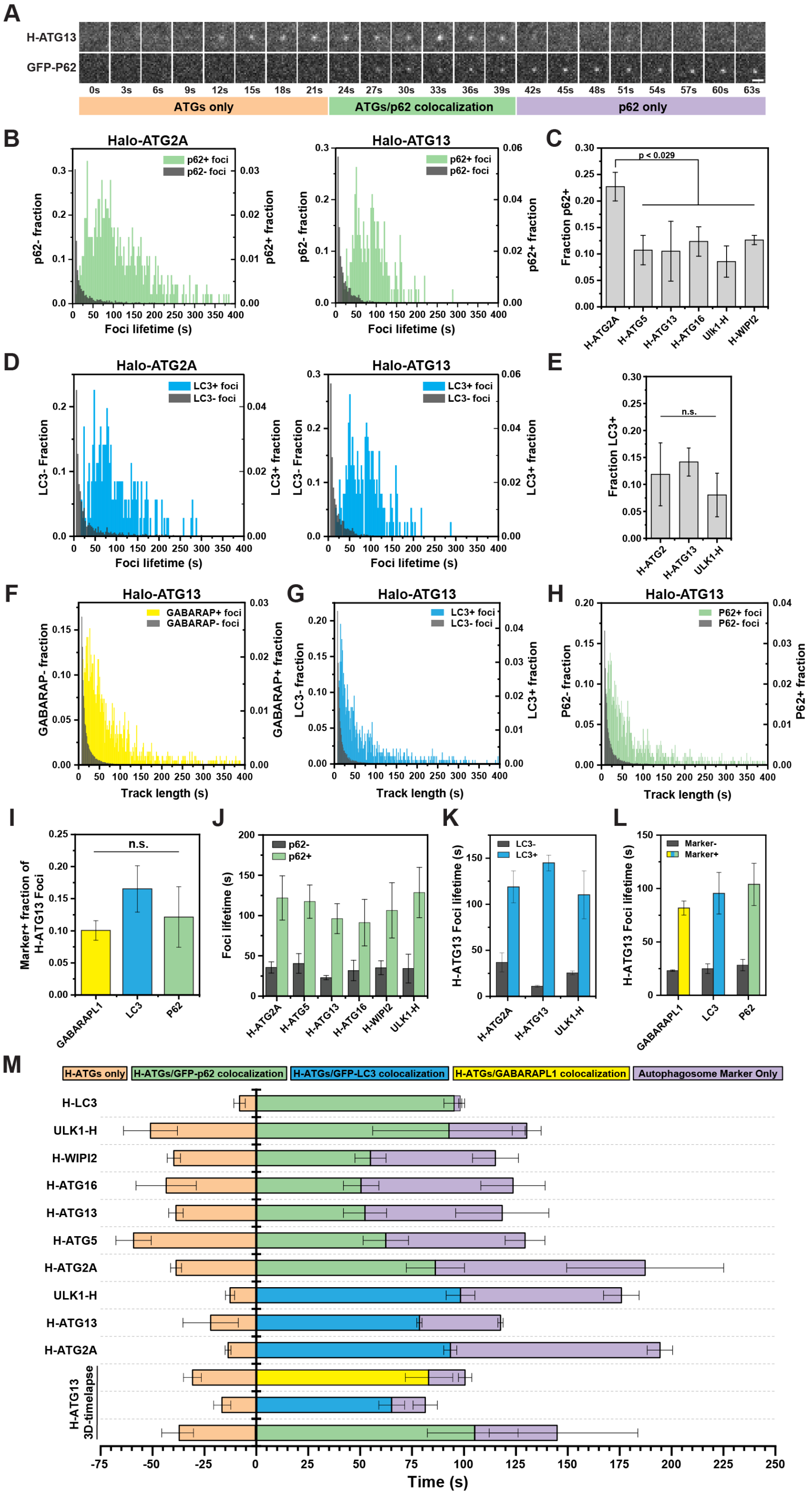

Figure 2.6. Analysis of the maturation kinetics of autophagosomes using dual-color imaging. (**A**) Example images showing formation, growth, and disappearance of co-localized Halo-ATG13 and GFP-p62 foci using dual-color live-cell imaging under EBSS starvation (1h). Scale bar = 2 μm. D.G.B., C.B. (**B**) Histograms of the lifetimes of Halo-

Figure 2.6. (cont'd) ATG2A and Halo-ATG13 foci that colocalized (green) or did not colocalize (dark grey) with virally transduced GFP-P62. D.G.B., C.B. (**C**) Percentage of HaloTagged autophagy protein foci that co-localized with P62 foci. Data represents mean ± SD of three biological replicates (20-30 cells per replicate). A two-tailed *t*-test was used for statistical analysis. D.G.B., C.B. (**D**) Histograms of the lifetimes of Halo-ATG2A and Halo-ATG13 foci that colocalized (light blue) or did not colocalize (dark grey) with virally transduced GFP-LC2. D.G.B., C.B. (**E**) Percentage of HaloTagged autophagy protein foci that co-localized with LC3 foci. Data represents mean ± SD of three biological replicates (20-30 cells per replicate). A two-tailed *t*-test was used for statistical analysis. D.G.B., C.B. (**F-H**) Histograms of the lifetimes of Halo-ATG13 foci that colocalized or did not colocalize (dark grey) with (**F**) GFP-GABARAPL1 (yellow), (**G**) GFP-LC3 (light blue), (**H**) GFP-p62 (green) stably expressed from an AAVS1 locus insertion. D.G.B., C.B. (**I**) Percentage of HaloTagged autophagy protein foci that co-localized with the adaptors GFP-GABARAPL1, GFP-LC3, and GFP-P62 stably expressed from an AAVS1 locus insertion. Data represents mean ± SD of three biological replicates (20-30 cells per replicate). A two-tailed *t*-test was used for statistical analysis. D.G.B., C.B. (**J**) Quantification of the average HaloTagged autophagy protein foci lifetimes for GFP-P62 positive (red) and negative (dark grey) foci. Data represents mean ± SD of three biological replicates (20-30 cells per replicate). D.G.B., C.B. (**K**) Quantification of the average HaloTagged autophagy protein foci lifetimes for GFP-LC3 positive (light blue) and negative (dark grey) foci. Data represents mean ± SD of three biological replicates (20-30 cells per replicate). D.G.B., C.B. (**L**) Quantification of the average Halo-ATG13 foci lifetimes that are negative (dark grey) or positive for adaptor signals (GABARAPL1, yellow; LC3, light blue; P62, green). Data represents mean ± SD of three biological replicates (20-30 cells per replicate). D.G.B., C.B. (**M**) Quantification of the timing of the three distinct phases of autophagosome formation for the HaloTag proteins under EBSS starvation (1h). Data represents mean ± SD of three biological replicates (20-30 cells per replicate). D.G.B., C.B.

co-localization was defined as particles whose centroids were less than 3 pixels apart at any given timepoint (see methods for details). This approach allowed us to analyze hundreds of autophagosomes in a completely unbiased fashion. A fraction (~10-20%) of the foci formed by all autophagy factors analyzed co-localized with P62 or LC3 ($\text{P62}^{\text{positive}}$, $\text{LC3}^{\text{positive}}$), but the majority (~80-90%) of foci never showed detectable P62 or LC3 accumulation ($\text{P62}^{\text{negative}}$, $\text{LC3}^{\text{negative}}$, **Fig. 2.6B-E, Appendix Fig. 13H-I**). The fraction of Halo-ATG2A foci that colocalized with P62 (23%) was approximately double that of all other autophagy proteins tested (10%) (**Fig. 2.6C**), while the fraction of autophagy protein foci that colocalized with LC3 was comparable for all proteins tested (**Fig. 2.6E**).

Importantly, the overall frequency and lifetime of P62 and LC3 foci was comparable across all cell lines, indicating that the HaloTagged autophagy proteins do not impact the formation of LC3- or P62-positive autophagosomes (**Appendix Fig. 13F-G**). It is possible that the lack of co-localization of the autophagy proteins analyzed with an autophagy marker was a consequence of the viral transduction, choice of autophagy cargo adaptor, or drift of the autophagy factor foci out of the focal plane of the objective. To rule out these possibilities, we stably expressed GFP-GABARAPL1, GFP-LC3B, and GFP-P62 by integrating a tetracycline-inducible expression cassette into the AAVS1 safe-harbor locus in our Halo-ATG13 cell line. Cells were grown in the absence of tetracyclin to limit the expression of the GFP-tagged P62, LC3B, and GABARAPL1. In addition, we increased the time resolution to 1.5 seconds per frame and imaged three z-sections, allowing us to analyze autophagy protein foci throughout the entire cytosol. The results did not differ from our previous findings: over 80% of ATG13 foci did not co-localize with GABARAPL1, LC3B, and P62 (**Fig. 2.6F-I**).

To gain further insight into the timeframe of autophagosome formation we analyzed the kinetics of foci formation and co-localization with P62 or LC2. The lifetime of the P62^{negative} autophagy protein trajectories (Mean = 23-41 s) was significantly ($p<0.001$) shorter than the P62^{positive} tracks (Mean = 91-122 s) for all tagged autophagy factors (**Fig. 2.6J**). Similarly, LC3^{positive} trajectories of Halo-ATG2A, Halo-ATG13, and Halo-ULK1 were significantly longer (Mean = 110-145 s) than LC3^{negative} tracks of the respective protein (Mean = 11-37 s) ($p<0.001$) (**Fig. 2.6K**), and GABARAPL1^{positive} Halo-ATG13 trajectories were significantly longer (Mean = 80 s) than Halo-ATG13 tracks that did not co-localize with GABARAPL1 (Mean = 25 s) (**Fig. 2.6L**). Viral expression and stable integration of GFP-LC3 and GFP-P62 lead to similar results (**Fig. 2.6J-L**). Altogether, these results demonstrate that most autophagosome initiation sites (~80-90%), marked by the local accumulation of an autophagy protein, rapidly disassemble ~25 s after their formation without detectably recruiting any of the cargo adaptors tested and therefor do not progress to form mature autophagosomes.

Kinetics of autophagosome formation

To dissect the assembly order and overall formation kinetics of autophagosomes we analyzed the sequential accumulation of the autophagy factors and P62 or LC3, respectively. To confirm the validity of this approach we first analyzed the accumulation of GFP-P62 at Halo-LC3 foci (**Fig. 2.6M, Movie S25**). As expected for LC3-dependent recruitment of P62 to phagophores, GFP-P62 and Halo-LC3 foci appeared nearly simultaneously (**Fig. 2.6M, Movie S25**). In addition, the GFP-P62 disappeared when Halo-LC3 foci were still detectable (**Fig. 2.6M**). We were unable to determine the fraction of Halo-LC3 marked autophagosomes that co-localized with GFP-P62, because Halo-LC3 does not get degraded after fusion of the autophagosome with the lysosome and therefore Halo-LC3 also leads to the accumulation of fluorescent signal in lysosomes. These properties of Halo-LC3 were recently described in detail by Yim and colleagues (Yim et al., 2022). We next analyzed the accumulation kinetics of GFP-LC3 and GFP-P62 at foci formed by the other HaloTagged autophagy factors. On average autophagy protein foci formed ~40-60 seconds prior to the recruitment of P62, co-colocalized with P62 for ~50-85 seconds, and dissociated from P62 foci ~30-100 seconds prior to the disappearance of the P62 signal, which is likely the consequence of autophagosome fusion with the lysosome and quenching of the GFP signal (**Fig. 2.6M, Movie S26-35**).

Compared to P62, LC3 accumulated at autophagy protein foci more rapidly (~12-22 seconds) after their formation (**Fig. 2.6M**), consistent with LC3 conjugation preceding P62 recruitment (Ichimura et al., 2008; Kirkin and Rogov, 2019; Noda et al., 2008; Pankiv et al., 2007). The total lifetime of autophagosomes (ATG signal appearance to P62 or LC3 signal disappearance) did not differ dramatically for all proteins tested (Range = 140-226 s, Mean = 175 s) (**Fig. 2.6M**). In total, these results demonstrate that if the phagophore matures into an autophagosome all autophagy factors analyzed are recruited in close succession ~40 seconds prior to the accumulation of P62, autophagosome biogenesis, from phagophore initiation to dissociation of the autophagy factors, takes ~110 seconds, and the total time from phagophore initiation to autophagosome fusion with the lysosomes is ~175 seconds.

ATG9A does not detectably accumulate at sites of autophagosome formation

A growing body of evidence suggests that ATG9-containing vesicles are the platform upon which the phagophore is assembled (Chang et al., 2021a; Chang et al., 2021b; Olivas et al., 2022; Sawa-Makarska et al., 2020). Live-cell imaging using a transiently expressed RFP-ATG9A suggested that ATG9A foci continuously interact with LC3B positive phagophores (Orsi et al., 2012). Furthermore, it has been proposed that autophagosomes are initiated at contact sites formed by the ER and ATG9A positive compartments (Karanasios et al., 2016). When performing dual color imaging to analyze the kinetics of Halo-ATG9A recruitment to the autophagosome we were unable to detect

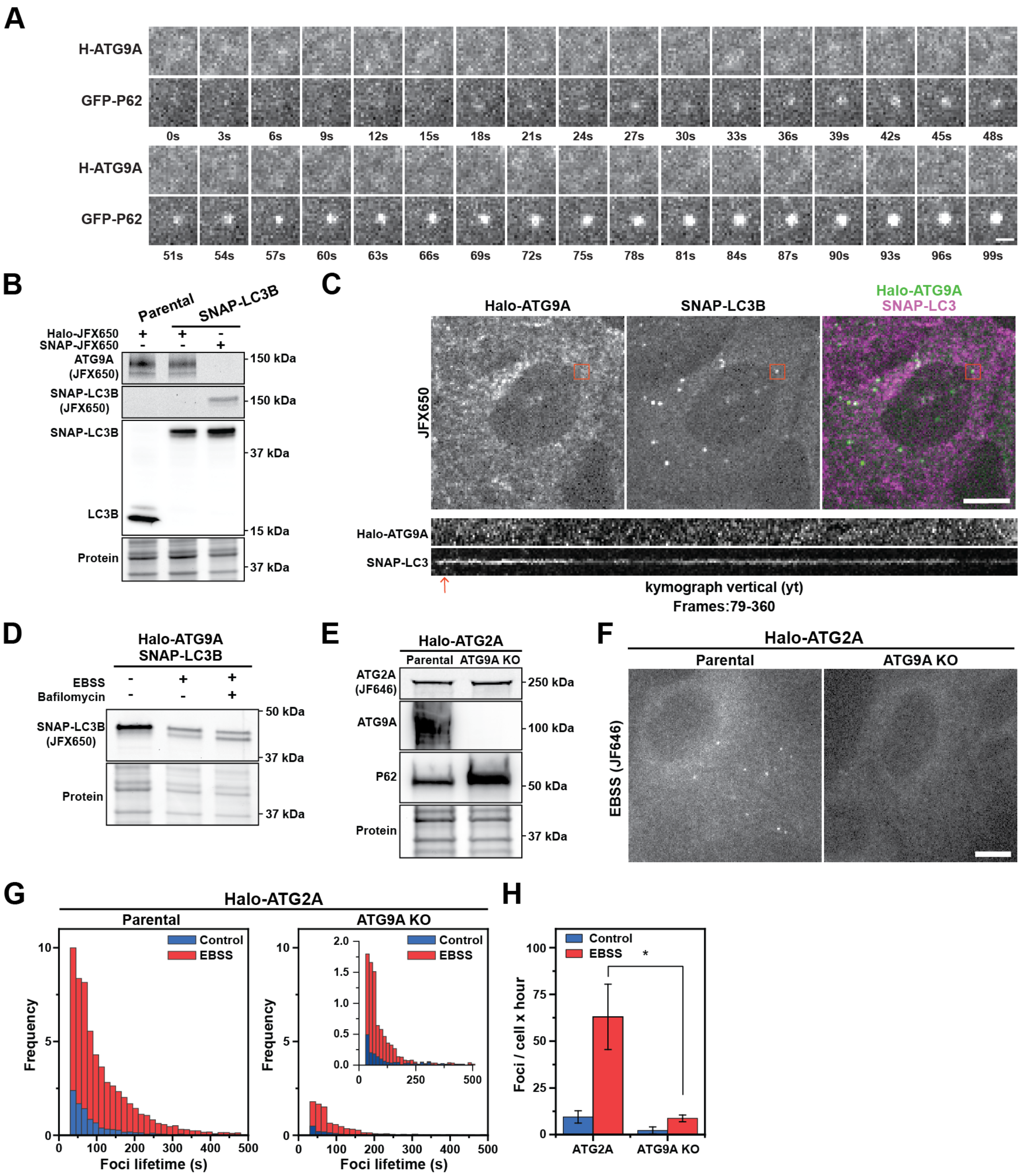

Figure 2.7. ATG9 does not detectably accumulate at the site of autophagosome formation. (**A**) Example image showing the formation of GFP-P62 spot in the absence of any Halo-ATG9A accumulation. D.G.B. (**B**) Fluorescent gels showing Halo-ATG9A (JFX650, top), and SNAP-LC3B (JFX650, middle) labeling, and western blot showing probed with an LC3 antibody showing the exclusive expression of SNAP-LC3B in genome edited cells. D.G.B., C.B. (**C**) Micrographs of cells expressing Halo-ATG9A (JFX650) and SNAP-LC3B (JF503) (top, scale bar = 10 µm) and kymograph of a SNAP-LC3B spot showing no accumulation of Halo-ATG9A (1 frame per second, frames 79-360). D.G.B. (**D**) Fluorescent gel of SNAP-LC3B (JFX650) after cell starvation and treatment with bafilomycin, demonstrating lipid conjugation of SNAP-LC3B (bottom band). D.G.B., C.B. (**E**) Fluorescence gel and western blots demonstrating successful ATG9A gene knock-

Figure 2.7. (cont'd) out from cells expressing Halo-ATG2A. The ATG9A knock-out cells accumulate P62, indicating impaired autophagy. D.G.B., C.B. (**F**) Micrographs showing decrease of Halo-ATG2A foci when ATG9A is knocked out (Scale bar = 10µm). Halo-ATG9A does not form foci detectable foci under EBSS starvation (right panel). D.G.B., C.B. (**G**) Histograms of Halo-ATG2A foci lifetime in parental and ATG9A knock-out cells (EBSS, 1h). D.G.B., C.B. (**H**) Quantification of the number of foci formed per cell over the course of an hour by Halo-ATG2A in control and ATG9A knock-out cells. Data represent mean ± SD of three biological replicates (20-30 cells per replicate). A two-tailed *t*-test was used for statistical analysis (**p*<0.05). D.G.B., C.B.

the accumulation of endogenous Halo-ATG9A at virally induced GFP-P62 positive foci (**Fig. 2.7A**). To confirm that Halo-ATG9A does not accumulate at sites of autophagosome formation, we edited the Halo-ATG9A cell line to express SNAP-LC3B from its endogenous locus (**Fig. 2.7B**). We confirmed the functionality of SNAP-LC3B, by starvation-induced foci formation and LC3 lipid conjugation using a fluorescence gel (**Fig. 2.7C-D, Movie S36**). Similar to GFP-P62 foci, we were unable to detect Halo-ATG9A accumulation at phagophores marked by SNAP-LC3B (**Fig. 2.7C, Movie S36**). These observations are at odds with the previous work mentioned above that detected co-localization of ATG9A positive sub-cellular structures and LC3 foci (Karanasios et al., 2016; Orsi et al., 2012). To verify the contribution of ATG9A to autophagosome formation in our U2OS cell system, we knocked out ATG9A in the Halo-ATG2A cell line (**Fig. 2.7E**). Compared to the parental Halo-ATG2A cells, we detected a molecular size shift of the P62 band in ATG9A knock-out cells (**Fig. 2.7E**), suggesting aberrant accumulation of P62, due to a defect in autophagy. We then analyzed the foci formation of Halo-ATG2A in the ATG9A knock-out cells. Under control and starvation conditions, the formation of ATG2A foci was significantly reduced in the absence of ATG9A (**Fig. 2.7G-H**, **Movie S37**). Therefore, while ATG9A accumulation is not detectable at autophagosome initiation sites it plays a critical role in the formation of ATG2A-positive phagophores. These

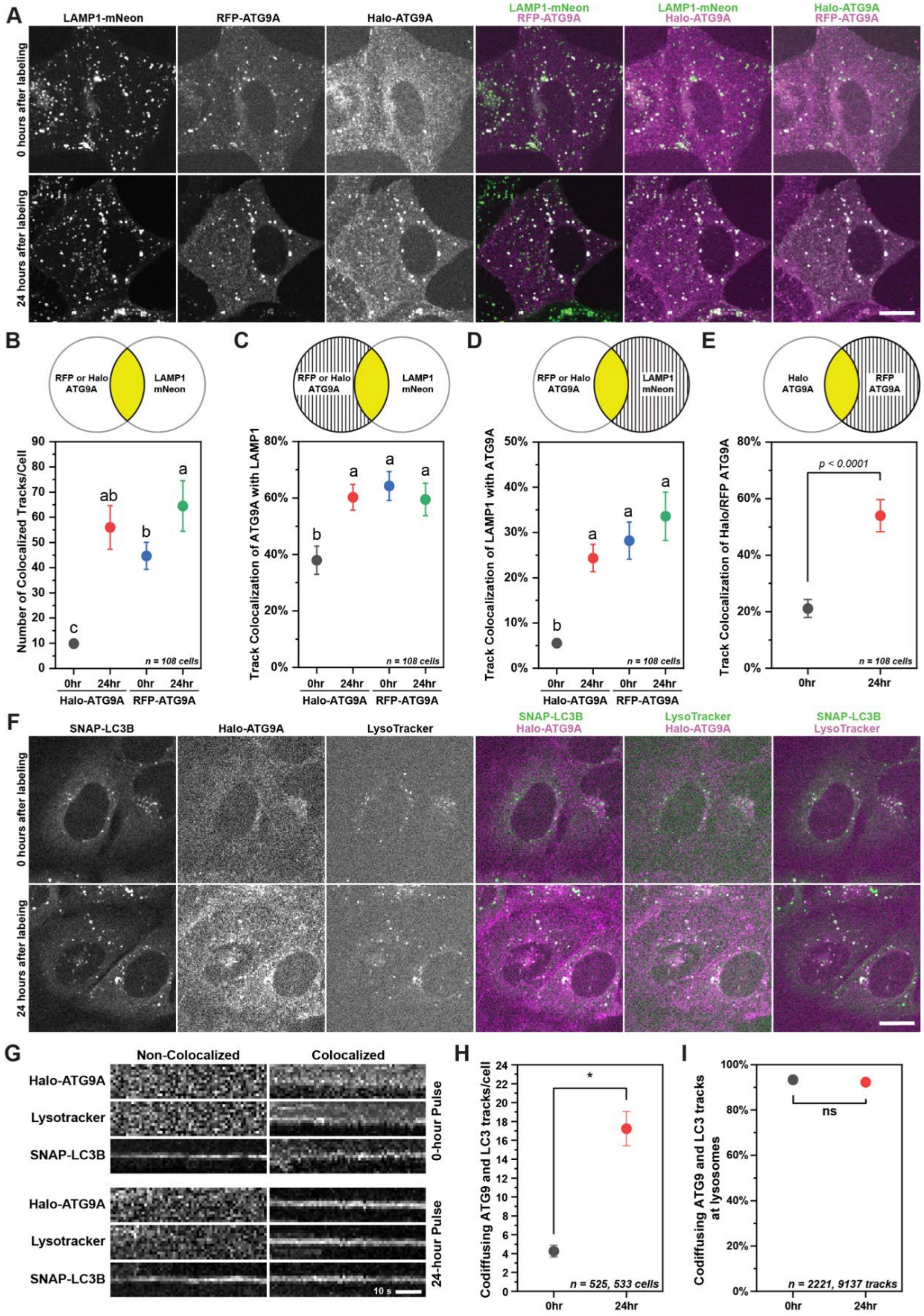

Figure 2.8. ATG9 compartments that co-localize with LC3 foci are lysosomes. (**A**) Micrographs showing cellular distribution of transiently expressed RFP-ATG9A, endogenous Halo-ATG9A, and lysosomes, marked with mNeon-LAMP1. Experiments

Figure 2.8. (cont'd) were performed immediately (upper panel) and 24 h (bottom panel) after labeling of Halo-ATG9A. D.G.B. (**B-E**) Quantification of Halo-ATG9A and RFP-ATG9A tracks colocalized with mNeon-LAMP1. The number of cells (n) is indicated in each graph in the figure panels. Top schemes depict which signals were used to calculate the fractions in the corresponding graph. The marker represent mean ± 95% confidence interval. Letters indicate statistically homogeneous group established by ANOVA ($p < 0.05$) followed by Bonferroni post-hoc test. D.G.B., C.B. (**F**) Micrographs showing cellular distribution of endogenous edited SNAP-LC3 and Halo-ATG9A, and lysosomes, marked with LysoTracker. Experiments were performed immediately (upper panel) and 24 hours (bottom panel) after Halo-ATG9A labeling. (Scale bar = 10 μm) D.G.B. (**G**) Kymographs showing co-localization of SNAP-LC3/Halo-ATG9A immediately and 24 hours after Halo-ATG9A labeling. D.G.B., C.B. (**H**) Number of co-diffusing Halo-ATG9A and SNAP-LC3 foci immediately and 24 hours after Halo-ATG9A labeling. The marker represent mean ± 95% confidence interval (*$p<0.05$). The number of data points (n) is indicated in each graph in the figure panels. D.G.B. (**I**) Fraction of colocalized SNAP-LC3 and Halo-ATG9 foci that also colocalized with lysosomes marked with LysoTracker. The marker represent mean ± 95% confidence interval. D.G.B.

observations are fully consistent with vesicles containing a small number of ATG9A molecules (undetectable by our imaging approach) forming the platform for autophagosome formation.

To resolve the discrepancy in the localization patterns of Halo-ATG9A and RFP-ATG9A, previously used by others (Karanasios et al., 2016; Orsi et al., 2012), we imaged Halo-ATG9A in cells transiently expressing RFP-ATG9A 48 hours after transfection. Surprisingly, minimal colocalization of Halo-ATG9A and RFP-ATG9A was observed immediately after labeling with JFX650, whereas RFP-ATG9A formed large structures that co-localized with LAMP1 (**Fig. 2.8A-E, Movie S38**). However, RFP-ATG9A, Halo-ATG9A, and LAMP1 all co-localized 24 hours after labeling the HaloTag with JFX650 (**Fig. 2.8A-E, Movie S38**). These observations demonstrate that RFP-ATG9A almost exclusively marks lysosomes. In contrast, the signal derived from Halo-ATG9A initially does not co-localize with lysosomes but accumulates in lysosomes 24 hours after HaloTag labeling. There are two possible explanations for this observation. First, at steady state, ATG9A is enriched in lysosomes and the HaloTag ligand fails to react with Halo-ATG9A in this acidic compartment. In this case, the HaloTag signal that accumulates would represent ATG9A molecules that were labeled elsewhere and trafficked to the lysosome over time. Alternatively, little ATG9A is found in lysosomes, and the fluorescent signal that accumulates over time results from the build-up of proteolysis-resistant fluorescent HaloTag molecules. Importantly, it was recently demonstrated that Halo-LC3 is partially degraded in lysosomes, causing labeled proteolysis-resistant HaloTag protein to accumulate within the lysosome (Yim et al., 2022). It is also well established that RFP fluorescent signal does not get quenched in lysosomes (Kaizuka et al., 2016; Yim et al., 2022). To analyze the trafficking of ATG9A and to determine whether the HaloTag fused to ATG9A is resistant to degradation we generated a cell line that expressed Halo-ATG9A under the control of a tetracyclin inducible promotor in an ATG9A knock-out background. This approach allowed us to control both Halo-ATG9A expression and fluorescent labeling. We induced Halo-ATG9A expression for 24 hours and imaged Halo-ATG9A immediately after labeling. Under these conditions Halo-ATG9A localized exclusively to the ER (**Appendix Fig. 14A-B**). In contrast, 24 hours after labeling (48 hours after expression induction) Halo-ATG9A localized to large foci resembling lysosomes (**Appendix Fig. 14B**). Continuous Halo-ATG9A expression lead to a similar result, although the enrichment of Halo-ATG9A on the ER immediately after labeling was less pronounced (**Appendix Fig. 14B**). Importantly, RFP-ATG9A also accumulated in the ER when imaged 24 hours after transfection (**Appendix Fig. 14D-E**). These observations demonstrate that when ATG9A expression is induced it is initially enriched in the ER before trafficking to other sub-cellular compartments.

To analyze Halo-ATG9A stability we induced Halo-ATG9A expression with a single doxycycline pulse or grew cells continuously in the presence of doxycycline and collected samples immediately, 24 hours, and 48 hours after Halo-ATG9A labeling. We detected a continual accumulation of fluorescently labeled HaloTag in cells stably over-expressing Halo-ATG9A (**Appendix Fig. 13C**), indicating that Halo-ATG9A, like Halo-LC3, is partially degraded over time releasing fluorescently labeled HaloTag protein. This result strongly suggests that ATG9A is degraded after it localizes to the lysosome and that the fluorescent signal derived from Halo-ATG9A that accumulates in lysosomes over time represents HaloTag protein resistant to proteolysis.

To dissect the relationship between ATG9A and LC3 positive compartments, and the lysosome, we simultaneously imaged Halo-ATG9A, SNAP-LC3B, and lysosomes marked with LysoTracker. Immediately after Halo-ATG9A labeling, we detected a limited number of SNAP-LC3 foci that co-localized with ATG9A positive compartments (**Fig. 2.8H, Movie S39**). In contrast, 24 hours after Halo-ATG9A labeling a large number of LC3 trajectories co-localized with Halo-ATG9A tracks (**Fig. 2.8H, Movie S39**). Finally, we determined that >90% of the ATG9A foci that co-diffuse with LC3 tracks are also marked by LysoTracker both immediately and 24 hours after Halo-ATG9A labeling (**Fig. 2.8C-F**). Together these results demonstrate that ATG9A is not detectably enriched at newly formed autophagosomes, and colocalization of ATG9A with LC3B exclusively occurs within the lysosome.

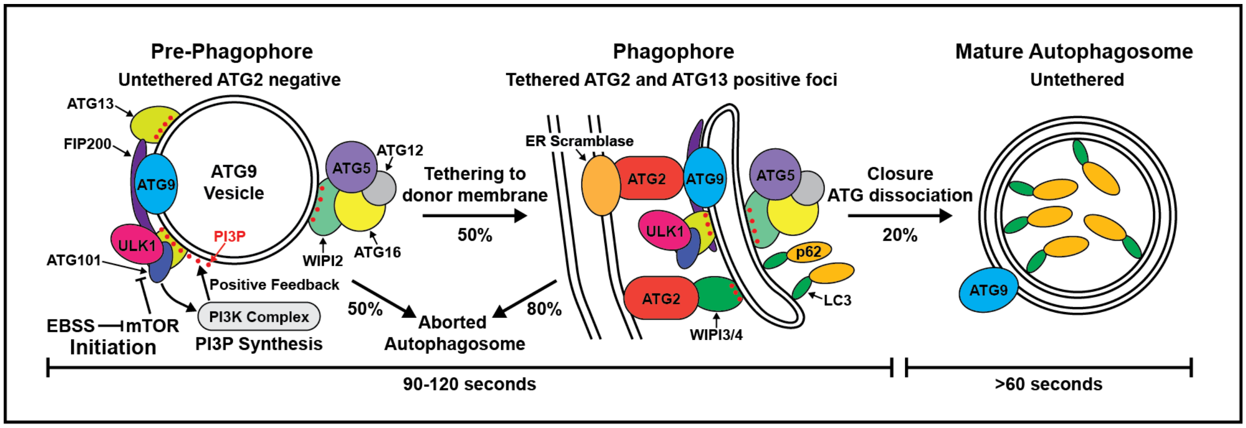

Figure 2.9. Model for the biogenesis of the autophagosome. Upon autophagy induction, a ULK1 complex - PI3-kinase feedback loop initiates the assembly of autophagy proteins on an untethered ATG9A vesicle. Approximately half of these pre-phagophores proceed to be tethered to cellular membranes via ATG2A. Only 20% of the ATG2A positive phagophores mature to a point where a the ATG8 family proteins (LC3, GABARAPL1) and the cargo adaptor P62 are detectably recruited, while the majority (80%) of autophagy protein foci disassemble without forming mature autophagosomes. The formation and growth of a full autophagosomes takes about 90-145 seconds. Upon closure, the autophagy proteins dissociate, the mature autophagosomes is untethered and is delivered to lysosomes (>60s). D.G.B., C.B., J.S.

Discussion

The experiments presented in this study systematically and quantitatively assess the formation of autophagosomes in human cells. Our work provides new mechanistic insights into the initiation and maturation of autophagosomes and the collection of cell lines we have created expressing HaloTagged autophagy factors from their endogenous loci represents a tremendously valuable tool for future studies of autophagosome formation in human cancer cells.

The role of ATG9 vesicles in autophagosome biogenesis

ATG9A/B are the only known transmembrane proteins that are critical for autophagosome formation (Guardia et al., 2020). ATG9A/B resides in lipid vesicles that traffic to and from the trans-Golgi network (TGN) and endosomes (Young et al., 2006). Upon starvation, the ULK1/2 complex controls the redistribution of ATG9A vesicles from the TGN to the phagophore site (Orsi et al., 2012). Several recent structural and biochemical studies have demonstrated that ATG9A forms a trimeric membrane pore that functions as a lipid scramblase, passively exchanging lipids between the inner and outer leaflets of lipid bilayers (Guardia et al., 2020; Matoba et al., 2020; Noda, 2021). These observations have led to a model in which ATG9A-containing vesicles constitute the platform upon which the autophagosome is formed via ATG2A-mediated lipid transfer from other membrane sources such as the endoplasmic reticulum (ER). Work by others has shown that ATG9A-containing proteo-liposomes or immunopurified ATG9A vesicles are sufficient for reconstituted nucleation of the autophagosome (Chang et al., 2021a; Chang et al., 2021b; Olivas et al., 2022; Sawa-Makarska et al., 2020). While these in vitro observations are consistent with the hypothesis that ATG9A vesicles are the platform for autophagosome formation, the evidence that ATG9A vesicles transform into autophagosomes in cells is limited.

The work presented here revealed that ATG9A is the only autophagy factor analyzed that does not detectably accumulate at sites of autophagosome biogenesis, yet it is essential for the formation of ATG2A-bound phagophores in U2OS cells. In addition, our results indicate that RFP-ATG9A and Halo-ATG9A accumulate in lysosomes. Therefore the previously reported association between forming autophagosomes marked by LC3 and ATG9A positive structures likely represents autophagosomes contacting lysosomes (Bright et al., 2005; Jahreiss et al., 2008). To assess ATG9A localization in the context of autophagosome formation in future experiments we believe it will be critical to include a lysosomal marker, to clearly distinguish lysosomes and autophagosomes. It is important to note that only a small fraction of lysosomes (~5%, **Fig. 2.8D**) co-localize with Halo-ATG9A, which is consistent with previous observations made using immunofluorescence to detect ATG9A and LAMP1 (Kannangara et al., 2021; Popovic and Dikic, 2014). The trafficking of ATG9A to the lysosome and the accumulation of cleaved, proteolysis-resistant HaloTag protein suggests that ATG9A can be degraded after autophagosomes fuse with the lysosome. Importantly, the lack of accumulation of ATG9A at sites of autophagosome formation is consistent with a lipid vesicle containing a small number of ATG9A molecules (not detectable by conventional fluorescence microscopy) forming the platform for phagophore initiation (**Fig. 2.7F**).

ATG2 recruitment leads to phagophore immobilization

Once an ATG9A vesicle has been specified as a seed for autophagosome formation it has to expand, engulf cargo, and eventually close into a mature autophagosome. ATG2A, a proposed direct interactor of ATG9A (Gómez-Sánchez et al., 2018; Tang et al., 2019), forms robust foci at autophagosomes, potentially by WIPI3/4-mediated recruitment of ATG2A to the phagophore (Chowdhury et al., 2018; Otomo et al., 2018; Ren et al., 2020). ATG2A is an extended barrel-shaped protein that can form tethers between lipid vesicles and transfer phospholipids between them (Chowdhury et al., 2018; Noda, 2021; Tang et al., 2019; Valverde et al., 2019). Therefore, it is thought that ATG2A is the critical factor for transferring phospho-lipids from a donor lipid source to the growing phagophore.

Our imaging methodologies allowed us to quantitatively analyze the recruitment of ATG2A to the phagophore. Strikingly, the number of ATG2A foci formed was approximately half of the number formed by all other autophagy factors tested except for WIPI2. In addition, the diffusion coefficient distribution of ATG2A showed a single slowly moving population, while all other factors contained two populations, one which was comparable to ATG2A positive foci and a second more rapidly diffusing population. Importantly, the number of slowly diffusing autophagy factor foci was similar to the number of ATG2A foci observed, suggesting that they reflect the same population of phagophores. These observations demonstrate that ATG2A marks a subset of phagophores with distinct biophysical properties. Consistent with this model, the recruitment of ATG2A to foci formed by the autophagosome initiation factor ATG13 leads to a reduction in the diffusion rate of these structures. We propose that the reduced diffusion coefficient of the ATG2A-positive phagophore population is the result of ATG2A-mediated tethering of the phagophore to donor membranes. The rapidly diffusing population of autophagy factors foci (D = 0.01 $\mu m^2/s$) is comparable to the diffusion coefficient of static ATG9A vesicles measured in our single-molecule imaging experiments (D = 0.02 $\mu m^2/s$). Immobilization of an ATG9A vesicle by tethering it to other cellular membranes via ATG2A would be expected to reduce its diffusion coefficient, which is consistent with our observations. For instance, yeast ATG9A vesicles directly involved in the formation of autophagosomes show distinct diffusive behavior than vesicles freely diffusing in the cytosol (Yamamoto et al., 2012). Our results demonstrate that inhibition of phagophore closure by knockdown at CHMP2A leads to the enrichment of ATG13 foci which were tightly associated with the ER. This observation is consistent with the accumulation of phagophores that have undergone expansion by ATG2A-mediated lipid transfer but remain tethered to the ER due to their inability to close and form mature autophagosomes. In contrast, it is not immediately apparent why ATG2A recruitment should reduce the mobility of the phagophore if it was formed by an alternative ER-remodeling mechanism. In addition, our observations suggest that the ULK1 complex, PI3-kinase, the LC3 lipidation machinery, and to a smaller degree WIPI2 can be recruited to ATG9A vesicles prior to their tethering to donor membranes by ATG2A.

Together these observations demonstrate that the recruitment of ATG2A marks the transition from an ATG9A vesicle into a phagophore that can expand and mature into an autophagosome.

ULK1 is the limiting factor for the assembly of the ULK1 complex

A key open question is how ATG9A vesicles are specifically selected to transform into autophagosomes. The ULK1 complex, composed of ULK1, ATG13, FIP200, and ATG101 is essential in the initiation of autophagy (Dikic and Elazar, 2018; Lin and Hurley, 2016; Yu et al., 2018). Work by others has demonstrated that ATG13 and FIP200 are required for the localization of ULK1 to the phagophore (Chang et al., 2021a; Ganley et al., 2009;

Kannangara et al., 2021; Shi et al., 2020). A key function of the ULK1 complex is the activation of the PI3-kinase VPS34 at sites of autophagosome formation to promote the production of PI3P (Mercer et al., 2018; Park et al., 2016; Russell et al., 2013). In addition, it has been shown that ULK1 complex recruitment to the phagophore is re-enforced by the association of ATG13 with PI3P (Karanasios et al., 2013a). Therefore, the ULK1 complex and PI3-kinase form a positive feedback loop required to initiate autophagosome formation (Ohashi, 2021).

Our observations demonstrate that ATG13 is 9-fold more abundant than ULK1, therefore ULK1 kinase is the limiting factor in ULK1 complex assembly. Despite the differences in protein abundance, similar amounts of ULK1 and ATG13 are recruited to phagophores, suggesting they act in concert during autophagosome biogenesis. Interestingly, clinical studies, have shown that ULK1 overexpression is associated with a poor patient prognosis (Lu et al., 2018; Yun et al., 2015), suggesting that ULK1 kinase levels control the overall activity of the ULK1 complex, confirming that ULK1 is a promising clinical target (Martin et al., 2018).

The initiation of autophagosome formation is inefficient

Previous work by others has largely focused on determining the number of cytoplasmic autophagy factor foci as a measurement of autophagosome formation, and a limited number of studies have analyzed the lifetime of foci formed by autophagy proteins (Dalle Pezze et al., 2021; Karanasios et al., 2013a; Karanasios et al., 2013b). Our dual color imaging of the tagged autophagy proteins and P62, GABARAPL1, or LC3, which mark phagophores that are in the process of cargo sequestration and mature autophagosomes, allowed us to systematically analyze the kinetics and efficiency of phagophore maturation.

Surprisingly, approximately 90% of the foci formed by ULK1, ATG13, WIPI2, ATG5, and ATG16 do not proceed to accumulate detectable quantities of P62, GABARAPL1, or LC2. In addition, autophagy protein foci that do not co-localize with P62, GABARAPL1, or LC3 are very short-lived (P62^{negative} mean = 33 s; LC3^{negative} mean = 25 s, Halo-ATG13 GABARAPL1^{negative} mean = 24 s), compared to foci that proceed to accumulate P62, GABARAPL1, or LC3 (P62^{positive} mean = 107 s; LC3^{positive} mean = 125 s, Halo-ATG13 GABARAPL1^{positive} mean = 80 s). These observations suggest that these short-lived foci represent aborted autophagosomes that initiate the accumulation of the ULK1 complex, WIPI2, and the LC3 lipidation machinery, but rapidly disassembly rather than maturing into an autophagosome. The use of three distinct markers, the adaptor P62 and ATG8-like family proteins LC3 and GABARAPL1, increases our confidence that these observations are a general feature of autophagosome formation, rather than a feature of a specific subset of autophagosomes. It is important to note that our observation that 90% of ULK1, ATG13, WIPI2, ATG5, and ATG16 foci do not proceed to accumulate P62, GABARAPL1, or LC3 is likely an overestimation. Our methodology to track the adaptor protein and autophagy factor foci and to determine their co-localization is very stringent and we likely fail to detect all co-localized trajectories. The close correspondence of the lifetimes of autophagy protein foci that co-localizes with P62 and LC3 strongly suggests that both LC3 and P62 mark the same structure: bona fide autophagosomes.

Strikingly, our analysis of the maturation of ATG2A foci revealed that they are twice as likely to co-localize with P62 compared to the other autophagy factors analyzed (**Fig. 2.6D**). As discussed above, the number of ATG2A foci formed is approximately half of the number formed by ULK1, ATG13, ATG5, and ATG16. Therefore, the total number of foci formed by all autophagy factors analyzed that proceed to co-localize with an adaptor protein is comparable. In addition, the fraction of ATG13 foci that proceed to recruit ATG2A (12%) and adaptor proteins (10-16%) is similar. In addition, the lifetime of ATG13 foci that recruit ATG2A or P62/LC3/GABARAPL1 are comparable (80-100 s), pointing that the co-localization of ATG13 and ATG2A marks phagophores that will complete maturation. Together these observations demonstrate that the majority of autophagy protein foci do not mature to form autophagosomes and further support our model that the recruitment of ATG2A and the concomitant tethering to donor membranes is a critical step in committing ATG9A vesicles toward maturation into an autophagosome (**Fig. 2.9**).

Endogenous tagging combined with automated tracking reveals the maturation kinetics of autophagosomes in human cancer cells

Foci formed by autophagy proteins have been extensively used to infer the lifetime of autophagosomes (Dalle Pezze et al., 2021; Fujita et al., 2008; Karanasios et al., 2013a; Karanasios et al., 2016; Stavoe et al., 2019). Current estimates of autophagosome lifetime rely upon manual identification and analysis of foci formed by stably expressed, fluorescently tagged autophagy protein transgenes (Dalle Pezze et al., 2021; Karanasios et al., 2013a). Using our cell lines that express fluorescently tagged autophagy proteins from their endogenous loci avoids known artifacts due to protein overexpression and provides consistent experimental conditions to directly compare individual autophagy factors. In addition, our observations described above demonstrate that a large fraction of autophagy protein foci does not mature into autophagosomes. To accurately analyze the kinetics of autophagosome formation it is therefore necessary to combine the detection of autophagy factor foci with a marker of mature autophagosomes, such as P62, LC3B, or GABARAPL1. In addition, our fully automated detection and particle tracking approach provides an unbiased method that generates a tremendous amount of data.

Our observations demonstrated that all autophagy factors analyzed accumulated approximately 40 seconds prior to P62 recruitment. This suggests that ULK1, ATG13, ATG5, ATG16, WIPI2, and ATG2A are all recruited in rapid succession (**Fig. 2.9**). Our current imaging approach does not have the time resolution required to determine a precise recruitment order of the autophagy factors analyzed. In general, we note that previous analysis of foci reports longer-lasting values than our data shows. For instance, previous analysis of ATG5 and ATG13 recruitment kinetics showed ATG5 foci lasting 480 seconds and ATG13 foci which lasted for 200 seconds on average (Dalle Pezze et al., 2021; Karanasios et al., 2013a; Koyama-Honda et al., 2013), compared to the average lifetime of 102 and 82 seconds that we observed in our experiments, respectively. The potential discrepancy may be due to the detection method, expression approach, or cell line differences. Once P62 accumulation is detectable the autophagy factors remain associated with the phagophore for 50-95 seconds, and the P62 signal is detected for 40-100 seconds after the autophagy proteins have dissociated from the autophagosome (**Fig. 2.9**). This demonstrates that the autophagy factors we analyzed in this study are recycled and therefore must be largely associated with the cytosol-facing membrane of the autophagosome. This is further supported by the recent observation that the HaloTag protein is resistant to lysosomal degradation (Yim et al., 2022). If the HaloTagged autophagy factors were sequestered inside the autophagosome we would expect to observe an accumulation of fluorescence signal in the lysosome, which was only observed for Halo-LC2. We assume the dissociation of the core autophagy factors analyzed in this work is closely correlated with the completion of phagophore expansion and its closure to form a mature autophagosome.

Importantly, we measured similar kinetics when using GFP-LC3, GFP-GABARAPL1, and GFP-P62 expressed by viral transduction and/or stably expressed from a single-genomic insertion as a marker for autophagosomes, which confirms that the P62 signals detected represent autophagosomes rather than protein aggregates marked by P62. LC3 accumulated more rapidly (~16 s) after autophagy protein foci formation compared to P62 (~40 s), consistent with the LC3-dependent recruitment of P62 to phagophores (Ichimura et al., 2008; Kirkin and Rogov, 2019; Noda et al., 2008; Pankiv et al., 2007). Overall, similar to autophagy protein foci length, the lifetime of LC3, GABARAPL1, and P62 positive autophagosomes is substantially shorter than previously reported in the literature (Dalle Pezze et al., 2021; Karanasios et al., 2013a; Karanasios et al., 2013b) (**Fig. 2.9**). We assume that the disappearance of the adaptor or the ATG8 family protein signal is a consequence of the fusion of the autophagosome with the lysosome, which quenches the fluorescent signal of GFP. The quenching of the GFP signal suggests that the average time from the completion of autophagosome formation to autophagosome-lysosome fusion is ~66 s (ranging from 38-101 s). In total, these experiments demonstrate that the average timeframe of autophagosome biogenesis is 110 seconds (ranging from 90-145 seconds) in U2OS cells (**Fig. 2.9**). Importantly, the autophagosome lifetime we determined using automated tracking of thousands of autophagy factor foci was comparable in all HaloTagged autophagy protein cell lines, raising our confidence that we are measuring the lifetime of bona fide phagophores that mature into autophagosomes. The similarity in the overall lifetimes measured also indicates that the autophagosome formation kinetics are not adversely affected by the HaloTag fusion proteins. Finally, our observations demonstrate that all autophagy factors analyzed are removed from autophagosomes prior to the fusion of the autophagosome with the lysosome. This suggests that the signal that leads to the recruitment of these proteins, likely the enrichment of PI3P, is removed from the autophagosome once it has closed and is fully matured (**Fig. 2.9**). In total, these experiments precisely define the overall lifetime of autophagosomes, the timing of phagophore maturation, and the time it takes for a mature autophagosome to fuse with a lysosome.

Altogether our work significantly expands our mechanistic understanding of autophagosome formation and provides a sophisticated experimental framework and toolkit for future quantitative studies of autophagy in human cancer cells.

Data availability

Data are available in the article itself and its supplementary materials. Live-cell imaging datasets are openly available in a public repository (https://doi.org/10.5061/dryad.866t1g1vh).

Acknowledgments

The order of authors was decided by a randomization process and both authors contributed equally to the paper; co-first authors reserve the right to list themselves first on their curriculum vitae. This work was supported by a grant from the NIH (DP2 GM142307) to J.C.S. J.C.S. was a Damon Runyon Dale F. Frey Scientist supported (in part) by the Damon Runyon Cancer Research Foundation (DFS-24-17). We thank Dr. Daniel T. Youmans and Dr. Thomas R. Cech for providing the plasmid for recombinant production of the 3xFLAG-HaloTag protein, and Luke D. Lavis for generously providing the Janelia fluor dyes. We thank Dr. Eric Patrick for contributing to the preparation of the recombinant HaloTag protein used in this study. We acknowledge the Flow Cytometry core (Research Technology Support Facility, Michigan State University) and the Confocal Laser Scanning Microscopy core (Center for Advanced Microscopy, Michigan State University) for supporting our cell sorting and microscopy experiments. The authors declare no competing financial interests.

Author contributions

Conceptualization: D.G.B., C.B., and J.C.S.; Experiments: D.G.B., C.B., G.I.P.; Data Analysis: D.G.B. and C.B.; Writing – Original Draft: D.G.B. and C.B.; Writing – Review and Editing: D.G.B., C.B., and J.C.S.

Materials and methods

Cell lines

All cell lines used in this study were derived from human bone osteosarcoma epithelial cells (U2OS, ATCC HTB-96) and grown in RPMI cell culture media supplemented with 10% fetal bovine serum (FBS), 100 units/ml penicillin, 100 µg/ml streptomycin at 37°C with 5% CO_2.

Plasmid Construction and Genome Editing

The autophagy genes were edited at their endogenous 5’-end, except for ULK1, which was edited at the 3’ end. For the 5’-end editing, the 3XFLAG-HaloTag donor plasmid was generated according to the procedure described by Xi et al. (Schmidt et al., 2016; Xi et al., 2015). Between the HaloTag and the start codon of the tagged gene, a linker sequence including a TEV protease cleavage site was inserted. The homology arms and HaloTag fragments were ligated into pFASTBac linearized with HpaI using Gibson

Assembly (NEB). All single-guide RNAs (sgRNAs) were cloned into pX330 Cas9 donor plasmid (Cong et al., 2013). Cells were transfected using the FuGENE HD® transfection reagent (Promega Co.); after 72h of transfection, the cells were selected for 4-6 days with puromycin (1µg/ml). Following selection with puromycin, cells were transfected with an eGFP-CRE recombinase plasmid. Cells were then labeled with the HaloTag ligand JF646 (Janelia) and sorted with FACS using the eGFP/JF646 positive signals. In single-cell clones, homologous recombination was confirmed by PCR and Sanger sequencing. Halo-NES, SNAP-SEC61 (in the U2OS parental cell line), LAMP1-mNeon (Lamp1-mNeonGreen was a gift from Dorus Gadella; Addgene plasmid # 98882 ; http://n2t.net/addgene:98882 ; RRID:Addgene_98882) (Chertkova et al., 2017), and the GFP-tagged ATG8 family proteins (LC3, GABARAPL1), and the adaptor P62 (in the genome-edited Halo-ATG13 cell line) were stably expressed by introducing the coding sequence at the AAVS1 safe-harbor locus (PPP1R12C) (Qian et al., 2014). All PCR oligonucleotides and sgRNA sequences are listed in the supplemental Table 1.

Western Blotting

The protein samples were separated on 4–15%, or 4-20% TGX stain-free polyacrylamide gels (Biorad), followed by standard western blotting procedures. The primary and secondary antibodies and dilutions used are listed in supplemental table 1. Clarity western ELC Substrate (BioRad) was used to generate a chemiluminescence signal detected with a ChemiDoc imaging system (BioRad). All western blot quantification was carried out using the ImageQuant™ software (Cytiva). Expression levels of the edited cell lines were estimated by comparing the chemiluminescence signal with the parental U2OS after normalization with the stain-free signal.

LC3 lipidation assay

Cells were grown in 24-well plates at 60-70% confluency and treated with 100nM rapamycin and 100nM rapamycin + 100nM bafilomycin for 2h; a control in regular RPMI media was also performed. After treatment, the cells were harvested with 150µl sample buffer, and 20ul were loaded in a 4-20% Bis-Tris gel. Gels were transferred into PVDF blot and treated against LC3 antibody according to the protocol supplied by the provider (CellSignaling). The chemiluminescence signal was detected with a ChemiDoc imaging system (BioRad) and the signal corresponding to LC3-I and LC3-II was quantified using the ImageQuant™ software (Cytiva).

Expression and Purification of Recombinant His-3XFlag-HaloTag

The His-3X-FlagHaloTag construct was kindly provided by Dr. Youmans and Dr. Cech at the University of Colorado. HaloTag protein was expressed and purified from E. coli BL21(DE3) cells grown in LB medium. Cells were grown at 37°C and expression was induced at OD ~0.5-0.8 with 1mL of IPTG (1M). Upon induction, the temperature was decreased to 18°C, and cells were grown overnight (16h) before harvesting. Cells were centrifugated, the pellet resuspended in wash buffer (50 mM sodium phosphate buffer pH 8.0, 300 mM sodium chloride, 10 mM imidazole, 5 mM beta-mercaptoethanol), and sonicated for 2 min (40% amplitude, 90 seconds of sonication, 10-second pulses, 20-second pause, FisherbrandTM Model 505, 0.5-inch tip). The lysate was then centrifuged (40,000g and 4°C for 30min) and the supernatant was loaded to 1 mL of in fast flow nickel Sepharose (Cytiva) and incubated under gentle rotation for 1h at 4°C. Beads were then washed 3 times with 6ml of wash buffer, and elution was performed using elution buffer (0 mM sodium phosphate buffer pH 7.0, 300 mM sodium chloride, 250 mM imidazole, 5 mM beta-mercaptoethanol). The eluate was subjected to further purification using size-exclusion chromatography on a Superdex S75 column in isocratic mode (50 mM Tris pH 7.5, 150 mM potassium chloride, 1 mM DTT). Protein was concentrated to 1mg/ml, supplemented with 50% glycerol, flash-frozen, and stored at -80°C. To fluorescently label the 6xHIS-3xFLAG-HaloTag, the protein was incubated with a 2-fold excess of JF646 HaloTag-ligand overnight at room temperature. Excess fluorescent dye was removed by size exclusion chromatography using a Superdex S75 column in isocratic mode (50 mM Tris pH 7.5, 150 mM potassium chloride, 1 mM DTT). The protein concentration and labeling efficiency were determined by absorption spectroscopy using ε_{280nm} = 41,060 M^{-1} cm^{-1} for the 6xHIS-3xFLAG-HaloTag and ε_{646nm} = 152,000 M^{-1} cm^{-1} for the JF646 fluorescent dye (Grimm et al., 2015).

In-Gel Fluorescence Absolute Protein Quantification

His-3XFlag-HaloTag was labeled by combining 15 nmol of JF646 (30ul from 0.5mM DMSO resuspended stock) to 0.2 mg recombinant protein in 200µl of buffer and incubated at RT for 30 minutes. The labeled protein was then purified by size exclusion on an S75 column. Fractions were combined and concentrated in Vivaspin 10 kDa columns and glycerol was added for a final concentration of 20%. Vials were snap-frozen in liquid nitrogen and stored at -80°C. The final concentration was measured using a 40ul microcuvette in a fluorescence spectrophotometer. Protein concentration was calculated using an extinction coefficient ε_{646nm} =152,000 M^{-1} cm^{-1} (Grimm et al., 2017). The labeled HaloTag protein was then serial diluted in sample buffer and a total of 37.5 fmol down to 0.29 fmol was added to cell lysates that were prepared using direct lysis in sample buffer and diluted from 150,000 cells/mL to 75,000 cells/mL in 25,000 cell/mL increments. The standards were then aliquoted into individual use tubes, boiled, snap-frozen in liquid nitrogen, and stored at -80°C. For the in-gel fluorescence, 80,000 cells were seeded in a 24-well plate. Cells were harvested by adding 30 µl of 1xSDS PAGE sample buffer (Biorad). The protein and the standard were loaded and separated on 4–15% TGX stain-free polyacrylamide gels (Biorad). Fluorescence was detected using the Cy5.5 settings on a ChemiDoc imaging system (BioRad). The gels were quantified using the ImageQuant™ software (Cytiva). We observed that the band patterns of each protein affected the quantification of both in-gel fluorescence (density of bands) and western blots (density of bands along with biased transfer). To correct for these biases, we cleaved the HaloTag using TEV protease to compare the fluorescence of the purified HaloTag to cleaved HaloTag, and the endogenous proteins with cleaved autophagy proteins (**Appendix Fig. 10D, Appendix Fig. 10F-G**). For the TEV in-gel fluorescence corrections, 120,000 cells were labeled for 30 minutes with 500 nM JF646, washed with PBS, harvested with 5 mM EDTA in PBS, and pelleted. Samples were lysed in 60 µL CHAPS lysis buffer (10 mM TRIS pH 7.5, 1 mM $MgCl_2$, 1 mM EGTA, 0.5% CHAPS, 10% glycerol) and 20 µL incubated on ice with 5 units of TEV protease (New England Biolabs, P8112) for 30 minutes. Following TEV cleavage, 5 µL 6x SDS sample buffer were added to 25 µL of the digested and undigested samples and boiled for five minutes at 95°C. Samples were then separated by gel electrophoresis. JF646 intensity was measured using the ChemiDoc imaging system (BioRad) and cleaved HaloTag protein was compared to uncleaved full-length HaloTag autophagy factor fusion protein. For TEV-westerns, the protocol followed was similar, but the cells were not labeled and a 50% dilution per sample was added. Gels were transferred using the Trans-Blot Turbo system (with Turbo transfer buffer) (BioRad) onto PVDF or Nitrocellulose. Samples were blocked in 5% milk powder for 1hr, washed in PBST, and left overnight in primary antibody. The following day, blots were washed and incubated in goat anti-mouse HRP (Invitrogen, 31430, 1:2000), goat anti-rabbit HRP (Invitrogen, 31460, 1:2000), and chemiluminescence was measured. Finally, we calculated the cellular protein abundance by first determining the total number of HaloTagged proteins by comparing the in-gel fluorescence signal of the tagged autophagy factor with the HaloTag standard curve. We then measured the total number of cells loaded using the stain-free protein signal compared to the cell number standard curve. Dividing the total number of HaloTag molecules by the number of cells loaded resulted in total protein abundance with the units of molecules per cell. This measurement was then corrected by multiplication with the TEV correction factor (fluorescent signal of the full-length fusion divided by cleaved HaloTag signal) and the western blot correction factor (western blot signal of the full-length fusion protein divided by endogenous length protein signal). The protein abundance was computed for two different cell clones; the measurement error was propagated using standard deviation.

Flow cytometry measurement of protein abundance

80,000 cells were plated into a 24-well plate. 24 hours after seeding cells were then labeled with JF646 at 500nM for 30 minutes in complete media and washed with a 5-minute incubation in media. Cells were then harvested using 5mM EDTA in PBS (10 min at 37°C) and transferred to a 2 ml deep 96-well plate using a multichannel pipette. Paraformaldehyde (PFA) fixation solution was added for a final concentration of 2% PFA in PBS and incubated for 10 minutes. Samples were then washed once with 1% BSA in PBS and filtered into a 96-well round-bottom plate using a nylon mesh with a 70 µm pore size. Analysis was performed on a Cytek Aurora (Cytek Biosciences) using a 96-well loader and unmixed using the default SpectroFlo software (Cytek Biosciences).

Immunofluorescence to detect LC3 foci in fixed cells

Halo-ATG5, Halo-ATG16, and Halo-WIPI2 cells were plated (200,000 cells) into an ethanol-sterilized 6-well plate containing 22X22 #1.5 glass coverslips and left overnight to adhere. Cells were then labeled with JF646 at 500nM for 30 minutes in complete media and washed with a 5-minute incubation in media. Cells were then treated for 2 hours with DMSO control, rapamycin (100nM), or rapamycin with bafilomycin (100nM). After 2 hours of drug treatment, cells were washed in PBS and fixed in 4% PFA in PBS (10 min at room temperature). The fixed coverslips were then transferred to a humidified chamber and washed 3 times in PBS for 5 minutes and simultaneously blocked/permeabilized with 3% BSA in PBS with digitonin (50ug/ml) for 30 minutes. Digitonin was added throughout the rest of the experiment for incubation steps. The primary antibody was diluted in 3% BSA in PBS, added at the indicated concentration, and incubated overnight. The samples were then washed 3 times in PBS and incubated with AlexaFlour conjugated secondary antibody (Invitrogen) for 1 hour (1:500) in 3% BSA in PBS. The samples were washed 3 times in PBS and once in water then flipped upside down onto the micro slides containing a drop of antifade mountant (ProLong Diamond, Life Technologies), dried for 10 minutes, and sealed with nail polish.

Live cell microscopy

Live cell imaging experiments were carried out using two distinct microscopes. An Olympus microscope (IX83), with a cellTIRF illuminator with four laser lines (100 mW 405nm, 200 mW 488nm, 300 mW 561nm, and 140 mW 640 nm) and an X-Cite TURBO multi-wavelength LED illumination system (Excelitas Technologies). The microscope is equipped with an environmental chamber (cellVivo) to control humidity, temperature, and CO_2 level, a 100x TIRF oil-immersion objective (Olympus UApo N, NA = 1.49), a 60x TIRF oil-immersion objective (Olympus UPlanApo, NA = 1.50), a 60X oil immersion objective (Olympus PlanApo N, NA = 1.42), and the appropriate excitation and emission filters. For signal detection, this microscope uses two Andor iXon Ultra 897 EMCCD or two Hamamatsu Orca Fusion BT sCMOS cameras attached to a Twin-cam beamsplitter (Cairn Research). Alternatively, we used an i3 spinning disc confocal microscope equipped with a CSU-W1 confocal spinning disk system (Yokogawa), five laser lines (100 mW 445nm, 150 mW 488nm, 175 mW 515 nm, 160 mW 561nm, and 140 mW 638 nm), a Prime 95B sCMOS camera (Photometrics), a 63X oil-immersion objective (Zeiss C Plan-Apo, NA = 1.4), and an incubation chamber to control humidity, temperature, and CO_2 level. All live cell imaging was carried out at 37°C, and under 5% CO_2-containing humidified air.

Autophagy protein and LC3 foci quantification in living cells

Cells (10,000) were grown in 96-well optical plates and after 24h transduced with GFP-LC3 encoding baculovirus particles using the viral BacMam 2.0 transfection reagent at a concentration of ~0.25×10^8 viral particles/mL. After 24h, cells were labeled with 100nM JF646 for 10 min, followed by 3 washed with growth media and 5 min bleeding at 37°C. A nuclear stain (Hoechst dye, diluted 1:10000) was added during the last wash step. For starvation, cells were washed 3 times with PBS buffer before the addition of EBSS starvation media. Cells were imaged on the Olympus microscope, using the Olympus PlanApo N, NA = 1.42, the Andor iXon 897 Ultra camera, using the 630 nm LED at 100%

power, the 475 nm LED at 30% power, and the 385 nm LED at 5% power. To avoid signal saturation, for Halo-LC3 the 630 nm LED power was set at 20%. For each cell line, a single frame was taken at 100 ms exposure for the three channels. Images were processed using a home-built foci analysis algorithm written in ICY software (BioImage Analysis Lab) (de Chaumont et al., 2012).

Single-Molecule Live-Cell Imaging

We performed single-particle tracking analysis for determining diffusion coefficients of HaloTagged autophagy protein under control and EBSS starving conditions. Single-molecule live-cell imaging was carried out on the Olympus microscope using the 640 nm laser (~25% power) in a HILO angle and the Andor iXon 897 Ultra camera was used for signal detection. Cells (200-300,000) were grown on glass coverslips (170 ± 5 μm, Schott) and imaged 24 hours after seeding. Coverslips were cleaned with 1M KOH (1h in a sonicated water bath), rinsed with ddH_2O, cleaned with 100% ethanol (1h in a sonicated water bath), and dried under N_2 stream before assembly on a 35 mm diameter imaging dish. Precise determination of diffusion coefficient using single-particle tracking requires sparse labeling of the Halo-tagged protein. Cells were labeled with Halo ligand JFX650 with the following optimized conditions: 1.0 nM, 30s pulse (ATG9A); 500pM, 30s pulse (WIPI2, ULK1, ATG2A, ATG5, ATG13, ATG16L1, PI4KIIIβ); 50pM, 30s pulse (LC3, SEC61, Halo-NES). These labeling conditions allowed a maximum of 10-15 particles per frame throughout the entire imaging experiment (146 frames per second, 3000 frames, 140×512 pixel region of interest). After labeling, the cells were washed three times with fresh media and incubated for an additional 10 min in complete media containing 7-bromophenol (10μM) to block unreacted HaloTag proteins at 37°C (5% CO_2). Before adding EBSS, cells were washed 3X with PBS. EBSS-treated samples were imaged within one hour of treatment.

Diffusion coefficient determination

For detecting individual single-molecule particles and computing particle tracks, we used the batch parallel-processing version of SLIMFast in MatLab 2020b. This software – kindly provided by Xavier Darzacq and Anders Hansen – allows direct import of the TIFF files and uses the MTT algorithm for signal detection and particle tracking (Sergé et al., 2008). The following settings were used for all the proteins: Exposure Time = 6.8 ms, NA = 1.49, PixelSize = 0.16 μm, Emission Wavelength = 664 nm, D_{max}= 15 μm^2 s^{-1}, Number of gaps allowed = 2, Localization Error = 10^{-5}, Deflation loops = 0. For ATG9, the D_{max} was set at 5 μm^2 s^{-1}. From the tracked particles, we determined the diffusion coefficients and the fraction corresponding to distinct particle subpopulations using the MATLAB version of SpotOn (kindly provided by Xavier Darzacq and Anders Hansen) (Hansen et al., 2018). The following settings were used: TimeGap = 6.8 ms, dZ = 0.700 μm, GapsAllowed = 2, Time-Points = 7, JumpsToConsider = 4, BinWidth = 0.01 μm, PDF-fitting, D_Free1_3State = [2 15], D_Free2_3State = [0.15 2], D_Bound_3State = [0.0001 0.15]. For ATG9A, a 2-state model was applied, with the following settings: D_Free2_1State = [0.2 5], D_Bound2_State = [0.0001 0.2]. We carried out 3 independent biological replicates with at least 20 cells for each cell line for all experiments.

Determination of HaloTag autophagy protein foci lifetime

Autophagy protein foci lifetimes were determined in the HaloTag-edited cell lines by live-cell imaging. Cells were imaged on the Olympus microscope, using the Olympus PlanApo N, NA = 1.42, the Andor iXon 897 Ultra camera, using the 630 nm LED at 100% power.

Cells (150,000) were grown on glass coverslips (170 ± 5 μm, Schott) and imaged 48 hours after seeding. Cells were labeled with Halo ligand 100nM JF646 in complete media for 10 minutes, which allows quantitative labeling of HaloTagged proteins. After labeling, the cells were washed three times with fresh media and incubated for an additional 10 min in complete media containing 7-bromophenol (10μM) to block unreacted HaloTag proteins at 37°C (5% CO_2). Before adding EBSS, cells were washed 3X with PBS. EBSS-treated samples were imaged within one hour of treatment. For each condition, four cell clusters (4-6 cells per cluster) were selected and imaged at 15 second-time intervals (50 ms exposure time) for 1 hour, corresponding to 240 frames per movie. For ATG2A and ATG13, cells were also imaged at a faster rate (3 seconds) for over 240 frames. The experiments were run in triplicate, with approximately 20-30 cells imaged per cell line for each replicate. Foci were treated as single particles and analyzed using TrackIT (Kuhn et al., 2021) with the following settings: threshold 1.5; tracking radius 6; minimum track length 2; gap frames 2.

Determination of foci colocalization with P62, LC3, and GABARAPL1 foci

Cells were seeded at low confluency (100,000) on glass coverslips (170 ± 5 μm, Schott). After 24 hours, cells were transduced with GFP-LC3 or GFP-P62 encoding baculovirus particles using the viral BacMam 2.0 transfection reagent at a concentration of ~0.25 x 10^8 viral particles/mL. After an additional 24 hours for viral transduction, cells were labeled for foci visualization (100 nM JFX650 for 10 minutes in complete media) and imaged in control and EBSS starvation media (Grimm et al., 2021). Before adding EBSS, cells were washed 3X with PBS. EBSS-treated samples were imaged within one hour of treatment. Cells were imaged on the Olympus microscope, using the Olympus PlanApo N, NA =

1.42, the Andor iXon 897 Ultra camera, using the 630 nm LED (100% power) and the 475 nm LED (30% power). For each condition, four cell clusters (4-6 cells per cluster) were selected and imaged in 3 seconds time intervals (50 ms exposure time) for 12 min. The experiments were run in triplicate, with approximately 20-30 cells imaged per cell line for each replicate. Additional experiments were performed for the Halo-ATG13 cell line stably expressing GFP-tagged adaptors LC3, P62, and GABARAPL1 from the AAVS1 safe harbor locus. Cells were imaged on the same Olympus microscope, with the Olympus TIRF 60x UPlanApo NA = 1.50 objective, and the Hamamatsu Orca-Fusion BT sCMOS camera. For each condition, four cell clusters (4-8 cells per cluster) were selected and three z-planes (center plane and ± 2 μm) were imaged at 1.5 second time intervals (50 ms exposure time) for 8 min. The experiments were run in triplicate, with approximately 40-60 cells imaged per cell line.

Automated Autophagy protein foci tracking and colocalization

Autophagy protein foci were treated as single particles and analyzed using TrackIT (Kuhn et al., 2021) with the following settings: threshold 1.5; tracking radius 6; minimum track length 2; gap frames 6. Tracks were exported and analyzed with a custom Matlab (v. 2022a) algorithm. The algorithm calculated the Euclidean distance between the tracked autophagy factor foci coordinates and the nearest GFP-tagged marker (LC3, P62, or GABARAPL1) signal coordinates. If the calculated distance was ≤ 3 pixels (0.81 μm or 0.33 μm for the Andor and Hamamatsu cameras, respectively), the marker signal was considered colocalized with the tracked autophagy protein particle. An autophagy factor track was considered colocalized with a marker track if at least 4 colocalized events were recorded over the duration of the autophagy factor track. The duration of colocalization between the autophagy factor foci and the marker foci was calculated by determining the difference between the first and last colocalization events.

Step-size analysis was carried out with a home-built algorithm written in MatLab. Diffusion coefficients for the autophagy factors foci were computed using MSDAnalyzer (Tarantino et al., 2014) implemented in MatLab or built in the TrackIt package. In both cases, the algorithm fits the mean-squared displacement (MSD) curve obtained from the single-particle tracks with a power law equation describing anomalous diffusion. For diffusion analysis, only 60% of the track was fitted.

Live-cell imaging of ATG13 with an ER marker

We visualized ATG13 foci in control cells (siCTR) and upon siRNA knock-down of CHMP2A (siCHMP2A). siRNA experiment was performed using previously validated siRNA pools (Takahashi et al., 2018) and nucleofection was performed according to the supplier's recommendation (control siRNA (D-001810-10-05), siCHMP2A (L-020247-01-0005), both supplied by Horizon). mEmerald-SEC61 (a gift from Jennifer Lippincott-Schwartz, Addgene plasmid # 90992; http://n2t.net/addgene:90992; RRID:Addgene_90992) was added to the siRNA transfection and effective protein depletion was verified at 40 hours after siRNA transfection using western blot using a CHMP2A antibody (Takahashi et al., 2018). The cells were seeded at low confluency (100,000 cells) on glass coverslips (170 ± 5 μm, Schott). The Halo-ATG13 was labeled with JFX650 dye (100 nM in complete media for 10 min) 40 hours after transfection and imaged on the Olympus microscope, using the Olympus TIRF 60x UPlanApo NA = 1.50, using the 630 nm LED (100% power) and the 475 nm LED (30% power), and the Hamamatsu Orca Fusion BT camera. The ER signal was restored to high resolution using

CARE, a machine-learning algorithm (Weigert et al., 2018) implemented in ImageJ, referred as CSBDeep plugin. The image deconvolution was performed using a pre-trained microtubules training set.

Live-cell imaging of ATG9A with LAMP1 lysosomal marker

Halo-ATG9A stably expressing LAMP1-mNeon, a lysosomal marker, were transfected with 2.5 µg of RFP-ATG9A (a gift from Noboru Mizushima; Addgene plasmid # 60609 ; http://n2t.net/addgene:60609 ; RRID:Addgene_60609) (Koyama-Honda et al., 2013) using a 4D-Nucleofector unit (Lonza). Nucleofection was performed according to the supplier protocol. The cells were seeded at low confluency (100,000 cells) on glass coverslips (170 ± 5 µm, Schott). Halo-ATG9A was labeled with JFX650 dye (100 nM in complete media for 10 min) 24 hours and 48 hours after transfection, to determine if the aging of Halo-ATG9A protein changes its localization with lysosomes. Cells were imaged 48 hours after transfection with a 3i spinning disc confocal microscope with the 488 nm laser (10 ms exposure time, 3% laser power), the 561nm laser (100ms exposure time, 100% laser power), and the 640 nm laser (100ms exposure time, 100% laser power) and imaged at 1 frame per second for 1 min.

Live-cell imaging of Halo-ATG9A and SNAP-LC3B with Deep Red Lysotracker

100,000 double-edited cells expressing Halo-ATG9A and SNAP-LC3B from their endogenous loci were plated in a 35mm glass bottom dish. The following day, cells were labeled with Halo ligand JFX554 (100 nM in complete media for 10 min) and imaged the same day (0 hours experiment) or the subsequent day (24 hours experiment). SNAP-LC3B was labeled with JF503 SNAP-ligand (100 nM in complete media) overnight prior to imaging. Samples were then labeled with Deep Red LysoTracker (Invitrogen, 2.5nM in complete media for 30 min) after labeling the Halo-ATG9A. Cells were washed in complete media and imaged with the 3i spinning disc confocal microscope with the 488 nm laser (10 ms exposure time, 3% laser power), the 561nm laser (100 ms exposure time, 100% laser power), and the 640 nm laser (100 ms exposure time, 100% laser power) and imaged at 1 frame per second for 1 min.

Halo-ATG9A trafficking and stability experiments

ATG9A was knocked out of a Halo-ATG9A cell line using the spCas9 and sgRNAs targeting the 3xFLAG-HaloTag coding sequence and 3 exon of the ATG9A coding sequence (see Supplemental Table 1) and knock out cells were identified by the lack of HaloTag fluorescence. Halo-ATG9A subsequently added back into the AAVS1 safe locus with a tet-inducible promotor. This Halo-ATG9A add-back cell line was grown with or without 2 µg/ml doxycycline in tetracyclin-free media (Invitrogen). 200,000 cells were then plated in a six-well dish and doxycycline was added to induce Halo-ATG9A expression in the samples that were grown without doxycyclin (2 µg/ml) and cells were grown in doxycycline-containing media for the remainder of the experiment. The following day, the cells were labeled with JFX650 (100 nM in complete media for 10 min) and the 0-hour timepoint was harvested by the addition of 100 µl of 1x SDS PAGE sample buffer. 24 hours and 48 hours after labeling additional samples were harvested. Samples were boiled for 5 minutes before being separated on 4-15% TGX stain-free polyacrylamide gels (Biorad). Fluorescence was detected using the Cy5.5 setting on the ChemiDoc imaging system (BioRad). For live-cell imaging, the cells were treated as described above, except for the following additions. Endogenously edited Halo-ATG9A was added as a control to compare intensities with doxycycline-induced Halo-ATG9A cells. Additionally, as a control, U2OS and Halo-ATG9A knock-out cells were labeled with JFX650 HaloTag-ligand and imaged at 0 and 24 hours after labeling, to assess non-specific JFX650 fluorescence signal.

Live-cell imagining of RFP-ATG9A

Plasmids for the expression of RFP-ATG9A (1 ug) and GFP-SEC61 (1 ug) were co-transfected with lipofectamine 3000 according to the manufacturer's instructions in U2OS cells. In an additional experiment, RFP-ATG9A (1 ug) was transfected with lipofectamine 3000 according to the manufacturer's instructions in Halo-ATG9A cells. 24 hours after transfection cells were imaged by spinning disc confocal microscopy as described above.

Quantification and statistical analysis

Data are expressed as ± one standard deviation (SD) unless otherwise stated. Data presented as percentage were normalized using a logit function prior to statistical analysis. Statistical differences were evaluated by two-tail *t*-test, or one-way ANOVA at $p < 0.05$ significance level followed by Bonferroni post-hoc test. All the statistical analyses were computed using OriginPro (v. 2023, OriginLab).

APPENDIX

Figures 2.10-2.13

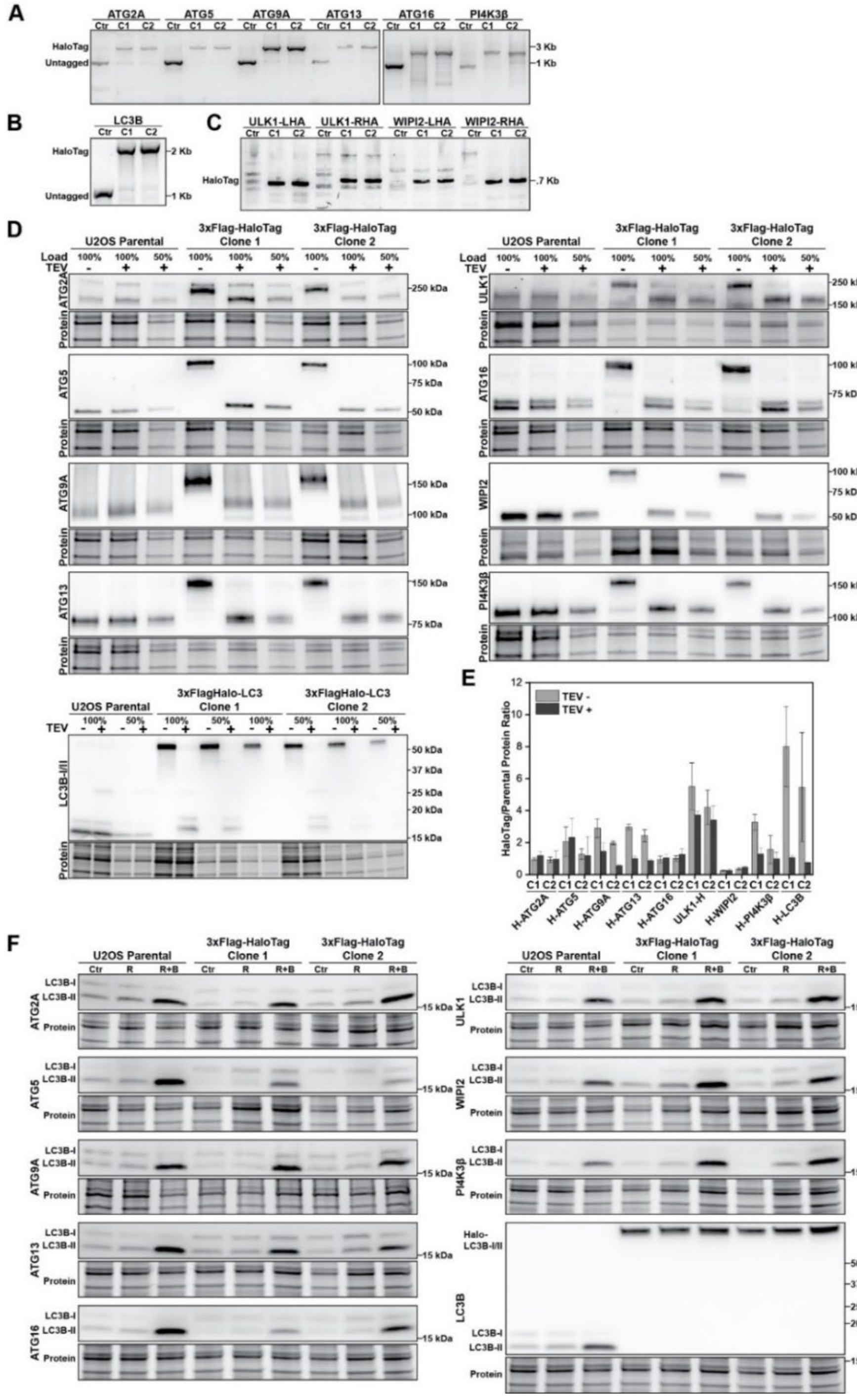

Figure 2.10. Validation and functional characterization of genome-edited clones expressing HaloTagged autophagy factors. (**A-B**) PCR analysis from genomic DNA of genome-edited clones for verifying the correct insertion of the HaloTag at the autophagy

Figure 2.10. (cont'd) loci. For amplifying the insertion, primers outside the homology arms region were designed. The edited clones show an expected shift of ~2kb on the PCR product, corresponding to the 3xFlag-HaloTag insert. D.G.B (**C**) PCR analysis from genomic DNA of genome-edited clones for verifying the correct insertion of the HaloTag in the high GC-rich *ULK1* and *WIPI2* gene loci. For amplifying the insertion, primers outside the homology arms and inside the 3xFlag-HaloTag regions were designed. The edited clones show a PCR product, which is absent in the parental U2OS cell line. D.G.B., C.B. (**D**) Western blots for determining the expression levels of the HaloTagged autophagy proteins relative to the wildtype protein before and after removal of HaloTag using the TEV protease. D.G.B., C.B. (**E**) Quantification of the western blots (A), showing the ratio between HaloTag and parental cell line (N=3, mean ± SD). D.G.B., C.B. (**F**) Western blot analysis of LC3 levels in parental and genome-edited cell lines in control (Ctr) and upon treatment with rapamycin (R, 100nM for 2h), or rapamycin + bafilomycin (R+B, 100nM each, for 2h).

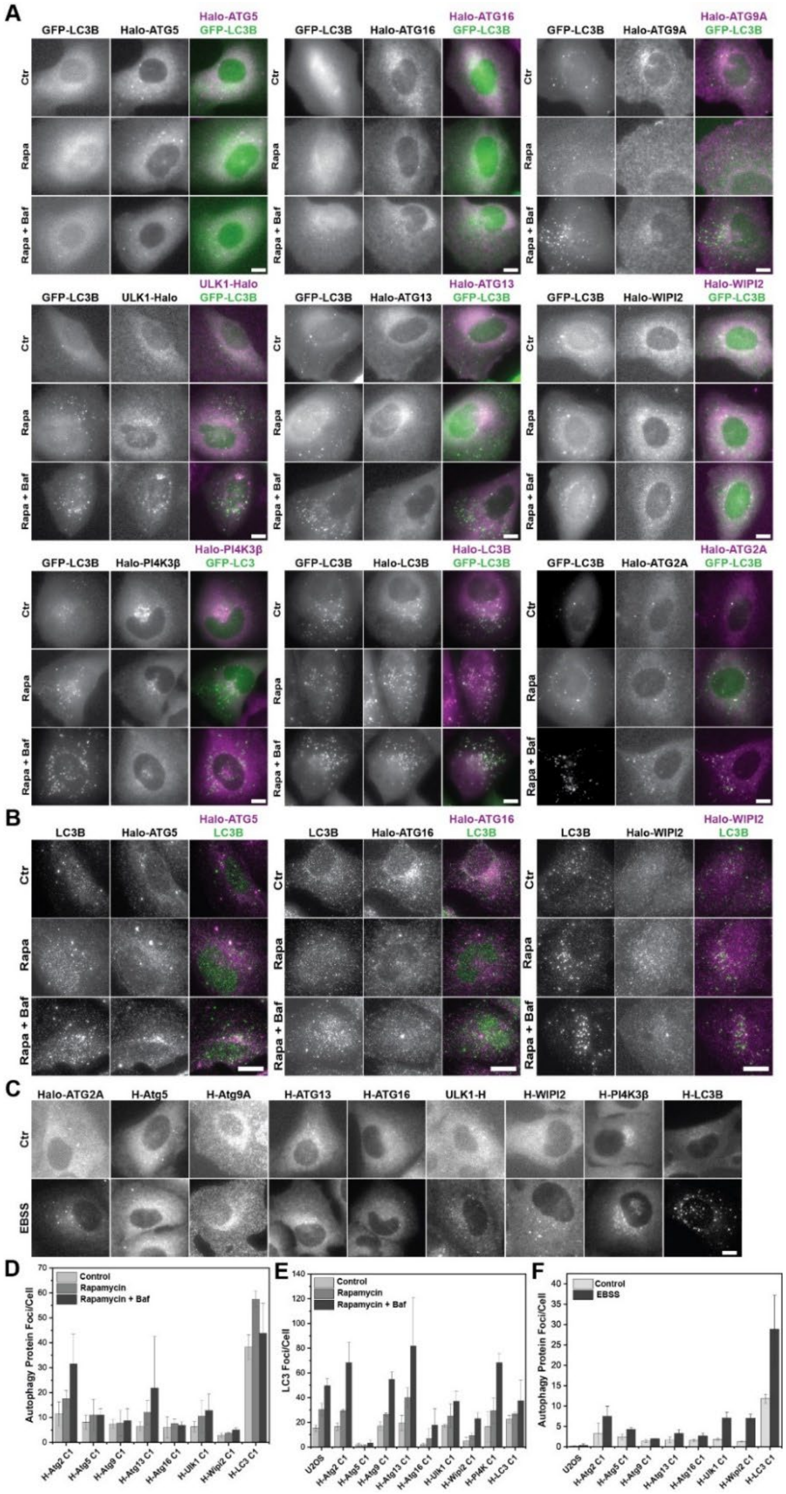

Figure 2.11. Autophagy induced foci formation by HaloTagged autophagy proteins. (**A**) Live-cell imaging of GFP-LC3 and JF646-labeled HaloTagged proteins in control (Ctr) and upon treatment with rapamycin (Rapa, 100nM for 2h), or rapamycin + bafilomycin (Rapa+Baf, 100nM each, for 2h). Both treatments show an expected increase in autophagy and LC3 foci. Scale bar = 10 µm. D.G.B., C.B. (**B**) Immunofluorescence with anti-LC3B antibody and HaloTag JF646-labeling for Halo-ATG5, Halo-ATG16, and Halo-

Figure 2.11. (cont'd) WIPI2 cell lines in control (Ctr) and upon treatment with rapamycin (Rapa, 100nM for 2h), or rapamycin + bafilomycin (Rapa+Baf, 100nM each, for 2h). Both treatments show an expected increase in autophagy and LC3 foci. Scale bar = 10 μm. D.G.B., C.B. (**C**) Representative images of JF646-labeled HaloTagged proteins under control (Ctr) or EBSS starvation media, demonstrating foci-forming ability upon autophagy induction. Scale bar = 10 μm. D.G.B., C.B. (**D**) Quantification of autophagy factor foci from live-cell imaging (A). Data represent the mean ± 1SD of three biological replicates. (**E**) Quantification of LC3 foci from live-cell imaging (A) (N=3, mean ± SD). D.G.B., C.B. (**F**) Quantification of autophagy factor foci from live-cell imaging (C) (N=3, mean ± SD). D.G.B., C.B.

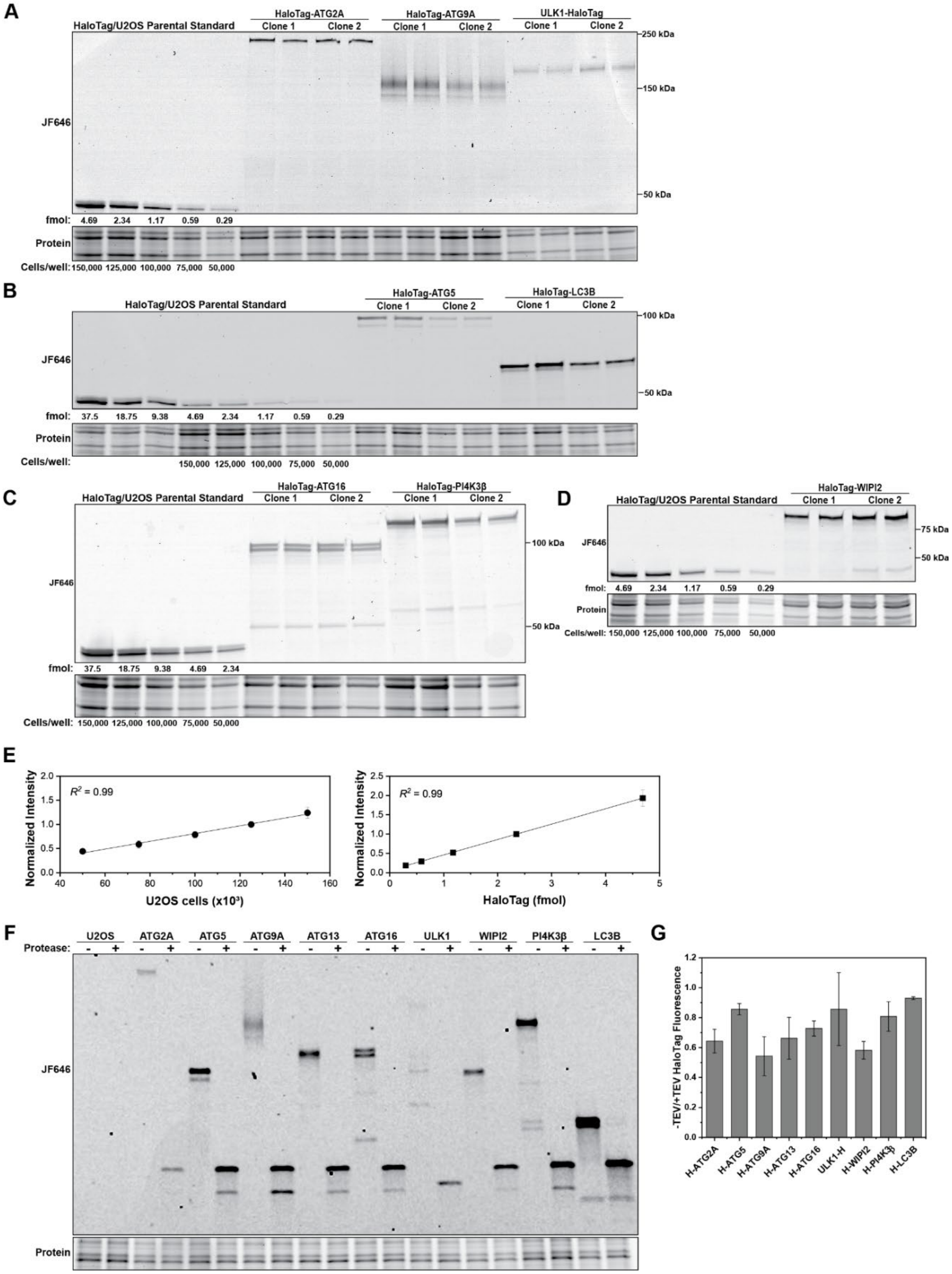

Figure 2.12. Absolute protein abundance quantification of HaloTagged autophagy factors. (**A-D**) Representative fluorescence gels for the absolute quantification of the autophagy proteins. D.G.B., C.B. (**E**) Standard curve for cell number using stain-free

Figure 2.12. (cont'd) gels(top) and florescent HaloTag protein (bottom), demonstrating an excellent correlation between intensity and gel loadings. D.G.B., C.B. (**F**) Representative fluorescence gel of HaloTagged proteins in the absence or presence of TEV protease. D.G.B., C.B. (**G**) Ratio of HaloTag fluorescence in the absence and presence of TEV protease (B) (N=3, mean ± SD). D.G.B., C.B.

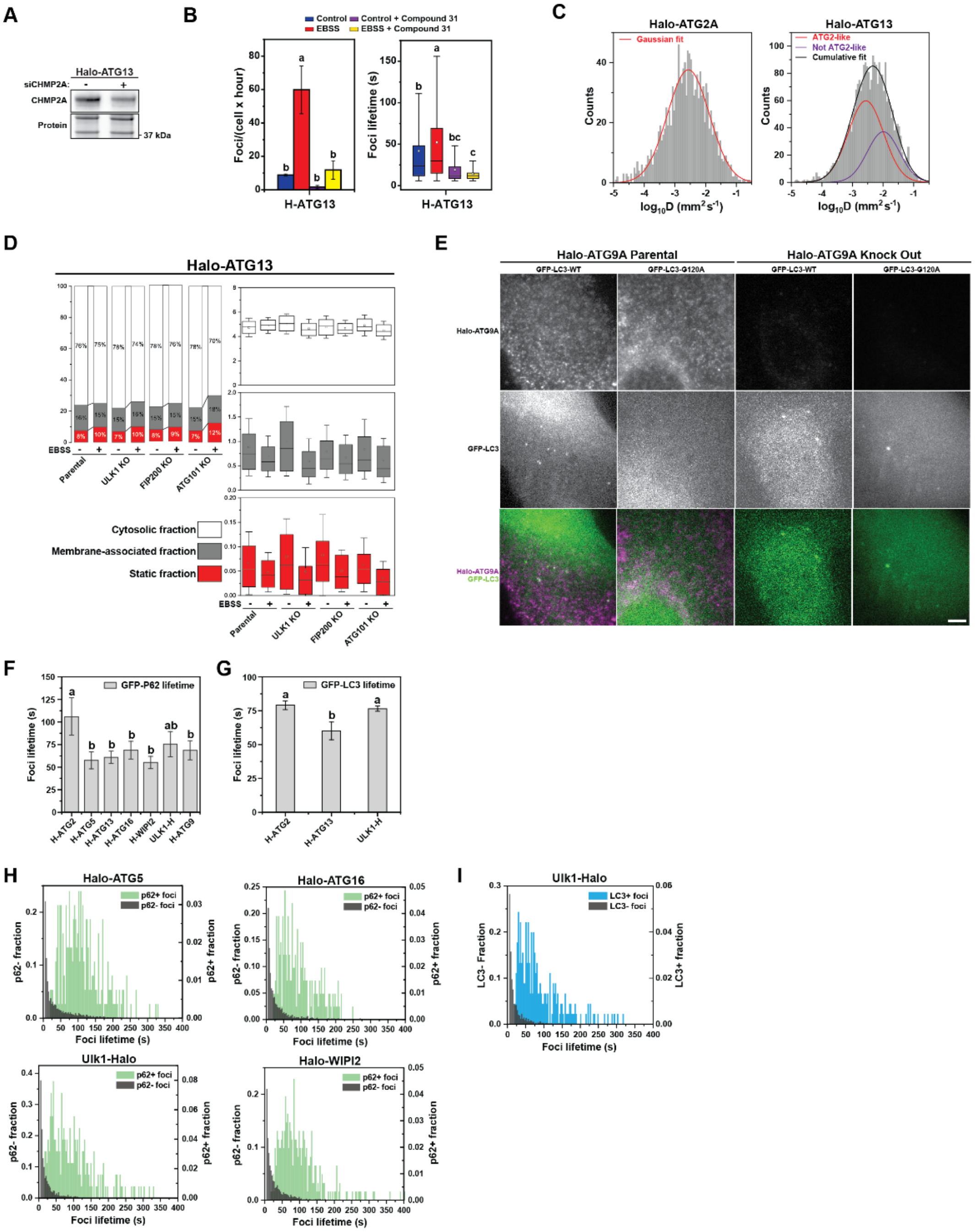

Figure 12.13. Quantification of diffusion and kinetic properties of HaloTagged autophagy proteins and autophagy induced foci. (**A**) Western blot showing partial depletion of CHMP2A in Halo-ATG13 cell line upon siRNA-mediated knock-down. D.G.B., C.B. (**B**) Graphs depicting foci frequency and foci lifetimes of ATG13 in complete media or EBSS treated with VPS34 inhibitor compound 31. Data represent mean ± SD. Letters indicate statistically homogenous groups established by ANOVA ($p < 0.05$). D.G.B., C.B. (**C**) Distribution of diffusion coefficients for Halo-ATG2A and Halo-ATG2A foci imaged a 3s frame interval. In Halo-ATG13, Gaussian fitting shows two populations with distinct diffusive properties (solid green and red lines). Cumulative fitting is shown in a solid black line**.** D.G.B., C.B. (**D**) Results of diffusive analysis for the parental Halo-ATG13 and ULK1,

Figure 12.13. (cont'd) FIP200 and ATG101 knockout under control, and EBSS starvation. Left panel depicts the percentage associated with each fraction. Right panels present the diffusion coefficients of the tracks based on the SpotON analysis. Boxes indicate confidence interval ± SD, the square indicates the average, and the horizontal line is the median; for each condition, 3 biological replicates were analyzed, ~20 cells/replicate. D.G.B., C.B. (**E**) Images demonstrating the titration of the virus such that the G120A mutant does not form aggregates (left) and a positive control in an ATG9A KO (right). D.G.B., C.B. (**F**) Bar graph representing the average lifetime of GFP-P62 within ATG edited cell lines. Data represent mean ± SD of three biological replicates (20-30 cells per replicate). Letters indicate statistically homogenous groups established by ANOVA ($p < 0.05$). D.G.B., C.B. (**G**) Bar graph depicting the average lifetime of GFP-LC3 within ATG edited cell lines. Data represent mean ± SD of three biological replicates (20-30 cells per replicate). Letters indicate statistically homogenous groups established by ANOVA ($p < 0.05$). D.G.B., C.B. (**H**) Histograms of the lifetime of Halo-Tagged protein foci that colocalized (green) or did not colocalize (dark grey) with GFP-P62 or D.G.B., C.B. (**I**) GFP-LC3 (light blue). D.G.B., C.B.

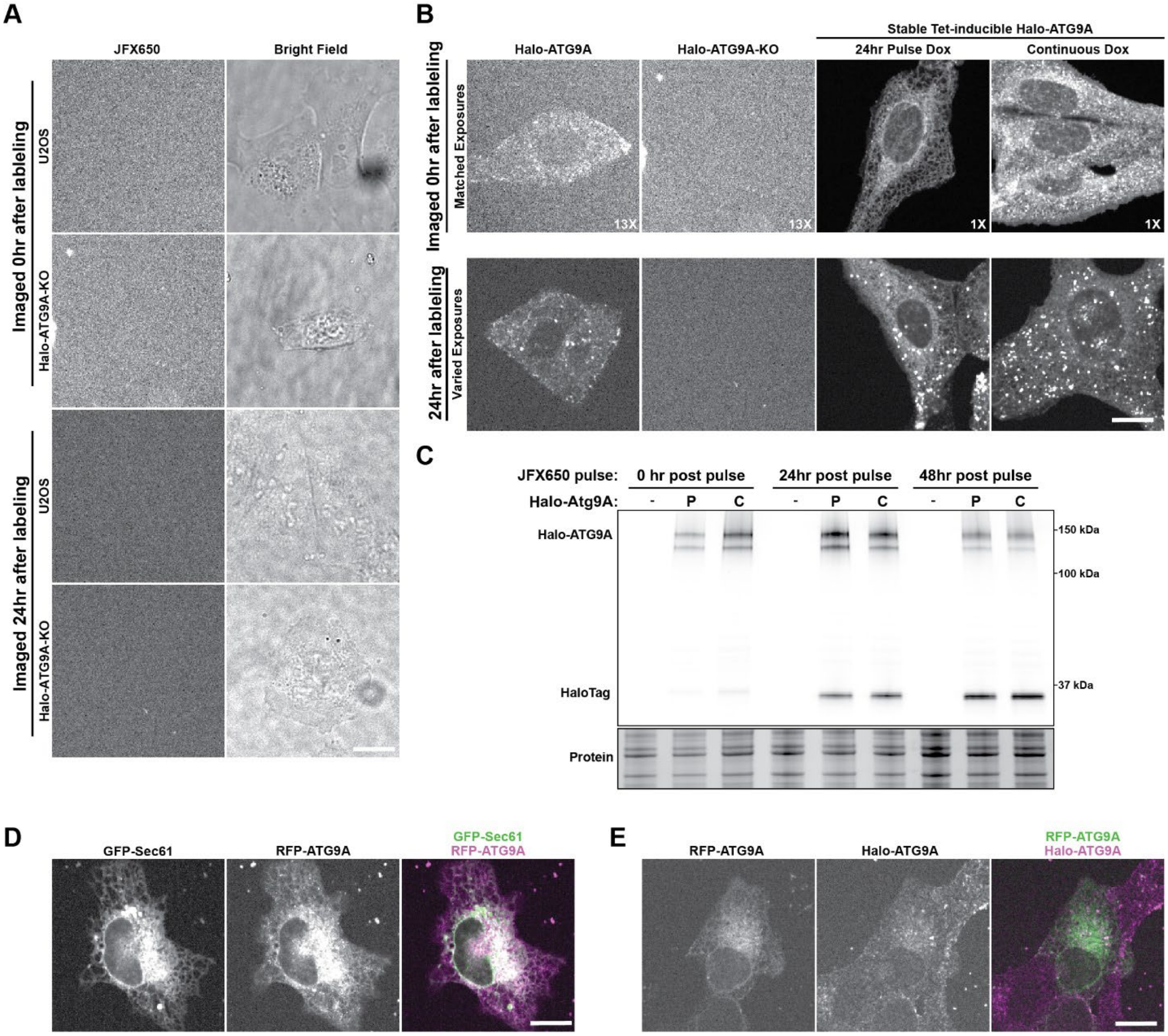

Figure 2.14. Pulse-chase analysis of Halo-ATG9 localization and degradation. (**A**) Representative micrographs of U2OS and Halo-ATG9A KO cells pulse labeled with JFX650 HaloTag-ligand at 0hr and 24h after labeling. Left panel: fluorescence signal; Right panel: bright field. D.G.B.(**B**) Representative micrographs of Halo-ATG9A at 0h (top) and 24h (bottom) labeling in the endogenously edited cell line (left) or in the stable tetracycline-inducible add back at different doxycycline pulse (left). D.G.B. (**C**) Fluorescence gel showing time-dependent cleavage of Halo-ATG9A in cells exposed to a single doxycycline pulse (P) or continuously grown in the presence of doxycycline (C), with progressive accumulation of a lower (~34 kDa) fluorescent band corresponding to the HaloTag protein. D.G.B. (**D**) Representative micrographs showing overlap between the endoplasmic reticulum (marked with GFP-SEC61) and RFP-ATG9A. D.G.B. (**E**) Representative micrographs showing overlap between Halo-ATG9A and transiently expressed RFP-ATG9A.D.G.B.

Supplemental Movie Legends

*Supplemental movies are described below but can be accessed at: https://doi.org/10.1083/jcb.202210078

Movie S1. Representative live-cell single-molecule imaging movies of control and EBSS-treated U2OS cells expressing 3xFLAG-HaloTagged ATG2A labeled with JFX650 and images were acquired at 146 frames per second. 140x140 pixels with a pixel size of 0.16 µm.

Movie S2. Representative live-cell single-molecule imaging movies of control and EBSS-treated U2OS cells expressing 3xFLAG-HaloTagged ATG5 labeled with JFX650 and images were acquired at 146 frames per second. 140x140 pixels with a pixel size of 0.16 µm.

Movie S2. Representative live-cell single-molecule imaging movies of control and EBSS-treated U2OS cells expressing 3xFLAG-HaloTagged ATG9A labeled with JFX650 and images were acquired at 146 frames per second. 140x140 pixels with a pixel size of 0.16 µm.

Movie S4. Representative live-cell single-molecule imaging movies of control and EBSS-treated U2OS cells expressing 3xFLAG-HaloTagged ATG13 labeled with JFX650 and images were acquired at 146 frames per second. 140x140 pixels with a pixel size of 0.16 µm.

Movie S5. Representative live-cell single-molecule imaging movies of control and EBSS-treated U2OS cells expressing 3xFLAG-HaloTagged ATG16 labeled with JFX650 and images were acquired at 146 frames per second. 140x140 pixels with a pixel size of 0.16 µm.

Movie S6. Representative live-cell single-molecule imaging movies of control and EBSS-treated U2OS cells expressing 3xFLAG-HaloTagged ULK1 labeled with JFX650 and images were acquired at 146 frames per second. 140x140 pixels with a pixel size of 0.16 μm.

Movie S7. Representative live-cell single-molecule imaging movies of control and EBSS-treated U2OS cells expressing 3xFLAG-HaloTagged WIPI2 labeled with JFX650 and images were acquired at 146 frames per second. 140x140 pixels with a pixel size of 0.16 μm.

Movie S8. Representative live-cell single-molecule imaging movies of control and EBSS-treated U2OS cells expressing 3xFLAG-HaloTagged LC3B labeled with JFX650 and images were acquired at 146 frames per second. 140x140 pixels with a pixel size of 0.16 μm.

Movie S9. Representative live-cell single-molecule imaging movies of control and EBSS-treated U2OS cells expressing 3xFLAG-HaloTagged PI4K3β labeled with JFX650 and images were acquired at 146 frames per second. 140x140 pixels with a pixel size of 0.16 μm.

Movie S10. Representative live-cell single-molecule imaging movies of control and EBSS-treated U2OS cells expressing 3xFLAG-HaloTagged NES labeled with JFX650 and SNAPTagged SEC61B labeled with JF650 and images were acquired at 146 frames per second. 140x140 pixels with a pixel size of 0.16 μm.

Movie S11. Representative live-cell imaging movies showing the automated foci detection and tracking using TrackIT algorithm. Left: raw movie of Halo-ATG2A cell line in EBSS starvation media; Center: automated identification of foci spots; Right: compiling of tracks. Cells were labeled with JF646 and images were acquired at 4 frames per minute. 300x300 pixels with a pixel size of 0.27 µm.

Movie S12. Representative live-cell foci imaging movies of control and EBSS-treated U2OS cells expressing 3xFLAG-HaloTagged ATG2A labeled with JF646 and images were acquired at 4 frames per minute. 300x300 pixels with a pixel size of 0.27 µm.

Movie S12. Representative live-cell foci imaging movies of control and EBSS-treated U2OS cells expressing 3xFLAG-HaloTagged ATG5 labeled with JF646 and images were acquired at 4 frames per minute. 300x300 pixels with a pixel size of 0.27 µm.

Movie S14. Representative live-cell foci imaging movies of control and EBSS-treated U2OS cells expressing 3xFLAG-HaloTagged ATG9A labeled with JF646 and images were acquired at 4 frames per minute. 300x300 pixels with a pixel size of 0.27 µm.

Movie S15. Representative live-cell foci imaging movies of control and EBSS-treated U2OS cells expressing 3xFLAG-HaloTagged ATG13 labeled with JF646 and images were acquired at 4 frames per minute. 300x300 pixels with a pixel size of 0.27 µm.

Movie S16. Representative live-cell foci imaging movies of control and EBSS-treated U2OS cells expressing 3xFLAG-HaloTagged ATG16 labeled with JF646 and images were acquired at 4 frames per minute. 300x300 pixels with a pixel size of 0.27 µm.

Movie S17. Representative live-cell foci imaging movies of control and EBSS-treated U2OS cells expressing 3xFLAG-HaloTagged ULK1 labeled with JF646 and images were acquired at 4 frames per minute. 300x300 pixels with a pixel size of 0.27 µm.

Movie S18. Representative live-cell foci imaging movies of control and EBSS-treated U2OS cells expressing 3xFLAG-HaloTagged WIPI2 labeled with JF646 and images were acquired at 4 frames per minute. 300x300 pixels with a pixel size of 0.27 µm.

Movie S19. Representative live-cell foci imaging movies of EBSS-treated U2OS cells expressing 3xFLAG-HaloTagged ATG13, and mEmerald-SEC61 treated with control siRNA. Cells were labeled with JFX650 and images were acquired at 1 frame per second. mEmerald-SEC61 signal was reconstructed to higher resolution using the CARE algorithm.

Movie S20. Representative live-cell foci imaging movies of EBSS-treated U2OS cells expressing 3xFLAG-HaloTagged ATG2 and GFP-ATG12. Cells were labeled with JFX650 and images were acquired at 1 frame per second.

Movie S21. Representative live-cell foci imaging movies of EBSS-treated U2OS cells expressing 3xFLAG-HaloTagged ATG13 (top left), and ULK1 (top right), FIP200 (bottom left), and ATG101 (bottom right) knock outs. Cells were labeled with JF646 and acquired at 4 frames per minute. 300x300 pixels with a pixel size of 0.27 μm.

Movie S22. Representative live-cell foci imaging movies of control and EBSS-treated U2OS cells expressing 3xFLAG-HaloTagged ATG13 with and without wortmannin. Cells were labeled with JF646 and images were acquired at 4 frames per minute. 300x300 pixels with a pixel size of 0.27 μm.

Movie S22. Representative live-cell foci imaging movies of control and EBSS-treated U2OS cells expressing 3xFLAG-HaloTagged ATG2 with and without wortmannin. Cells were labeled with JF646 and images were acquired at 4 frames per minute. 300x300 pixels with a pixel size of 0.27 μm.

Movie S24. Representative live-cell single-molecule imaging movies of control (top) and EBSS-treated (bottom) U2OS cells expressing 3xFLAG-HaloTagged ATG13 parental and and ULK1, FIP200, and ATG101 knock out. Cells were labeled with JF650 and images were acquired at 146 frames per second. 140x140 pixels with a pixel size of 0.16 μm.

Movie S25. Representative live-cell foci imaging movies of EBSS-treated U2OS cells expressing 3xFLAG-HaloTagged LC3 labeled with JF646 and GFP-P62. Images were acquired at 20 frames per minute. 300x300 pixels with a pixel size of 0.27 μm.

Movie S26. Representative live-cell foci imaging movies of EBSS-treated U2OS cells expressing 3xFLAG-HaloTagged ATG2A labeled with JF646 and GFP-P62. Images were acquired at 20 frames per minute. 300x300 pixels with a pixel size of 0.27 μm.

Movie S27. Representative live-cell foci imaging movies of EBSS-treated U2OS cells expressing 3xFLAG-HaloTagged ATG5 labeled with JF646 and GFP-P62. Images were acquired at 20 frames per minute. 300x300 pixels with a pixel size of 0.27 μm.

Movie S28. Representative live-cell foci imaging movies of EBSS-treated U2OS cells expressing 3xFLAG-HaloTagged ATG9A labeled with JF646 and GFP-P62. Images were acquired at 20 frames per minute. 300x300 pixels with a pixel size of 0.27 μm.

Movie S29. Representative live-cell foci imaging movies of EBSS-treated U2OS cells expressing 3xFLAG-HaloTagged ATG13 labeled with JF646 and GFP-P62. Images were acquired at 20 frames per minute. 300x300 pixels with a pixel size of 0.27 μm.

Movie S30. Representative live-cell foci imaging movies of EBSS-treated U2OS cells expressing 3xFLAG-HaloTagged ATG16 labeled with JF646 and GFP-P62. Images were acquired at 20 frames per minute. 300x300 pixels with a pixel size of 0.27 μm.

Movie S31. Representative live-cell foci imaging movies of EBSS-treated U2OS cells expressing 3xFLAG-HaloTagged ULK1 labeled with JF646 and GFP-P62. Images were acquired at 20 frames per minute. 300x300 pixels with a pixel size of 0.27 μm.

Movie S32. Representative live-cell foci imaging movies of EBSS-treated U2OS cells expressing 3xFLAG-HaloTagged WIPI2 labeled with JF646 and GFP-P62. Images were acquired at 20 frames per minute. 300x300 pixels with a pixel size of 0.27 µm.

Movie S32. Representative live-cell foci imaging movies of EBSS-treated U2OS cells expressing 3xFLAG-HaloTagged ATG2A labeled with JF646 and GFP-LC2. Images were acquired at 20 frames per minute. 300x300 pixels with a pixel size of 0.27 µm.

Movie S34. Representative live-cell foci imaging movies of EBSS-treated U2OS cells expressing 3xFLAG-HaloTagged ATG13 labeled with JF646 and GFP-LC2. Images were acquired at 20 frames per minute. 300x300 pixels with a pixel size of 0.27 µm.

Movie S35. Representative live-cell foci imaging movies of EBSS-treated U2OS cells expressing 3xFLAG-HaloTagged ULK1 labeled with JF646 and GFP-LC2. Images were acquired at 20 frames per minute. 300x300 pixels with a pixel size of 0.27 µm.

Movie S36. Representative live-cell foci imaging movies of EBSS-treated U2OS cells expressing 3xFLAG-HaloTagged ATG9A and SNAPtag-LC3B. Cells were labeled with JFX650 HaloTag ligand and JF503 SNAPtag ligand and images were acquired at 1 frame per second.

Movie S37. Representative live-cell foci imaging movies of EBSS-treated U2OS cells expressing 3xFLAG-HaloTagged ATG2 (left), 3xFLAG-HaloTagged ATG2 ATG9A knock-out (right). Cells were labeled with JF646 HaloLigand and images were acquired at 4 frames per minute. 300x300 pixels with a pixel size of 0.27 µm.

Movie S38. Representative live-cell foci imaging movies of EBSS-treated U2OS cells expressing 3xFLAG-HaloTagged ATG9A, RFP-ATG9A, and LAMP-mNeonGreen. Cells were labeled with JFX650 HaloTag ligand and images were acquired at 1 frame per second. (Green: Halo-ATG9A Red: RFP-ATG9A Blue: Lamp1-mNeon)

Movie S39. Representative live-cell foci imaging movies of EBSS-treated U2OS cells expressing 3xFLAG-HaloTagged ATG9A, SNAPtag-LC3B, and treated with LysoTracker DeepRed. Cells were labeled with JFX554 HaloTag ligand and JF503 SNAPtag ligand and images were acquired at 1 frame per second. (Green: Halo-ATG9A Red: SNAP-LC3B Blue: Lysotracker)

CHAPTER 3: KEY FINDINGS AND FUTURE DIRECTIONS

Key findings

The complexity of the autophagic pathway has continued to expand since the initial characterization of non-selective autophagy in yeast. Macroautophagy has since been expanded to include a wide variety of subsets including non-selective, mitophagy, aggrephagy, ER-phagy, and potentially the recently identified endo-phagy. Additionally, macroautophagy has an interconnected and complex relationship with the endosomal-lysosome system and cellular motors. In cells, all of these occur simultaneously resulting in a complex and dynamic process that conventional microscopy and analysis cannot capture.

In Chapter 2, I presented endogenously HaloTagged autophagy factors. We characterize the functionality of these factors and demonstrate them to be robust tools for studying non-selective autophagy. We demonstrate that the majority of ATG13 cannot be constitutively bound to ULK1, due to the ~9 fold difference in absolute protein abundance. High-throughput analysis of endogenously tagged autophagy foci demonstrates 2-3-fold faster kinetics compared to other studies. Using the principles defined in K-FOCUS we perform dual-channel tracking and identify a novel brief (<30 seconds) autophagy foci, that represent the majority of foci, and don't culminate in autophagosomes. Diffusion coefficient analysis identifies two populations of ATG foci, while ATG2 only represented a slower population. We posit that the faster population represents the accumulation of autophagy factors on ATG9A vesicles that dissociate, aborting the autophagosome. Using the same time threshold for the short foci, we find that ATG2 foci negative for ATG13 are also short, and dual positive foci are long lasting, indicating that ATG2/ATG13 positive foci likely represent committed autophagosomes. Importantly, knockout of ATG9 abolished both the short and long ATG2 foci, further suggesting that it represents that platform for autophagosome biogenesis. Our work is the first to provide evidence for the vesicle seeding of autophagosomes using live-cell data. Additionally, we rectify discrepancies surrounding ATG9A localization to redefine the role of ATG9A at the autophagosome and show the endpoint accumulation of ATG9A is within the lysosome.

Future Directions

Many of the well-characterized observations made within chapter 2 are completely novel to the autophagy field. However, they are not of equal importance. In my opinion the two most impactful observations in this work, and those that will be discussed in this section, is that the majority of autophagosomes are aborted and that ATG9A is not detectable at autophagosomes but accumulates in the lysosome over time.

Aborted autophagosomes is a completely novel concept for the autophagy field, and further work to better characterize these structures is warranted. Their presence also begs the question, “What signals determine if an autophagosome will continue on to be conjugated with ATG8 family members?”. Another important question is, “Do aborted autophagosomes occur in neurons, or in multi-cellular organisms?”. Answering these questions will play an important part in truly understanding the significance of this intriguing finding. Our data also questions whether ATG foci that are negative for ATG8 family members should be considered autophagosomes in colocalization studies.

The second major finding of ATG9A at the lysosome has also never been identified. ATG9A has been an elusive protein to study within the autophagy field. Few labs have attempted live-cell imaging on ATG9A and those that have, usually use the RFP-tagged version. Our work clarifies much of the confusion surrounding the role of

ATG9A at the autophagosome and provides live-cell data that is not in contradiction with the newest cryo-EM structures. Understanding the path of ATG9A from the ER-Golgi-vesicle-lysosome pathways substantially impacts past and future studies. Most obvious is that ATG9A does not form foci, and protease resistant fused tags localize to the lysosome. This finding also extends to untagged ATG9A, which may accumulate in lysosomes in conditions that effect autophagosome-lysosome fusion events, and ultimately confound conclusions from colocalizing ATG9A with other proteins. This work highlights the many potential pitfalls when imaging ATG9A, but does raise an intriguing question, “Does ATG9A play a role in the function of lysosomes?”. My work demonstrates that ATG9A is degraded in the lysosome, but due to multi-vesicular bodies that specifically function to degrade membrane proteins, it is possible that ATG9A may be at the lysosome for another purpose. One can speculate that a scramblase at a lysosome may be beneficial to maintain a homeostatic membrane that can continue to fuse with incoming endosomes or autophagosomes. Further work is required to verify its role. If ATG9 does not play a role at the lysosome, but arrives through its role in autophagosome biogenesis, then Halo-ATG9A accumulation in the lysosome has the potential to be a readout of early autophagosome biogenesis. All current autophagosome markers are visible at the ATG8 family member conjugation step and does not provide insight into the amount of conjugation per autophagosome, total number of autophagosomes, or the size of autophagosomes. Thus, determining if ATG9A can be used as a readout for total formed autophagosomes would provide an impactful new tool for the autophagy field.

REFERENCES

Bakula, D., A.J. Müller, T. Zuleger, Z. Takacs, M. Franz-Wachtel, A.K. Thost, D. Brigger, M.P. Tschan, T. Frickey, H. Robenek, B. Macek, and T. Proikas-Cezanne. 2017. WIPI3 and WIPI4 β-propellers are scaffolds for LKB1-AMPK-TSC signalling circuits in the control of autophagy. *Nat Commun*. 8:15637.

Barth, S., D. Glick, and K.F. Macleod. 2010. Autophagy: assays and artifacts. *J Pathol*. 221:117-124.

Berg, T.O., M. Fengsrud, P.E. Strømhaug, T. Berg, and P.O. Seglen. 1998. Isolation and characterization of rat liver amphisomes. Evidence for fusion of autophagosomes with both early and late endosomes. *J Biol Chem*. 273:21883-21892.

Blommaart, E.F., U. Krause, J.P. Schellens, H. Vreeling-Sindelárová, and A.J. Meijer. 1997. The phosphatidylinositol 3-kinase inhibitors wortmannin and LY294002 inhibit autophagy in isolated rat hepatocytes. *Eur J Biochem*. 243:240-246.

Bright, N.A., M.J. Gratian, and J.P. Luzio. 2005. Endocytic delivery to lysosomes mediated by concurrent fusion and kissing events in living cells. *Curr Biol*. 15:360-365.

Cattoglio, C., I. Pustova, N. Walther, J.J. Ho, M. Hantsche-Grininger, C.J. Inouye, M.J. Hossain, G.M. Dailey, J. Ellenberg, X. Darzacq, R. Tjian, and A.S. Hansen. 2019. Determining cellular CTCF and cohesin abundances to constrain 3D genome models. *Elife*. 8.

Chang, C., L.E. Jensen, and J.H. Hurley. 2021a. Autophagosome biogenesis comes out of the black box. *Nat Cell Biol*. 23:450-456.

Chang, C., X. Shi, L.E. Jensen, A.L. Yokom, D. Fracchiolla, S. Martens, and J.H. Hurley. 2021b. Reconstitution of cargo-induced LC3 lipidation in mammalian selective autophagy. *Sci Adv*. 7.

Chertkova, A.O., M. Mastop, M. Postma, N. van Bommel, S. van der Niet, K.L. Batenburg, L. Joosen, T.W.J. Gadella, Y. Okada, and J. Goedhart. 2017. Robust and Bright Genetically Encoded Fluorescent Markers for Highlighting Structures and Compartments in Mammalian Cells. *bioRxiv*:160374.

Chowdhury, S., C. Otomo, A. Leitner, K. Ohashi, R. Aebersold, G.C. Lander, and T. Otomo. 2018. Insights into autophagosome biogenesis from structural and biochemical analyses of the ATG2A-WIPI4 complex. *Proc Natl Acad Sci U S A*. 115:E9792-E9801.

Cong, L., F.A. Ran, D. Cox, S. Lin, R. Barretto, N. Habib, P.D. Hsu, X. Wu, W. Jiang, L.A. Marraffini, and F. Zhang. 2013. Multiplex genome engineering using CRISPR/Cas systems. *Science*. 339:819-823.

Dalle Pezze, P., E. Karanasios, V. Kandia, M. Manifava, S.A. Walker, N. Gambardella Le Novère, and N.T. Ktistakis. 2021. ATG13 dynamics in nonselective autophagy and mitophagy: insights from live imaging studies and mathematical modeling. *Autophagy*. 17:1131-1141.

de Chaumont, F., S. Dallongeville, N. Chenouard, N. Hervé, S. Pop, T. Provoost, V. Meas-Yedid, P. Pankajakshan, T. Lecomte, Y. Le Montagner, T. Lagache, A. Dufour, and J.C. Olivo-Marin. 2012. Icy: an open bioimage informatics platform for extended reproducible research. *Nat Methods*. 9:690-696.

Dikic, I., and Z. Elazar. 2018. Mechanism and medical implications of mammalian autophagy. *Nat Rev Mol Cell Biol*. 19:349-364.

Dooley, H.C., M. Razi, H.E. Polson, S.E. Girardin, M.I. Wilson, and S.A. Tooze. 2014. WIPI2 links LC3 conjugation with PI3P, autophagosome formation, and pathogen clearance by recruiting Atg12-5-16L1. *Mol Cell*. 55:238-252.

Dorsey, F.C., K.L. Rose, S. Coenen, S.M. Prater, V. Cavett, J.L. Cleveland, and J. Caldwell-Busby. 2009. Mapping the phosphorylation sites of Ulk1. *J Proteome Res*. 8:5253-5263.

Feng, Y., D. He, Z. Yao, and D.J. Klionsky. 2014. The machinery of macroautophagy. *Cell Res*. 24:24-41.

Filimonenko, M., S. Stuffers, C. Raiborg, A. Yamamoto, L. Malerød, E.M. Fisher, A. Isaacs, A. Brech, H. Stenmark, and A. Simonsen. 2007. Functional multivesicular bodies are required for autophagic clearance of protein aggregates associated with neurodegenerative disease. *J Cell Biol*. 179:485-500.

Filippone, A., E. Esposito, D. Mannino, N. Lyssenko, and D. Praticò. 2022. The contribution of altered neuronal autophagy to neurodegeneration. *Pharmacol Ther*. 238:108178.

Foglio, E., G. Puddighinu, A. Germani, M.A. Russo, and F. Limana. 2017. HMGB1 Inhibits Apoptosis Following MI and Induces Autophagy via mTORC1 Inhibition. *J Cell Physiol*. 232:1135-1143.

Fracchiolla, D., C. Chang, J.H. Hurley, and S. Martens. 2020. A PI3K-WIPI2 positive feedback loop allosterically activates LC3 lipidation in autophagy. *J Cell Biol*. 219.

Fujita, N., M. Hayashi-Nishino, H. Fukumoto, H. Omori, A. Yamamoto, T. Noda, and T. Yoshimori. 2008. An Atg4B mutant hampers the lipidation of LC3 paralogues and causes defects in autophagosome closure. *Mol Biol Cell*. 19:4651-4659.

Ganley, I.G., d.H. Lam, J. Wang, X. Ding, S. Chen, and X. Jiang. 2009. ULK1.ATG13.FIP200 complex mediates mTOR signaling and is essential for autophagy. *J Biol Chem*. 284:12297-12305.

Ge, L., M. Zhang, S.J. Kenny, D. Liu, M. Maeda, K. Saito, A. Mathur, K. Xu, and R. Schekman. 2017. Remodeling of ER-exit sites initiates a membrane supply pathway for autophagosome biogenesis. *EMBO Rep*. 18:1586-1603.

Gewirtz, D.A. 2014. The four faces of autophagy: implications for cancer therapy. *Cancer Res*. 74:647-651.

Ghanbarpour, A., D.P. Valverde, T.J. Melia, and K.M. Reinisch. 2021. A model for a partnership of lipid transfer proteins and scramblases in membrane expansion and organelle biogenesis. *Proc Natl Acad Sci U S A*. 118.

Grimm, J.B., B.P. English, J. Chen, J.P. Slaughter, Z. Zhang, A. Revyakin, R. Patel, J.J. Macklin, D. Normanno, R.H. Singer, T. Lionnet, and L.D. Lavis. 2015. A general method to improve fluorophores for live-cell and single-molecule microscopy. *Nat Methods*. 12:244-250, 243 p following 250.

Grimm, J.B., B.P. English, H. Choi, A.K. Muthusamy, B.P. Mehl, P. Dong, T.A. Brown, J. Lippincott-Schwartz, Z. Liu, T. Lionnet, and L.D. Lavis. 2016. Bright photoactivatable fluorophores for single-molecule imaging. *Nat Methods*. 13:985-988.

Grimm, J.B., A.K. Muthusamy, Y. Liang, T.A. Brown, W.C. Lemon, R. Patel, R. Lu, J.J. Macklin, P.J. Keller, N. Ji, and L.D. Lavis. 2017. A general method to fine-tune fluorophores for live-cell and in vivo imaging. *Nat Methods*. 14:987-994.

Grimm, J.B., L. Xie, J.C. Casler, R. Patel, A.N. Tkachuk, N. Falco, H. Choi, J. Lippincott-Schwartz, T.A. Brown, B.S. Glick, Z. Liu, and L.D. Lavis. 2021. A General Method to Improve Fluorophores Using Deuterated Auxochromes. *JACS Au*. 1:690-696.

Gross, A.S., and M. Graef. 2020. Mechanisms of Autophagy in Metabolic Stress Response. *J Mol Biol*. 432:28-52.

Guardia, C.M., X.F. Tan, T. Lian, M.S. Rana, W. Zhou, E.T. Christenson, A.J. Lowry, J.D. Faraldo-Gómez, J.S. Bonifacino, J. Jiang, and A. Banerjee. 2020. Structure of

Human ATG9A, the Only Transmembrane Protein of the Core Autophagy Machinery. *Cell Rep*. 31:107837.

Gubas, A., and I. Dikic. 2022. A guide to the regulation of selective autophagy receptors. *FEBS J*. 289:75-89.

Guo, J.Y., X. Teng, S.V. Laddha, S. Ma, S.C. Van Nostrand, Y. Yang, S. Khor, C.S. Chan, J.D. Rabinowitz, and E. White. 2016. Autophagy provides metabolic substrates to maintain energy charge and nucleotide pools in Ras-driven lung cancer cells. *Genes Dev*. 30:1704-1717.

Gómez-Sánchez, R., J. Rose, R. Guimarães, M. Mari, D. Papinski, E. Rieter, W.J. Geerts, R. Hardenberg, C. Kraft, C. Ungermann, and F. Reggiori. 2018. Atg9 establishes Atg2-dependent contact sites between the endoplasmic reticulum and phagophores. *J Cell Biol*. 217:2743-2763.

Hanada, T., N.N. Noda, Y. Satomi, Y. Ichimura, Y. Fujioka, T. Takao, F. Inagaki, and Y. Ohsumi. 2007. The Atg12-Atg5 conjugate has a novel E3-like activity for protein lipidation in autophagy. *J Biol Chem*. 282:37298-37302.

Hansen, A.S., M. Woringer, J.B. Grimm, L.D. Lavis, R. Tjian, and X. Darzacq. 2018. Robust model-based analysis of single-particle tracking experiments with Spot-On. *Elife*. 7.

Hayashi-Nishino, M., N. Fujita, T. Noda, A. Yamaguchi, T. Yoshimori, and A. Yamamoto. 2009. A subdomain of the endoplasmic reticulum forms a cradle for autophagosome formation. *Nat Cell Biol*. 11:1433-1437.

Hemelaar, J., V.S. Lelyveld, B.M. Kessler, and H.L. Ploegh. 2003. A single protease, Apg4B, is specific for the autophagy-related ubiquitin-like proteins GATE-16, MAP1-LC3, GABARAP, and Apg8L. *J Biol Chem*. 278:51841-51850.

Henriques, R. 2022. Open Technologies for Super-Resolution & Machine Learning in BioImaging. Vol. 2023.

Hosokawa, N., T. Hara, T. Kaizuka, C. Kishi, A. Takamura, Y. Miura, S. Iemura, T. Natsume, K. Takehana, N. Yamada, J.L. Guan, N. Oshiro, and N. Mizushima. 2009. Nutrient-dependent mTORC1 association with the ULK1-Atg13-FIP200 complex required for autophagy. *Mol Biol Cell*. 20:1981-1991.

Ichimura, Y., T. Kirisako, T. Takao, Y. Satomi, Y. Shimonishi, N. Ishihara, N. Mizushima, I. Tanida, E. Kominami, M. Ohsumi, T. Noda, and Y. Ohsumi. 2000. A ubiquitin-like system mediates protein lipidation. *Nature*. 408:488-492.

Ichimura, Y., T. Kumanomidou, Y.S. Sou, T. Mizushima, J. Ezaki, T. Ueno, E. Kominami, T. Yamane, K. Tanaka, and M. Komatsu. 2008. Structural basis for sorting mechanism of p62 in selective autophagy. *J Biol Chem*. 283:22847-22857.

Itakura, E., and N. Mizushima. 2010. Characterization of autophagosome formation site by a hierarchical analysis of mammalian Atg proteins. *Autophagy*. 6:764-776.

Jahreiss, L., F.M. Menzies, and D.C. Rubinsztein. 2008. The itinerary of autophagosomes: from peripheral formation to kiss-and-run fusion with lysosomes. *Traffic*. 9:574-587.

Johansen, T., and T. Lamark. 2011. Selective autophagy mediated by autophagic adapter proteins. *Autophagy*. 7:279-296.

Johansen, T., and T. Lamark. 2020. Selective Autophagy: ATG8 Family Proteins, LIR Motifs and Cargo Receptors. *J Mol Biol*. 432:80-103.

Judith, D., H.B.J. Jefferies, S. Boeing, D. Frith, A.P. Snijders, and S.A. Tooze. 2019. ATG9A shapes the forming autophagosome through Arfaptin 2 and phosphatidylinositol 4-kinase IIIβ. *J Cell Biol*. 218:1634-1652.

Juillerat, A., T. Gronemeyer, A. Keppler, S. Gendreizig, H. Pick, H. Vogel, and K. Johnsson. 2003. Directed evolution of O6-alkylguanine-DNA alkyltransferase for efficient labeling of fusion proteins with small molecules in vivo. *Chem Biol*. 10:313-317.

Jung, C.H., C.B. Jun, S.H. Ro, Y.M. Kim, N.M. Otto, J. Cao, M. Kundu, and D.H. Kim. 2009. ULK-Atg13-FIP200 complexes mediate mTOR signaling to the autophagy machinery. *Mol Biol Cell*. 20:1992-2003.

Kabeya, Y., N. Mizushima, T. Ueno, A. Yamamoto, T. Kirisako, T. Noda, E. Kominami, Y. Ohsumi, and T. Yoshimori. 2000. LC3, a mammalian homologue of yeast Apg8p, is localized in autophagosome membranes after processing. *EMBO J*. 19:5720-5728.

Kabeya, Y., N. Mizushima, A. Yamamoto, S. Oshitani-Okamoto, Y. Ohsumi, and T. Yoshimori. 2004. LC3, GABARAP and GATE16 localize to autophagosomal membrane depending on form-II formation. *J Cell Sci*. 117:2805-2812.

Kaizuka, T., H. Morishita, Y. Hama, S. Tsukamoto, T. Matsui, Y. Toyota, A. Kodama, T. Ishihara, T. Mizushima, and N. Mizushima. 2016. An Autophagic Flux Probe that Releases an Internal Control. *Mol Cell*. 64:835-849.

Kannangara, A.R., D.M. Poole, C.M. McEwan, J.C. Youngs, V.K. Weerasekara, A.M. Thornock, M.T. Lazaro, E.R. Balasooriya, L.M. Oh, E.J. Soderblom, J.J. Lee, D.L. Simmons, and J.L. Andersen. 2021. BioID reveals an ATG9A interaction with ATG13-ATG101 in the degradation of p62/SQSTM1-ubiquitin clusters. *EMBO Rep*. 22:e51136.

Karanasios, E., E. Stapleton, M. Manifava, T. Kaizuka, N. Mizushima, S.A. Walker, and N.T. Ktistakis. 2013a. Dynamic association of the ULK1 complex with omegasomes during autophagy induction. *J Cell Sci*. 126:5224-5238.

Karanasios, E., E. Stapleton, S.A. Walker, M. Manifava, and N.T. Ktistakis. 2013b. Live cell imaging of early autophagy events: omegasomes and beyond. *J Vis Exp*.

Karanasios, E., S. Walker, H. Okkenhaug, M. Manifava, E. Hummel, H. Zimmermann, Q. Ahmed, M. Domart, L. Collinson, and N. Ktistakis. 2016. Autophagy initiation by ULK complex assembly on ER tubulovesicular regions marked by ATG9 vesicles. *Nature Communications*. 7.

Khandia, R., M. Dadar, A. Munjal, K. Dhama, K. Karthik, R. Tiwari, M.I. Yatoo, H.M.N. Iqbal, K.P. Singh, S.K. Joshi, and W. Chaicumpa. 2019. A Comprehensive Review of Autophagy and Its Various Roles in Infectious, Non-Infectious, and Lifestyle Diseases: Current Knowledge and Prospects for Disease Prevention, Novel Drug Design, and Therapy. *Cells*. 8.

Kirisako, T., M. Baba, N. Ishihara, K. Miyazawa, M. Ohsumi, T. Yoshimori, T. Noda, and Y. Ohsumi. 1999. Formation process of autophagosome is traced with Apg8/Aut7p in yeast. *J Cell Biol*. 147:435-446.

Kirisako, T., Y. Ichimura, H. Okada, Y. Kabeya, N. Mizushima, T. Yoshimori, M. Ohsumi, T. Takao, T. Noda, and Y. Ohsumi. 2000. The reversible modification regulates the membrane-binding state of Apg8/Aut7 essential for autophagy and the cytoplasm to vacuole targeting pathway. *J Cell Biol*. 151:263-276.

Kirkin, V. 2020. History of the Selective Autophagy Research: How Did It Begin and Where Does It Stand Today? *J Mol Biol*. 432:3-27.

Kirkin, V., and V.V. Rogov. 2019. A Diversity of Selective Autophagy Receptors Determines the Specificity of the Autophagy Pathway. *Mol Cell*. 76:268-285.

Koyama-Honda, I., E. Itakura, T.K. Fujiwara, and N. Mizushima. 2013. Temporal analysis of recruitment of mammalian ATG proteins to the autophagosome formation site. *Autophagy*. 9:1491-1499.

Kuhn, T., J. Hettich, R. Davtyan, and J.C.M. Gebhardt. 2021. Single molecule tracking and analysis framework including theory-predicted parameter settings. *Sci Rep*. 11:9465.

Lamark, T., S. Svenning, and T. Johansen. 2017. Regulation of selective autophagy: the p62/SQSTM1 paradigm. *Essays Biochem*. 61:609-624.

Lamb, C.A., T. Yoshimori, and S.A. Tooze. 2013. The autophagosome: origins unknown, biogenesis complex. *Nat Rev Mol Cell Biol*. 14:759-774.

Lambert, T.J. 2019. FPbase: a community-editable fluorescent protein database. *Nat Methods*. 16:277-278.

Lee, J.A., A. Beigneux, S.T. Ahmad, S.G. Young, and F.B. Gao. 2007. ESCRT-III dysfunction causes autophagosome accumulation and neurodegeneration. *Curr Biol*. 17:1561-1567.

Levy, J.M.M., C.G. Towers, and A. Thorburn. 2017. Targeting autophagy in cancer. *Nat Rev Cancer*. 17:528-542.

Li, Q., Q.T. Dong, Y.J. Yang, X.Q. Tian, C. Jin, P.S. Huang, L.P. Jiang, and G.H. Chen. 2016. AMPK-mediated cardioprotection of atorvastatin relates to the reduction of apoptosis and activation of autophagy in infarcted rat hearts. *Am J Transl Res*. 8:4160-4171.

Lin, M.G., and J.H. Hurley. 2016. Structure and function of the ULK1 complex in autophagy. *Curr Opin Cell Biol*. 39:61-68.

Los, G.V., L.P. Encell, M.G. McDougall, D.D. Hartzell, N. Karassina, C. Zimprich, M.G. Wood, R. Learish, R.F. Ohana, M. Urh, D. Simpson, J. Mendez, K. Zimmerman, P. Otto, G. Vidugiris, J. Zhu, A. Darzins, D.H. Klaubert, R.F. Bulleit, and K.V. Wood. 2008. HaloTag: a novel protein labeling technology for cell imaging and protein analysis. *ACS Chem Biol*. 3:373-382.

Los, G.V., and K. Wood. 2007. The HaloTag: a novel technology for cell imaging and protein analysis. *Methods Mol Biol*. 356:195-208.

Lu, J., M. Wu, and Z. Yue. 2020. Autophagy and Parkinson's Disease. *Adv Exp Med Biol*. 1207:21-51.

Lu, J., L. Zhu, L.P. Zheng, Q. Cui, H.H. Zhu, H. Zhao, Z.J. Shen, H.Y. Dong, S.S. Chen, W.Z. Wu, and J.M. Tan. 2018. Overexpression of ULK1 Represents a Potential

Diagnostic Marker for Clear Cell Renal Carcinoma and the Antitumor Effects of SBI-0206965. *EBioMedicine*. 34:85-93.

Lystad, A.H., S.R. Carlsson, L.R. de la Ballina, K.J. Kauffman, S. Nag, T. Yoshimori, T.J. Melia, and A. Simonsen. 2019. Distinct functions of ATG16L1 isoforms in membrane binding and LC3B lipidation in autophagy-related processes. *Nat Cell Biol*. 21:372-383.

Mack, H.I., B. Zheng, J.M. Asara, and S.M. Thomas. 2012. AMPK-dependent phosphorylation of ULK1 regulates ATG9 localization. *Autophagy*. 8:1197-1214.

Maeda, S., C. Otomo, and T. Otomo. 2019. The autophagic membrane tether ATG2A transfers lipids between membranes. *Elife*. 8.

Maeda, S., H. Yamamoto, L.N. Kinch, C.M. Garza, S. Takahashi, C. Otomo, N.V. Grishin, S. Forli, N. Mizushima, and T. Otomo. 2020. Structure, lipid scrambling activity and role in autophagosome formation of ATG9A. *Nat Struct Mol Biol*. 27:1194-1201.

Manczyk, N., B.P. Yates, G. Veggiani, A. Ernst, F. Sicheri, and S.S. Sidhu. 2017. Structural and functional characterization of a ubiquitin variant engineered for tight and specific binding to an alpha-helical ubiquitin interacting motif. *Protein Sci*. 26:1060-1069.

Marshall, R.S., Z. Hua, S. Mali, F. McLoughlin, and R.D. Vierstra. 2019. ATG8-Binding UIM Proteins Define a New Class of Autophagy Adaptors and Receptors. *Cell*. 177:766-781.e724.

Marshall, R.S., Z. Hua, S. Mali, F. McLoughlin, and R.D. Vierstra. 2022. ATG8-Binding UIM Proteins Define a New Class of Autophagy Adaptors and Receptors. *Cell*. 185:1101-1102.

Martin, K.R., S.L. Celano, A.R. Solitro, H. Gunaydin, M. Scott, R.C. O'Hagan, S.D. Shumway, P. Fuller, and J.P. MacKeigan. 2018. A Potent and Selective ULK1 Inhibitor Suppresses Autophagy and Sensitizes Cancer Cells to Nutrient Stress. *iScience*. 8:74-84.

Mathew, R., V. Karantza-Wadsworth, and E. White. 2007. Role of autophagy in cancer. *Nat Rev Cancer*. 7:961-967.

Matoba, K., T. Kotani, A. Tsutsumi, T. Tsuji, T. Mori, D. Noshiro, Y. Sugita, N. Nomura, S. Iwata, Y. Ohsumi, T. Fujimoto, H. Nakatogawa, M. Kikkawa, and N.N. Noda. 2020. Atg9 is a lipid scramblase that mediates autophagosomal membrane expansion. *Nat Struct Mol Biol*. 27:1185-1193.

Matoba, K., and N.N. Noda. 2020. Secret of Atg9: lipid scramblase activity drives de novo autophagosome biogenesis. *Cell Death Differ*. 27:3386-3388.

Melia, T.J., A.H. Lystad, and A. Simonsen. 2020. Autophagosome biogenesis: From membrane growth to closure. *J Cell Biol*. 219.

Mercer, C.A., A. Kaliappan, and P.B. Dennis. 2009. A novel, human Atg13 binding protein, Atg101, interacts with ULK1 and is essential for macroautophagy. *Autophagy*. 5:649-662.

Mercer, T.J., A. Gubas, and S.A. Tooze. 2018. A molecular perspective of mammalian autophagosome biogenesis. *J Biol Chem*. 293:5386-5395.

Mizushima, N. 2010. The role of the Atg1/ULK1 complex in autophagy regulation. *Curr Opin Cell Biol*. 22:132-139.

Mizushima, N., A. Kuma, Y. Kobayashi, A. Yamamoto, M. Matsubae, T. Takao, T. Natsume, Y. Ohsumi, and T. Yoshimori. 2003a. Mouse Apg16L, a novel WD-repeat protein, targets to the autophagic isolation membrane with the Apg12-Apg5 conjugate. *J Cell Sci*. 116:1679-1688.

Mizushima, N., T. Noda, T. Yoshimori, Y. Tanaka, T. Ishii, M.D. George, D.J. Klionsky, M. Ohsumi, and Y. Ohsumi. 1998. A protein conjugation system essential for autophagy. *Nature*. 395:395-398.

Mizushima, N., A. Yamamoto, M. Hatano, Y. Kobayashi, Y. Kabeya, K. Suzuki, T. Tokuhisa, Y. Ohsumi, and T. Yoshimori. 2001. Dissection of autophagosome formation using Apg5-deficient mouse embryonic stem cells. *J Cell Biol*. 152:657-668.

Mizushima, N., T. Yoshimori, and Y. Ohsumi. 2003b. Role of the Apg12 conjugation system in mammalian autophagy. *Int J Biochem Cell Biol*. 35:553-561.

Mohsen, S., P.T. Sobash, G.F. Algwaiz, N. Nasef, S.A. Al-Zeidaneen, and N.A. Karim. 2022. Autophagy Agents in Clinical Trials for Cancer Therapy: A Brief Review. *Curr Oncol*. 29:1695-1708.

Nakamura, S., and T. Yoshimori. 2017. New insights into autophagosome-lysosome fusion. *J Cell Sci*. 130:1209-1216.

Nishimura, T., N. Tamura, N. Kono, Y. Shimanaka, H. Arai, H. Yamamoto, and N. Mizushima. 2017. Autophagosome formation is initiated at phosphatidylinositol synthase-enriched ER subdomains. *EMBO J*. 36:1719-1735.

Nixon, R.A. 2007. Autophagy, amyloidogenesis and Alzheimer disease. *J Cell Sci*. 120:4081-4091.

Noda, N.N. 2021. Atg2 and Atg9: Intermembrane and interleaflet lipid transporters driving autophagy. *Biochim Biophys Acta Mol Cell Biol Lipids*. 1866:158956.

Noda, N.N., H. Kumeta, H. Nakatogawa, K. Satoo, W. Adachi, J. Ishii, Y. Fujioka, Y. Ohsumi, and F. Inagaki. 2008. Structural basis of target recognition by Atg8/LC3 during selective autophagy. *Genes Cells*. 13:1211-1218.

Ohashi, Y. 2021. Activation Mechanisms of the VPS34 Complexes. *Cells*. 10.

Olivas, T.J., Y. Wu, S. Yu, L. Luan, P. Choi, S. Nag, P. De Camilli, K. Gupta, and T.J. Melia. 2022. ATG9 vesicles comprise the seed membrane of mammalian autophagosomes. *bioRxiv*:2022.2008.2016.504143.

Orsi, A., M. Razi, H.C. Dooley, D. Robinson, A.E. Weston, L.M. Collinson, and S.A. Tooze. 2012. Dynamic and transient interactions of Atg9 with autophagosomes, but not membrane integration, are required for autophagy. *Mol Biol Cell*. 23:1860-1873.

Osawa, T., T. Kotani, T. Kawaoka, E. Hirata, K. Suzuki, H. Nakatogawa, Y. Ohsumi, and N.N. Noda. 2019. Atg2 mediates direct lipid transfer between membranes for autophagosome formation. *Nat Struct Mol Biol*. 26:281-288.

Otomo, T., S. Chowdhury, and G.C. Lander. 2018. The rod-shaped ATG2A-WIPI4 complex tethers membranes in vitro. *Contact (Thousand Oaks)*. 1.

Pankiv, S., T.H. Clausen, T. Lamark, A. Brech, J.A. Bruun, H. Outzen, A. Øvervatn, G. Bjørkøy, and T. Johansen. 2007. p62/SQSTM1 binds directly to Atg8/LC3 to facilitate degradation of ubiquitinated protein aggregates by autophagy. *J Biol Chem*. 282:24131-24145.

Park, J.M., C.H. Jung, M. Seo, N.M. Otto, D. Grunwald, K.H. Kim, B. Moriarity, Y.M. Kim, C. Starker, R.S. Nho, D. Voytas, and D.H. Kim. 2016. The ULK1 complex mediates MTORC1 signaling to the autophagy initiation machinery via binding and phosphorylating ATG14. *Autophagy*. 12:547-564.

Pasquier, B., Y. El-Ahmad, B. Filoche-Rommé, C. Dureuil, F. Fassy, P.Y. Abecassis, M. Mathieu, T. Bertrand, T. Benard, C. Barrière, S. El Batti, J.P. Letallec, V. Sonnefraud, M. Brollo, L. Delbarre, V. Loyau, F. Pilorge, L. Bertin, P. Richepin, J. Arigon, J.R. Labrosse, J. Clément, F. Durand, R. Combet, P. Perraut, V. Leroy, F. Gay, D. Lefrançois, F. Bretin, J.P. Marquette, N. Michot, A. Caron, C. Castell, L.

Schio, G. McCort, H. Goulaouic, C. Garcia-Echeverria, and B. Ronan. 2015. Discovery of (2S)-8-[(3R)-3-methylmorpholin-4-yl]-1-(3-methyl-2-oxobutyl)-2-(trifluoromethyl)-3,4-dihydro-2H-pyrimido[1,2-a]pyrimidin-6-one: a novel potent and selective inhibitor of Vps34 for the treatment of solid tumors. *J Med Chem*. 58:376-400.

Popovic, D., and I. Dikic. 2014. TBC1D5 and the AP2 complex regulate ATG9 trafficking and initiation of autophagy. *EMBO Rep*. 15:392-401.

Proikas-Cezanne, T., Z. Takacs, P. Dönnes, and O. Kohlbacher. 2015. WIPI proteins: essential PtdIns3P effectors at the nascent autophagosome. *J Cell Sci*. 128:207-217.

Qian, K., C.T. Huang, C.L. Huang, H. Chen, L.W. Blackbourn, Y. Chen, J. Cao, L. Yao, C. Sauvey, Z. Du, and S.C. Zhang. 2014. A simple and efficient system for regulating gene expression in human pluripotent stem cells and derivatives. *Stem Cells*. 32:1230-1238.

Ren, J., R. Liang, W. Wang, D. Zhang, L. Yu, and W. Feng. 2020. Multi-site-mediated entwining of the linear WIR-motif around WIPI β-propellers for autophagy. *Nat Commun*. 11:2702.

Ro, S.H., C.H. Jung, W.S. Hahn, X. Xu, Y.M. Kim, Y.S. Yun, J.M. Park, K.H. Kim, M. Seo, T.Y. Ha, E.A. Arriaga, D.A. Bernlohr, and D.H. Kim. 2013. Distinct functions of Ulk1 and Ulk2 in the regulation of lipid metabolism in adipocytes. *Autophagy*. 9:2103-2114.

Rocchi, A., and C. He. 2017. Regulation of Exercise-Induced Autophagy in Skeletal Muscle. *Curr Pathobiol Rep*. 5:177-186.

Rothman, J.S., L. Kocsis, E. Herzog, Z. Nusser, and R.A. Silver. 2016. Physical determinants of vesicle mobility and supply at a central synapse. *Elife*. 5.

Runwal, G., E. Stamatakou, F.H. Siddiqi, C. Puri, Y. Zhu, and D.C. Rubinsztein. 2019. LC3-positive structures are prominent in autophagy-deficient cells. *Sci Rep*. 9:10147.

Russell, R.C., Y. Tian, H. Yuan, H.W. Park, Y.Y. Chang, J. Kim, H. Kim, T.P. Neufeld, A. Dillin, and K.L. Guan. 2013. ULK1 induces autophagy by phosphorylating Beclin-1 and activating VPS34 lipid kinase. *Nat Cell Biol*. 15:741-750.

Rusten, T.E., T. Vaccari, K. Lindmo, L.M. Rodahl, I.P. Nezis, C. Sem-Jacobsen, F. Wendler, J.P. Vincent, A. Brech, D. Bilder, and H. Stenmark. 2007. ESCRTs and Fab1 regulate distinct steps of autophagy. *Curr Biol*. 17:1817-1825.

Sawa-Makarska, J., V. Baumann, N. Coudevylle, S. von Bülow, V. Nogellova, C. Abert, M. Schuschnig, M. Graef, G. Hummer, and S. Martens. 2020. Reconstitution of autophagosome nucleation defines Atg9 vesicles as seeds for membrane formation. *Science*. 369.

Schaaf, M.B., T.G. Keulers, M.A. Vooijs, and K.M. Rouschop. 2016. LC3/GABARAP family proteins: autophagy-(un)related functions. *FASEB J*. 30:3961-3978.

Scherz-Shouval, R., Y. Sagiv, H. Shorer, and Z. Elazar. 2003. The COOH terminus of GATE-16, an intra-Golgi transport modulator, is cleaved by the human cysteine protease HsApg4A. *J Biol Chem*. 278:14053-14058.

Schmidt, J.C., A.J. Zaug, and T.R. Cech. 2016. Live Cell Imaging Reveals the Dynamics of Telomerase Recruitment to Telomeres. *Cell*. 166:1188-1197.e1189.

Sergé, A., N. Bertaux, H. Rigneault, and D. Marguet. 2008. Dynamic multiple-target tracing to probe spatiotemporal cartography of cell membranes. *Nat Methods*. 5:687-694.

Shi, X., A.L. Yokom, C. Wang, L.N. Young, R.J. Youle, and J.H. Hurley. 2020. ULK complex organization in autophagy by a C-shaped FIP200 N-terminal domain dimer. *J Cell Biol*. 219.

Shpilka, T., H. Weidberg, S. Pietrokovski, and Z. Elazar. 2011. Atg8: an autophagy-related ubiquitin-like protein family. *Genome Biol*. 12:226.

Staufer, O., J.E. Hernandez Bücher, J. Fichtler, M. Schröter, I. Platzman, and J.P. Spatz. 2022. Vesicle Induced Receptor Sequestration: Mechanisms behind Extracellular Vesicle-Based Protein Signaling. *Adv Sci (Weinh)*. 9:e2200201.

Stavoe, A.K., P.P. Gopal, A. Gubas, S.A. Tooze, and E.L. Holzbaur. 2019. Expression of WIPI2B counteracts age-related decline in autophagosome biogenesis in neurons. *Elife*. 8.

Strong, L.M., C. Chang, J.F. Riley, C.A. Boecker, T.G. Flower, C.Z. Buffalo, X. Ren, A.K. Stavoe, E.L. Holzbaur, and J.H. Hurley. 2021. Structural basis for membrane recruitment of ATG16L1 by WIPI2 in autophagy. *Elife*. 10.

Szymańska, P., K.R. Martin, J.P. MacKeigan, W.S. Hlavacek, and T. Lipniacki. 2015. Computational analysis of an autophagy/translation switch based on mutual inhibition of MTORC1 and ULK1. *PLoS One*. 10:e0116550.

Takahashi, Y., H. He, Z. Tang, T. Hattori, Y. Liu, M.M. Young, J.M. Serfass, L. Chen, M. Gebru, C. Chen, C.A. Wills, J.M. Atkinson, H. Chen, T. Abraham, and H.G. Wang. 2018. An autophagy assay reveals the ESCRT-III component CHMP2A as a regulator of phagophore closure. *Nat Commun*. 9:2855.

Tang, Z., Y. Takahashi, H. He, T. Hattori, C. Chen, X. Liang, H. Chen, M.M. Young, and H.G. Wang. 2019. TOM40 Targets Atg2 to Mitochondria-Associated ER Membranes for Phagophore Expansion. *Cell Rep*. 28:1744-1757.e1745.

Tanida, I., E. Tanida-Miyake, M. Komatsu, T. Ueno, and E. Kominami. 2002. Human Apg3p/Aut1p homologue is an authentic E2 enzyme for multiple substrates, GATE-16, GABARAP, and MAP-LC3, and facilitates the conjugation of hApg12p to hApg5p. *J Biol Chem*. 277:13739-13744.

Tanida, I., E. Tanida-Miyake, T. Ueno, and E. Kominami. 2001. The human homolog of Saccharomyces cerevisiae Apg7p is a Protein-activating enzyme for multiple substrates including human Apg12p, GATE-16, GABARAP, and MAP-LC3. *J Biol Chem*. 276:1701-1706.

Tarantino, N., J.Y. Tinevez, E.F. Crowell, B. Boisson, R. Henriques, M. Mhlanga, F. Agou, A. Israël, and E. Laplantine. 2014. TNF and IL-1 exhibit distinct ubiquitin requirements for inducing NEMO-IKK supramolecular structures. *J Cell Biol*. 204:231-245.

Tecalco-Cruz, A.C., J. Pedraza-Chaverri, A. Briones-Herrera, E. Cruz-Ramos, L. López-Canovas, and J. Zepeda-Cervantes. 2022. Protein degradation-associated mechanisms that are affected in Alzheimer´s disease. *Mol Cell Biochem*. 477:915-925.

Tooze, S.A. 2013. Current views on the source of the autophagosome membrane. *Essays Biochem*. 55:29-38.

Towers, C.G., and A. Thorburn. 2016. Therapeutic Targeting of Autophagy. *Ebiomedicine*. 14:15-23.

Valverde, D.P., S. Yu, V. Boggavarapu, N. Kumar, J.A. Lees, T. Walz, K.M. Reinisch, and T.J. Melia. 2019. ATG2 transports lipids to promote autophagosome biogenesis. *J Cell Biol*. 218:1787-1798.

Vietri, M., M. Radulovic, and H. Stenmark. 2020. The many functions of ESCRTs. *Nat Rev Mol Cell Biol*. 21:25-42.

Wang, S., H. Li, M. Yuan, H. Fan, and Z. Cai. 2022. Role of AMPK in autophagy. *Front Physiol*. 13:1015500.

Waugh, M.G. 2019. The Great Escape: how phosphatidylinositol 4-kinases and PI4P promote vesicle exit from the Golgi (and drive cancer). *Biochem J*. 476:2321-2346.

Weerasekara, V.K., D.J. Panek, D.G. Broadbent, J.B. Mortenson, A.D. Mathis, G.N. Logan, J.T. Prince, D.M. Thomson, J.W. Thompson, and J.L. Andersen. 2014. Metabolic-stress-induced rearrangement of the 14-3-3ζ interactome promotes autophagy via a ULK1- and AMPK-regulated 14-3-3ζ interaction with phosphorylated Atg9. *Mol Cell Biol*. 34:4379-4388.

Weigert, M., U. Schmidt, T. Boothe, A. Müller, A. Dibrov, A. Jain, B. Wilhelm, D. Schmidt, C. Broaddus, S. Culley, M. Rocha-Martins, F. Segovia-Miranda, C. Norden, R. Henriques, M. Zerial, M. Solimena, J. Rink, P. Tomancak, L. Royer, F. Jug, and E.W. Myers. 2018. Content-aware image restoration: pushing the limits of fluorescence microscopy. *Nat Methods*. 15:1090-1097.

White, E. 2015. The role for autophagy in cancer. *Journal of Clinical Investigation*. 125:42-46.

Xi, L., J.C. Schmidt, A.J. Zaug, D.R. Ascarrunz, and T.R. Cech. 2015. A novel two-step genome editing strategy with CRISPR-Cas9 provides new insights into telomerase action and TERT gene expression. *Genome Biol*. 16:231.

Yamamoto, A., Y. Tagawa, T. Yoshimori, Y. Moriyama, R. Masaki, and Y. Tashiro. 1998. Bafilomycin A1 prevents maturation of autophagic vacuoles by inhibiting fusion between autophagosomes and lysosomes in rat hepatoma cell line, H-4-II-E cells. *Cell Struct Funct*. 23:33-42.

Yamamoto, H., S. Kakuta, T.M. Watanabe, A. Kitamura, T. Sekito, C. Kondo-Kakuta, R. Ichikawa, M. Kinjo, and Y. Ohsumi. 2012. Atg9 vesicles are an important membrane source during early steps of autophagosome formation. *J Cell Biol*. 198:219-233.

Yim, W.W., H. Yamamoto, and N. Mizushima. 2022. A pulse-chasable reporter processing assay for mammalian autophagic flux with HaloTag. *Elife*. 11.

Ylä-Anttila, P., H. Vihinen, E. Jokitalo, and E.L. Eskelinen. 2009. 3D tomography reveals connections between the phagophore and endoplasmic reticulum. *Autophagy*. 5:1180-1185.

Young, A.R., E.Y. Chan, X.W. Hu, R. Köchl, S.G. Crawshaw, S. High, D.W. Hailey, J. Lippincott-Schwartz, and S.A. Tooze. 2006. Starvation and ULK1-dependent cycling of mammalian Atg9 between the TGN and endosomes. *J Cell Sci*. 119:3888-3900.

Yu, L., Y. Chen, and S.A. Tooze. 2018. Autophagy pathway: Cellular and molecular mechanisms. *Autophagy*. 14:207-215.

Yun, M., H.Y. Bai, J.X. Zhang, J. Rong, H.W. Weng, Z.S. Zheng, Y. Xu, Z.T. Tong, X.X. Huang, Y.J. Liao, S.J. Mai, S. Ye, and D. Xie. 2015. ULK1: a promising biomarker in predicting poor prognosis and therapeutic response in human nasopharygeal carcinoma. *PLoS One*. 10:e0117375.

Zachari, M., M. Longo, and I.G. Ganley. 2020. Aberrant autophagosome formation occurs upon small molecule inhibition of ULK1 kinase activity. *Life Sci Alliance*. 3.

Zhen, Y., H. Spangenberg, M.J. Munson, A. Brech, K.O. Schink, K.W. Tan, V. Sørensen, E.M. Wenzel, M. Radulovic, N. Engedal, A. Simonsen, C. Raiborg, and H. Stenmark. 2020. ESCRT-mediated phagophore sealing during mitophagy. *Autophagy*. 16:826-841.

Zoncu, R., L. Bar-Peled, A. Efeyan, S. Wang, Y. Sancak, and D.M. Sabatini. 2011. mTORC1 senses lysosomal amino acids through an inside-out mechanism that requires the vacuolar H(+)-ATPase. *Science*. 334:678-683.